

## Cover Page

### ALPHA FOUNDATION FOR THE IMPROVEMENT OF MINE SAFETY AND HEALTH

#### Final Technical Report

**Project Title: Full-Wave Electromagnetic Solver for Statistical Characterization, Optimal Deployment, and On-the-Fly Reconfiguration of Wireless and Through-the-Earth Communication and Tracking Systems**

**Grant Number: AFC-215-54**

**Organization: University of Michigan, Ann Arbor**

**Principal Investigator: Eric Michielssen**

**Contact Information :**

**Department of Electrical Engineering and Computer Science**

**University of Michigan, Ann Arbor**

[emichiel@umich.edu](mailto:emichiel@umich.edu)

**(734) 353 0629**

**Period of Performance: 09/01/15 – 4/30/18**

**Acknowledgement/Disclaimer:** This study was sponsored by the Alpha Foundation for the Improvement of Mine Safety and Health, Inc. (ALPHA FOUNDATION). The views, opinions and recommendations expressed herein are solely those of the authors and do not imply any endorsement by the ALPHA FOUNDATION, its Directors and staff."

Note: technical terms in the report marked by \* are explained in Appendix A.

## 1 Executive Summary:

This report is the result of research conducted by Prof. Eric Michielssen's group at the University of Michigan under contract with the Alpha Foundation. The objective of this project was to develop a new computational framework that leverages novel full wave electromagnetic (EM) simulators in concert with modern *Uncertainty Quantification\** (UQ) and optimization techniques to produce actionable quantitative data and qualitative insights to aid in the design, deployment, and post-event reconfiguration of communication and tracking systems customized to specific mine environments.

Wireless sensing, communication, and tracking systems are essential for planning and conducting routine mining operations, as well as for safeguarding miners' health and planning life-saving actions after catastrophic events [1]. The efficient design and optimization of such systems hinges on the use of computational frameworks that incorporate EM simulators, UQ tools and optimization engines. Ideally, these EM simulators should be capable of accurately characterizing EM propagation in realistic mine entries and galleries that incorporate internal structures (mining and communication equipment, and miners); moreover they should permit coupling with UQ tools that permit the statistical characterization of EM observables and optimizers for wireless network (re)configuration. Meanwhile, the UQ tools should be able to efficiently and accurately gather statistics (e.g. *Probability Density Functions\** (PDFs)) of received signal strength due to uncertainties in mine environments and wireless network layout, and the optimization engine should permit fast network synthesis while minimizing system deployment cost (e.g. the number of transmitters and repeaters). This report presents an EM simulation framework that realizes the above, i.e. permits fast and efficient stochastic analysis and optimization of communication networks in mine environments.

The proposed framework couples two novel EM simulators, a sophisticated UQ tool, and an optimization method. The two EM simulators are domain decomposition - based and fast-multiple method – fast Fourier transform (FMM-FFT) integral equation solvers, both tailored to efficiently simulate EM propagation phenomena in mine environments. Next, these two simulators are coupled with a high-dimension model representation (HDMR) UQ method, which is fine-tuned to minimize the number of calls to the EM simulators. Finally, the EM-UQ framework is coupled with a Dividing RECTangles (DIRECT) optimization engine to synthesize communication systems in mine environments.

The applicability and efficiency of the proposed framework are demonstrated via statistical analysis, optimization, and reconfiguration of several real-world communication systems commonly used in mine environments, including a leaky feeder, a through-the-earth communication system, a medium frequency radio system, and a wireless node-based mesh network.

The application of the framework is expected to facilitate the design of communication systems that are used in mine environments to protect the health and safety of miners and enhance operational efficiency.

## 2 Problem Statement and Objective:

### 2.1 Background and Problem Statement

The EM framework proposed herein involves novel EM simulators that are strategically coupled with *Uncertainty Quantification\** (UQ) tools and optimization algorithms to statistically analyze and efficiently synthesize real-world wireless communication systems in mine environments. To our knowledge it constitutes the first research framework of its kind, capable of providing reliable quantitative data to aid in the design, deployment, and post-event reconfiguration of communication and tracking systems customized to realistic mine environments.

#### EM Simulation Methods

During the past two decades, various EM simulators based on approximate and full wave techniques for analyzing EM wave propagation in mine environments have been developed [2]. Frequently-used approximate techniques include, but are not limited to, single/multi-mode waveguide [3, 4], ray-tracing (or ray optics) [5-7], and cascaded-impedance methods. Invariably, these methods involve either simplifying assumptions about the physics of electromagnetic wave propagation (e.g. ray optics cannot account for geometric details on the order of the *electromagnetic wavelength\**) or the mine's geometry (e.g. the waveguide model assumes entries with perfect rectangular cross sections and smooth walls), thereby limiting their utility and ability to accurately analyze wireless communication systems inside complex mine environments. Without exception, these methods are restricted to certain frequency bands and cannot readily account for the presence of wall roughness, unstructured debris, miners, and mining equipment.

In contrast, simulators that leverage full-wave techniques do not invoke simplifying assumptions about the physics and/or geometry under consideration. Full-wave techniques, such as finite-difference-time-domain (FDTD) methods [8-11], finite elements methods, and surface integral equation (SIE) techniques [12-15] directly solve Maxwell's equations; discretization issues aside they do not invoke any simplifying assumptions about the nature of the electromagnetic field. Moreover they can account for geometric and material features that affect electromagnetic wave propagation and thus are capable of providing a complete and detailed characterization of signal transmission in inside a mine entry or gallery. More concretely, they can model entries and galleries with rough walls that are occupied by miners and mining equipment. That said, given the large *electrical size\** of entries and the high operating frequencies of modern wireless systems, the computational costs of these full-wave simulators oftentimes is prohibitively high, exceeding the capacity of existing computers by orders of magnitude, especially when used in statistical analysis or for wireless network optimization/(re)configuration. To reduce the computational burden associated with full wave solvers, we developed a fast multipole method – fast Fourier transform (FMM-FFT) accelerated surface integral equation (SIE) simulator allowing for the analysis of mine entries and galleries that span hundreds of wavelengths. We further extended the capabilities of the simulator through the use of domain decomposition (DD) and Tucker decomposition (TD) methods, resulting in two novel EM simulators that together enable the analysis of mine environments spanning thousands of wavelengths.

### Uncertainty Quantification (UQ)

Unfortunately, the usefulness of full-wave simulators for analyzing for communication systems in mine environments is adversely affected by the fact that many aspects of a mine layout and operation are intrinsically stochastic in nature. In other words, many of the parameters that describe a communication scenario in a mine are uncertain; examples include, but are not limited to, the mine's geometry, locations of miners and mining equipment, locations of transmitters and receivers, material parameters, etc. This uncertainty and dependency must be accurately quantified and reflected into the simulators' predictions. Such capability enables, for example, the estimation of uncertainty in received power strengths associated with uncertainty in mine layout or rock electrical properties, the location or movement of miners, etc.

The need for UQ is oftentimes met by *Monte Carlo*\* (MC) methods. Unfortunately, MC methods require (too) many simulations to yield accurate statistical results. As each simulation of a mine environment can take minutes to hours, MC methods simply are too expensive to serve as the basis for UQ analysis in the proposed framework. To reduce the computational cost of MC methods, polynomial chaos (PC) [16] and multi-element probabilistic collocation (ME-PC) methods [17] have been developed. These methods first form a polynomial approximation (i.e. build a polynomial surrogate model) for each EM observable (e.g. received power) as a function of the uncertain parameters by probing the EM simulator. Then, the polynomial surrogate model is used in lieu of the simulator by the MC method. Evaluating the polynomial requires little computational effort and therefore this approach realizes significant computational savings compared to a brute-force MC method. That said, even in these methods a multivariate polynomial of prescribed order is constructed and the number of simulations required increases exponentially with the number of uncertain parameters (i.e. dimension of the random domain), making them of little use for most practical problems. To address this limitation, ME-PC methods recently have been hybridized with high dimensional model representation (HDMR) techniques [18]. The resulting technique allows for the generation of a surrogate model in a high dimensional random domain by bootstrapping surrogate models generated in lower dimensional random domains. The technique iteratively constructs an HDMR surrogate model by only including so-called "component functions" pertinent to the "most important" random variables, and therefore dramatically reduces the cost of surrogate model construction.

Use of this HDMR technique in conjunction with the proposed EM simulator allows for the efficient calculation the statistics of observables in stochastic EM wave propagation scenarios.

### Synthesis and Optimization

Optimization algorithms have long been applied to the design of wireless communication systems. Typical questions addressed by such optimization methods include: (i) where should one deploy (a minimal set of) transmitters and repeaters to ensure adequate signal coverage over an area of interest; (ii) how can a network of repeaters be re-configured in the event the propagation environment changes, e.g. due to a catastrophic event.

Frequently-used optimization algorithms are either stochastic in nature, gradient-based, or rooted in direct search. Stochastic algorithms, such as genetic algorithms [19] and particle swarm optimization [20], use random variables to search for values of design parameters that maximize an objective function, e.g. the worst case received power level. These algorithms

typically introduce a number of random ‘seeds’ that cover the search space and determine the direction and step size for each seed that is informed by the best solution found thus far. Oftentimes, these algorithms find strong local or even global optima. That said, a relative large population of seeds/design candidates is needed to ensure the search space is adequately covered to avoid convergence to a weak local optimum; this requirement significantly increases the number of objective function evaluations.

Gradient-based methods, such as the quasi-Newton [21] and adjoint sensitivity methods [22], require information about the derivatives of the objective function to determine the search direction. They oftentimes are highly efficient, requiring a minimum of objective function evaluations -- this is especially true when the objective function is smooth and continuous -- but may fail to find the optimum when the derivative information is not reliable. The highly unpredictable properties of the objective function involved in the design of mine communication systems (discontinuities, non-differentiability, and noise) renders gradient-based algorithms and stochastic algorithms all but useless for the proposed framework.

Direct search algorithms turn out to be well-suited to finding the optimal placement of wireless devices, since they require only the value of the objective function and require a relatively small number of objective function evaluations. Direct search algorithms determine directions to be explored by directly comparing current and past sample values of objective functions. Hence, they are derivative-free and can be applied to objective functions that are discontinuous and non-smooth. Direct search algorithms are often classified as global or local in nature. Local direct search algorithms, such as the Nelder-Mead simplex [23] and Hooke-Jeeves algorithms [24], are efficient in terms of the number of objective function evaluations. However, they get easily trapped by local optima, which occur even when designing very simple wireless mine communications systems. In contrast, global direct search algorithms such as DIRECT (DIViding RECTangles) algorithm [25-27], can find global optima using a reasonable number of objective function evaluations. DIRECT is a modification of standard Lipschitzian optimization methods and is widely-used in engineering applications.

In this study, the DIRECT algorithm is adopted and incorporated into the aforementioned EM simulators and UQ framework.

## **2.2 Objectives**

The research presented here has four objectives:

- (i) Development of EM simulators: a fast multipole method - fast Fourier transform accelerated surface integral equation simulator and a domain decomposition based surface integral equation simulator.
- (ii) Development of UQ methods: application of Karhunen-Loeve expansions to model wall roughness and the ME-PC enhanced HDMR method for modeling uncertain system parameters.
- (iii) Development of efficient optimization schemes for designing wireless mine communication networks and reconfiguring them post-disaster.
- (iv) Application of the EM+UQ framework to statistically characterize numerous practical communication systems, including leaky feeder networks (VHF - UHF) replete with amplifiers and repeaters, TTE systems composed of surface or buried loops (VLF), medium frequency (MF) radio systems, and various wireless mesh network (WMN)

systems. Also, evaluation of the framework's potential to optimally deploy and reconfigure wireless systems to enhance mine safety.

The research in Objectives (i)-(iii) has a distinct applied mathematical / computer science flavor. The focus is on selection and development of numerically rigorous, full-wave computational methods capable of modeling electromagnetic wave propagation in realistic mine environments. In other words, the focus is on the selection and hybridization of existing EM simulation methods, and the development of new methods that exploit particular features of mine propagation problems to enhance the solver's computational efficiency, i.e. minimize their computer memory and CPU usage. This is not an abstract or inconsequential exercise. Prior to this research, there existed no full-wave methods capable of analyzing wave propagation in realistic mine environments. The principal outcome of this research is that it enables the first application of full-wave as opposed to approximate techniques to the problem of wave propagation in complex mine environments.

The research in Objective (iv) aims to demonstrate the usefulness of the framework developed in (i)-(iii) through analysis of various practical systems. A complete characterization of these systems is, however, beyond the scope of this study. The authors hope that the nature of the results presented will spur the community to adapt the methods developed in (i)-(iii) to carry out such studies.

### 3 Research Approach

This Section details research performed towards Objectives (i)-(iii) above. Code validation efforts aimed at demonstrating the accuracy, efficiency, and applicability of the EM simulators, UQ methods, and optimization engine, are presented also.

Research towards Objective (iv) relating to the application of the EM-UQ framework to the analysis and design of various communication systems is discussed in Section 4: Research Findings and Accomplishments.

#### 3.1 Objective 1: EM Simulator Development

This section details the development of various techniques for analyzing EM wave propagation in mine environments.

All simulators take as input:

- A geometric description of the mine environment. In practice, the walls of the mine entries and galleries (exterior and pillars) are discretized in terms of a triangular elements. This task is easily accomplished using commercially available mesh generators. The mesh may contain tens of millions of nodes, edges, and surface elements, and should reflect any roughness in the walls.
- The geometry of all mining equipment. In practice, it is assumed that all equipment is made of metal, i.e. is Perfect Electrically Conducting (PEC). Extensions of the simulators aimed at modeling penetrable (i.e. plastic) equipment and miners are possible but were not implemented; their impact on the propagation characteristics are assumed small.
- The *electric permittivity*\* of the rock surrounding the mine entry. The solvers assume this material to be homogeneous.
- The frequency, location, orientation, and strength of antennas that produce the wireless signal. In practice, one often assumes that the transmitting antenna is a simple dipole or monopole.
- The locations of (generalized) receivers, i.e. places in the mine where the simulator is to compute power densities.

All simulators produce:

- Electric and magnetic field densities on the walls of the mine.
- Electric current densities on conducting mining equipment and communication systems.
- Electric fields, magnetic fields, and power densities at receiver locations.

Electric and magnetic fields and associated current densities on walls and equipment serve to compute fields and power densities at received locations. They also provide a means for visualizing fields inside the mining environment.

All simulators use Surface Integral Equation (SIE) techniques for modeling penetrable (mine walls) and PEC structures (mining and communication equipment). SIE techniques were chosen over popular Finite Difference Time Domain (FDTD) and Finite Element Methods (FEM) as they only associate unknowns with the walls/surface of the mining environment as opposed to its volume. Unknown counts associated with SIE methods therefore are much smaller than those for their FDTD and FEM counterparts. Even so, the computational (CPU and memory) costs of these SIE solvers often is astronomical. The CPU and memory costs of traditional SIE solvers scales

as  $O(N^3)$  and  $O(N^2)$ , respectively; here  $N$  represents the number of unknowns, i.e. edges in the surface mesh for the mine walls and equipment. For realistic mine environments  $N$  can be many millions, even tens of millions, rendering the execution of these methods difficult even on the world's most powerful computers. To combat the curse of dimensionality and reduce these prohibitive computational costs, we employ so-called “fast solver” methods. These methods exhibit lower computational complexity, and enable their implementation on a small supercomputer; most results presented herein consumed a few hours of computing time on computers with less than 1,000 cores (readily available from many vendors and in the commercial cloud).

Below, we describe two fast solver constructs: a Domain Decomposition (DD) SIE solver and a Tucker decomposition enhanced Fast Multipole Method – Fast Fourier Transform (FMM-FFT) simulator.

- The DD-based significantly reduces the computational cost of a classical surface integral equation simulator. It does so by first characterizing separate sections of the mine entry and then stitching together these models to characterize the entire propagation path.
- The Tucker decomposition-enhanced FMM-FFT simulator complements the DD-based SIE simulator. Principally, the Tucker decomposition aims to reduce the memory required for storing so-called translation operator matrices when performing FMM-FFT procedures.

### **3.1.1 Task 1.1: Domain Decomposition Based Surface Integral Equation Simulator**

#### **3.1.1.1 Introduction**

In this section, a fast, full-wave, and memory-efficient domain decomposition (DD) based 3-D SIE simulator for efficiently analyzing EM wave propagation in electrically large and realistic mine environments is described. The proposed simulator first divides the physical mine entries/galleries into subdomains and defines equivalent surfaces between them using Huygens' principle. Then, it obtains reduced order representations using equivalent surfaces to characterize EM wave propagation in each subdomain separately. The reduced order representations –called scattering matrices– are computed using a fast and efficient butterfly-based direct solver [28] and an FMM-FFT scheme [29-32]. Finally, it constructs and solves an inter-domain system accounting for EM interactions between equivalent surfaces. The solution of the inter-domain system is accelerated by judiciously combining subdomains into larger ones via an efficient subdomain combining scheme for electrically large mine environments.

As explained in detail in this section and demonstrated in the code validation section, the proposed simulator is far more memory and CPU efficient than conventional fast simulators, such as FMM-FFT accelerated SIE simulators. It significantly outperforms conventional fast simulators especially for problems involving EM analyses of electrically large entries/galleries with multiple excitations, encountered in UQ and optimal wireless node placement studies. This is due to the fact that the proposed simulator obtains and solves a reduced system with significantly fewer degrees of freedom compared to conventional fast simulators. To that end, it performs the analysis in two stages: (i) it computes scattering matrices (only once) during its offline stage and (ii) it updates the right hand side of inter-domain system and solves the reduced system for each different excitation during its online stage. For problems involving electrically large entries, the subdomain combining scheme is applied and the computational cost of the proposed



simulator, which peak during stage (ii), scale logarithmically with the entry length while those of the conventional fast simulators scale quasi-linearly. When the subdomain combining scheme is not applied, the computational cost of the proposed simulator scale linearly with the entry length while remaining lower than that of conventional fast simulators for electrically large entries. Furthermore, the memory requirement of the proposed simulator with and without subdomain combining scheme scales logarithmically and remains constant with entry length, respectively.

The applicability, accuracy, and efficiency of the proposed simulator are demonstrated through its application to the analysis of EM wave propagation in an arched entry, rectangular entries with rough walls and a partial cave-in, and a mine gallery; the simulator also is used to statistically characterize EM wave propagation in an electrically large rectangular entry.

### 3.1.1.2 Formulation

This section first explains the domain decomposition strategy to split the physical domain of a mine environment into subdomains and expounds the computation of scattering matrices for characterizing EM wave propagation in each subdomain. Then, it presents the inter-domain system and its expedient solution via a subdomain combining scheme. Finally, it provides the theoretical estimates for the computational cost and memory requirement of the proposed simulator.

#### A) Domain Decomposition Strategy

Consider a straight rectangular mine entry which is assumed to be filled by air with permittivity  $\varepsilon_0$  and permeability  $\mu_0$  (medium 0) and surrounded by unbounded rock with permittivity  $\varepsilon_1$ , permeability  $\mu_1$ , and conductivity  $\sigma$  (medium 1) [Fig. 3-1 (a)]. The entry with walls, denoted  $\Omega$  [Fig. 3-1 (a)], is split into four subdomains (for the sake of simplicity and demonstration) denoted  $\Omega_i$ ,  $i = a, b, c, d$  [Fig. 3-1 (b)]. By invoking the Huygens' equivalence principle, equivalent surfaces enclosing each subdomain are defined [Fig. 3-1 (b)]. The adjacent subdomains and equivalent surfaces touch each other as  $\delta$  approaches zero and consequently the union of subdomains  $\Omega_i$ ,  $i = a, b, c, d$  yields the original domain [Fig. 3-1 (c)].

The small skin depth due to the lossy surrounding environment and high operating frequencies of wireless communication systems allows limiting each equivalent surface to a portion of touching surfaces between adjacent subdomains [Fig. 3-1 (d)-(e)]. The equivalent electric and magnetic current densities  $\mathbf{J}_p(\mathbf{r})$  and  $\mathbf{M}_p(\mathbf{r})$ ,  $p = 1, \dots, 3$  are defined on these surfaces in accordance with the outward pointing unit normal of surfaces  $\hat{\mathbf{n}}_p$ ,  $p = 1, \dots, 3$ . These surfaces and the equivalent current densities are used to characterize EM wave propagation in each subdomain separately, as explained in the following subsection. (Note: the domain decomposition example given in and subdomains and equivalent surfaces defined therein are extensively referred to in this section (without loss of generality) to avoid heavy generic notation.)

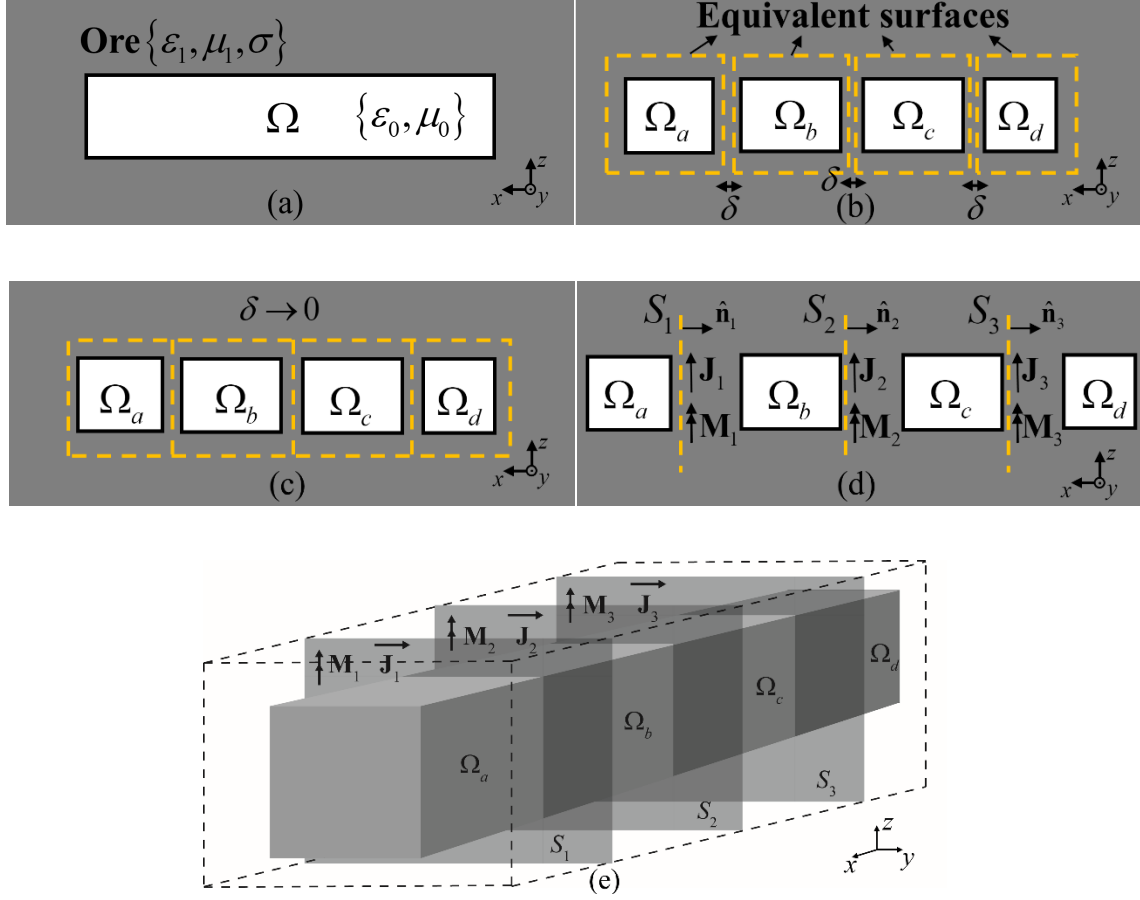


Fig. 3-1: Domain decomposition scheme for a mine entry: (a) The original physical domain of the entry. (b) Decomposition with equivalent surfaces. (c) Overlapping equivalent surfaces between subdomains. (d) Truncated equivalent surfaces and equivalent currents. (e) 3-D view of the decomposed straight entry.

#### B) Scattering Matrix of Individual Subdomain

EM wave propagation in each subdomain defined in Fig. 3-1 (d) is characterized by a scattering matrix  $\mathbf{Z}^i$ ,  $i \in \{a, b, c, d\}$ . Consider that  $\mathbf{J}_p(\mathbf{r})$  and  $\mathbf{M}_p(\mathbf{r})$ ,  $p=1, \dots, 3$ , on each equivalent surface (in Fig. 3-1 (d)) are discretized by  $2N_p$  Rao-Wilton-Glisson (RWG) basis functions  $\mathbf{f}_{p,j}(\mathbf{r})$  [33] as

$$\mathbf{J}_p(\mathbf{r}) = \sum_{j=1}^{N_p} I_{p,j} \mathbf{f}_{p,j}(\mathbf{r}), \quad \mathbf{M}_p(\mathbf{r}) = \sum_{j=N_p+1}^{2N_p} I_{p,j} \mathbf{f}_{p,j}(\mathbf{r}) \quad (3.1)$$

where  $I_{p,j}$ ,  $j=1, \dots, 2N_p$ , are unknown expansion coefficients of the currents on  $S_p$ ,  $p=1, \dots, 3$ . The scattering matrix  $\mathbf{Z}^i$  relates the discretized currents defined on equivalent surfaces touching to  $\Omega_i$  to the discretized tested fields (scattered from  $\Omega_i$ ) on them. For an example subdomain  $\Omega_c$  in Fig. 3-1 (d), this relation is expressed via a matrix system as

$$\begin{bmatrix} \mathbf{Z}_{22}^c & \mathbf{Z}_{23}^c \\ \mathbf{Z}_{32}^c & \mathbf{Z}_{33}^c \end{bmatrix} \begin{bmatrix} \mathbf{I}_2 \\ \mathbf{I}_3 \end{bmatrix} = \begin{bmatrix} \mathbf{V}_2^{sca} \\ \mathbf{V}_3^{sca} \end{bmatrix} \quad (3.2)$$

where the scattering matrix  $\mathbf{Z}^c$  is formed by  $2 \times 2$  scattering submatrices.  $\mathbf{I}_p$  is the vector holding the unknown expansion coefficients of the discretized currents on  $S_p$ ,  $p \in \{2, 3\}$ .  $\mathbf{V}_q^{sca}$  is the vector formed by the vectors of scattered electric fields  $\mathbf{E}_q^{sca}$  and scattered magnetic fields  $\mathbf{H}_q^{sca}$  tested on  $S_q$ , as  $\mathbf{V}_q^{sca} = [\mathbf{E}_q^{sca}; \mathbf{H}_q^{sca}]$ ,  $q \in \{2, 3\}$ . The  $2N_q \times 2N_p$  scattering submatrix  $\mathbf{Z}_{qp}^c$ ,  $q, p \in \{2, 3\}$ , maps the currents on  $S_p$  to the scattered fields on  $S_q$  by accounting for the wave propagation characteristics of the subdomain  $\Omega_c$ .  $2N_q$  is the number of RWG basis functions used to discretize the currents on  $S_q$ . It is computed performing the following three steps for all basis functions on  $S_p$ :

- Step 1: Generate a unit vector  $\mathbf{I}_p$  with non-zero entry corresponding to a basis function on  $S_p$  and compute the fields generated via  $\mathbf{I}_p$  and tested on  $\Omega_c$  with RWG basis functions.
- Step 2: Obtain the electric and magnetic currents on  $\Omega_c$  induced by the fields computed in step 1.
- Step 3: Compute the tested fields on  $S_q$  generated by the currents obtained in step 2.

These three steps are illustrated to obtain an example scattering submatrix  $\mathbf{Z}_{32}^c$  in Fig. 3-2 and described in detail as follows:

Step 1: The current densities  $\mathbf{J}_p(\mathbf{r})$  and  $\mathbf{M}_p(\mathbf{r})$  on  $S_p$  generate the electric and magnetic fields on  $\Omega_c$ ,  $\mathbf{E}^c(\mathbf{r})$  and  $\mathbf{H}^c(\mathbf{r})$ , [Fig. 3-2 (a)] via

$$\mathbf{E}^c(\mathbf{r}) = \mathcal{L}_1[\pm \mathbf{J}_p(\mathbf{r})] + \mathcal{K}_1[\pm \mathbf{M}_p(\mathbf{r})], \quad (3.3)$$

$$\mathbf{H}^c(\mathbf{r}) = -\mathcal{K}_1[\pm \mathbf{J}_p(\mathbf{r})] + (1/\eta_1^2)\mathcal{L}_1[\pm \mathbf{M}_p(\mathbf{r})], \quad (3.4)$$

Here  $\eta_1 = (\mu_1/\epsilon_1)^{0.5}$ ,  $\mathbf{r} \in \Omega_c$ , and the signs of  $\mathbf{J}_p(\mathbf{r})$  and  $\mathbf{M}_p(\mathbf{r})$  are positive if they are defined on the side of  $S_p$  facing to  $\Omega_c$ ; otherwise, they are negative. The integral operators  $\mathcal{L}_\alpha$  and  $\mathcal{K}_\alpha$  are defined as

$$\mathcal{L}_\alpha[\mathbf{F}(\mathbf{r})] = j\omega\mu_\alpha \int_S (\bar{\mathbf{I}} + (k_\alpha^{-2}\nabla\nabla')) G_\alpha(\mathbf{r}, \mathbf{r}') \mathbf{F}(\mathbf{r}') d\mathbf{r}' \quad (3.5)$$

$$\mathcal{K}_\alpha[\mathbf{F}(\mathbf{r})] = -\nabla \times \int_S G_\alpha(\mathbf{r}, \mathbf{r}') \mathbf{F}(\mathbf{r}') d\mathbf{r}' \quad (3.6)$$

where  $\omega = 2\pi f$ ,  $f$  is the frequency,  $G_\alpha(\mathbf{r}, \mathbf{r}') = \exp(-jk_\alpha |\mathbf{r} - \mathbf{r}'|) / (4\pi |\mathbf{r} - \mathbf{r}'|)$  is the Green's function [34] for the medium  $\alpha \in \{0, 1\}$  and  $k_\alpha = \omega(\mu_\alpha \epsilon_\alpha)^{0.5}$ .

Step 2: The electric and magnetic fields on  $\Omega_c$ ,  $\mathbf{E}^c(\mathbf{r})$  and  $\mathbf{H}^c(\mathbf{r})$ , (computed in step 1) induce the current densities  $\mathbf{J}^c(\mathbf{r})$  and  $\mathbf{M}^c(\mathbf{r})$  on  $\Omega_c$  [Fig. 3-2 (b)], which are obtained solving

$$-\mathbf{E}^c(\mathbf{r}) = (\mathcal{L}_0 + \mathcal{L}_1)[\mathbf{J}^c(\mathbf{r})] + (\mathcal{K}_0 + \mathcal{K}_1)[\mathbf{M}^c(\mathbf{r})], \quad (3.7)$$

$$-\mathbf{H}^c(\mathbf{r}) = -(\mathcal{K}_0 + \mathcal{K}_1)[\mathbf{J}^c(\mathbf{r})] + \left( \frac{\mathcal{L}_0}{\eta_0^2} + \frac{\mathcal{L}_1}{\eta_1^2} \right) [\mathbf{M}^c(\mathbf{r})], \quad (3.8)$$

where  $\mathbf{r} \in \Omega_c$ . (3.7) and (3.8) are well-known Poggio-Muller-Chang-Harrington-Wu-Tsai (PMCHWT) equations [34] and are solved for  $\mathbf{J}^c(\mathbf{r})$  and  $\mathbf{M}^c(\mathbf{r})$ , as detailed below.

Step 3: The current densities  $\mathbf{J}^c(\mathbf{r})$  and  $\mathbf{M}^c(\mathbf{r})$  generate the electric and magnetic fields on  $S_q$ ,  $\mathbf{E}_q(\mathbf{r})$  and  $\mathbf{H}_q(\mathbf{r})$ , [Fig. 3-2 (c)] via

$$\mathbf{E}_q(\mathbf{r}) = \mathcal{L}_1[\mathbf{J}^c(\mathbf{r})] + \mathcal{K}_1[\mathbf{M}^c(\mathbf{r})], \quad (3.9)$$

$$\mathbf{H}_q(\mathbf{r}) = -\mathcal{K}_1[\mathbf{J}^c(\mathbf{r})] + (1/\eta_1^2)\mathcal{L}_1[\mathbf{M}^c(\mathbf{r})], \quad (3.10)$$

where  $\mathbf{r} \in S_q$ . Discretizing the currents in (3.3), (3.4), and (3.7)-(3.10) and Galerkin testing the resulting equations yields  $2N_q \times 2N_p$  scattering submatrix  $\mathbf{Z}_{qp}^c$  that relates currents on  $S_p$  to fields on  $S_q$  as

$$\mathbf{Z}_{qp}^c = \mathbf{C}_q^c (\mathbf{B}^c)^{-1} \mathbf{A}_p^c, \quad (3.11)$$

Here  $\mathbf{A}_p^c$ ,  $\mathbf{B}^c$ , and  $\mathbf{C}_q^c$  are the matrices of discretized operators with dimensions  $2N_c \times 2N_p$ ,  $2N_c \times 2N_c$ , and  $2N_q \times 2N_c$  (obtained in steps 1, 2, and 3), respectively.  $2N_c$  is the number of RWG basis functions used to discretize the currents on  $\Omega_c$ . Inverting  $\mathbf{B}^c$  via classical direct methods is computationally expensive when  $N_c$  is large (more than tens/hundreds of thousands). To this end, the proposed simulator leverages a butterfly-based direct solver for computing the compressed inverse (LU factors) of  $\mathbf{B}^c$ , realizing significant savings when compared to conventional direct solvers for inverting  $\mathbf{B}^c$ . Specifically, the solver first hierarchically decomposes the discretized PWCHWT impedance matrix  $\mathbf{B}^c$  and compresses its off-diagonal blocks via butterflies [35]. Next, the solver computes a compressed LU factorization of  $\mathbf{B}^c$  via recursively computing sums and products of butterfly-compressed partial LU factors as new butterfly representations, which is augmented by a fast matrix-vector multiplication-based low-complexity randomized butterfly scheme. The details of this solver can be found in [28]. Once  $(\mathbf{B}^c)^{-1}$  is obtained, the remaining computationally costly operations to obtain  $\mathbf{Z}_{qp}^c$  are the multiplications of matrices  $\mathbf{A}_p^c$  and  $\mathbf{C}_q^c$  with a vector while computing  $\mathbf{Z}_{qp}^c \mathbf{I}_p$ ; such operations are accelerated by an FMM-FFT scheme [29-32].

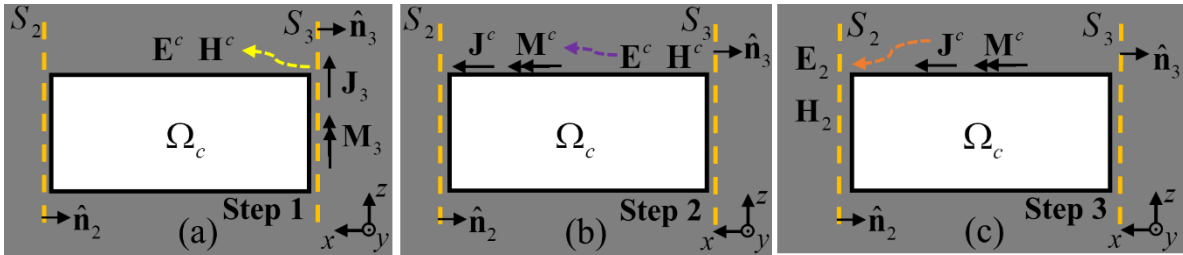


Fig. 3-2: Procedure for computing scattering submatrix  $\mathbf{Z}_{23}^3$ . (a) Step 1: coefficient of a basis function on  $S_3$  is set to unit and the fields produced by this current are tested on  $\Omega_c$ . (b) Step 2: the currents on  $\Omega_c$  due to the incident fields obtained in step 1 are solved. (c) Step 3: the fields produced by the currents obtained in step 2 are tested on  $S_2$ .

### C) Inter-Domain System

The scattering matrices computed to characterize the EM wave propagation in each subdomain are used to form the inter-domain system of equations that accounts for the interactions between equivalent surfaces. The interactions between equivalent surfaces that are not attached to the same subdomain are not included in inter-domain system since those are negligible due to the highly lossy background. The interactions between equivalent surfaces attached to the same subdomain are included in inter-domain system by carefully accounting

for the impressed sources in subdomains and induced currents on equivalent surfaces and by imposing the boundary conditions on the equivalent surfaces, as detailed below.

Consider the equivalent surface  $S_1$  attached to  $\Omega_a$  and  $\Omega_b$  [Fig. 3-3]. This equivalent surface interacts with itself and  $S_2$ . To illustrate its self-interaction,  $S_1$  is duplicated as  $S_1^+$  and  $S_1^-$  [Fig. 3-3 (a)]. While the self-interaction of  $S_1$  is represented as the interaction between  $S_1^+$  and  $S_1^-$ , the interaction between  $S_1$  and  $S_2$  is replaced by the interaction between  $S_1^-$  and  $S_2$  [Fig. 3-3 (a)]. Note that  $S_1^+$  does not interact with  $S_2$  since they are not attached to the same subdomain. Furthermore, the vectors holding the unknown expansion coefficients of the currents on  $S_1^+$  and  $S_1^-$  are denoted by  $\mathbf{I}_1^+$  and  $\mathbf{I}_1^-$ , respectively. To obtain  $\mathbf{I}_1^+$ , the fields impinging to the  $S_1^+$  should be determined. In fact, these are (i) the incident fields generated by possible impressed sources in  $\Omega_a$  and (ii) the fields generated by the currents on  $S_1^-$ , which travel throughout  $\Omega_a$ , impinge to the  $S_1^+$ , and thereby are characterized by scattering submatrix  $\mathbf{Z}_{11}^a$ . By taking into account these incident fields, the currents on  $S_1^+$  are obtained by solving the PMCHWT equations for  $S_1^+$ , which reads

$$\mathbf{D}_1 \mathbf{I}_1^+ = \mathbf{V}_{1,a}^{inc} - \mathbf{Z}_{11}^a \mathbf{I}_1^-, \quad (3.12)$$

where  $\mathbf{V}_{1,a}^{inc}$  is the tested incident fields on  $S_1^+$  due to impressed sources in  $\Omega_a$  and  $\mathbf{D}_1$  is the discretized PMCHWT matrix for  $S_1$  (see [34] for details). Similarly, the currents on  $S_1^-$  are obtained by accounting for the incident fields due to impressed sources in  $\Omega_b$  and the fields generated by the currents on  $S_1^+$  and  $S_2$ , which travel throughout  $\Omega_b$ , impinge to the  $S_1^-$ , and thereby are characterized by scattering submatrices  $\mathbf{Z}_{11}^b$  and  $\mathbf{Z}_{12}^b$ , respectively [Fig. 3-3 (c)]. By considering these incident fields, the currents on  $S_1^-$  are obtained via

$$\mathbf{D}_1 \mathbf{I}_1^- = \mathbf{V}_{1,b}^{inc} - \mathbf{Z}_{11}^b \mathbf{I}_1^+ - \mathbf{Z}_{12}^b \mathbf{I}_2, \quad (3.13)$$

where  $\mathbf{V}_{1,b}^{inc}$  is the tested incident fields on  $S_1^-$  due to impressed sources in  $\Omega_b$ . Since  $S_1^+$  and  $S_1^-$  coincide, currents on both surfaces equal to each other ( $\mathbf{I}_1 = \mathbf{I}_1^+ = \mathbf{I}_1^-$ ). Denoting  $\bar{\mathbf{Z}}_{11}^a = \mathbf{Z}_{11}^a + \mathbf{D}_1$ ,  $\bar{\mathbf{Z}}_{11}^b = \mathbf{Z}_{11}^b + \mathbf{D}_1$ , and summing (3.12) and (3.13) yield the inter-domain equation for  $S_1$

$$(\bar{\mathbf{Z}}_{11}^a + \bar{\mathbf{Z}}_{11}^b) \mathbf{I}_1 + \mathbf{Z}_{12}^b \mathbf{I}_2 = \mathbf{V}_1^{inc}, \quad (3.14)$$

where  $\mathbf{V}_1^{inc} = \mathbf{V}_{1,a}^{inc} + \mathbf{V}_{1,b}^{inc}$ . By extending the above procedure to all other equivalent surfaces, the inter-domain system for the example entry in Fig.1 is obtained as

$$\begin{bmatrix} \bar{\mathbf{Z}}_{11}^a + \bar{\mathbf{Z}}_{11}^b & \mathbf{Z}_{12}^b & 0 \\ \mathbf{Z}_{21}^b & \bar{\mathbf{Z}}_{22}^b + \bar{\mathbf{Z}}_{22}^c & \mathbf{Z}_{23}^c \\ 0 & \mathbf{Z}_{32}^c & \bar{\mathbf{Z}}_{33}^c + \bar{\mathbf{Z}}_{33}^d \end{bmatrix} \begin{bmatrix} \mathbf{I}_1 \\ \mathbf{I}_2 \\ \mathbf{I}_3 \end{bmatrix} = \begin{bmatrix} \mathbf{V}_1^{inc} \\ \mathbf{V}_2^{inc} \\ \mathbf{V}_3^{inc} \end{bmatrix}, \quad (3.15)$$

where  $\mathbf{V}_p^{inc} = [\mathbf{E}_p^{inc}; \mathbf{H}_p^{inc}]$ ,  $p = 1, \dots, 3$ , is the vector of incident electric and magnetic fields on  $S_p$  due to impressed sources in the subdomains touching  $S_p$ . It is zero if all subdomains touching to  $S_p$  are (impressed) source-free. Similar equations can be easily derived for entries and galleries with more subdomains attached to more than two equivalent surfaces. Once the inter-domain system (3.15) is solved, the currents on each equivalent surface are used to compute the currents on  $\Omega_i$  (and hence fields anywhere inside  $\Omega_i$ ) via steps 1 and 2 of the procedures to obtain scattering matrix. For example, the current coefficients  $\mathbf{I}^b$  on  $\Omega_b$  are computed as

$$\mathbf{I}^b = (\mathbf{B}^b)^{-1} \mathbf{A}_1^b \mathbf{I}_1 + (\mathbf{B}^b)^{-1} \mathbf{A}_2^b \mathbf{I}_2, \quad (3.16)$$

In case one subdomain contains impressed sources, the incident fields generated by impressed sources should be accounted for while computing the currents pertinent to that subdomain.

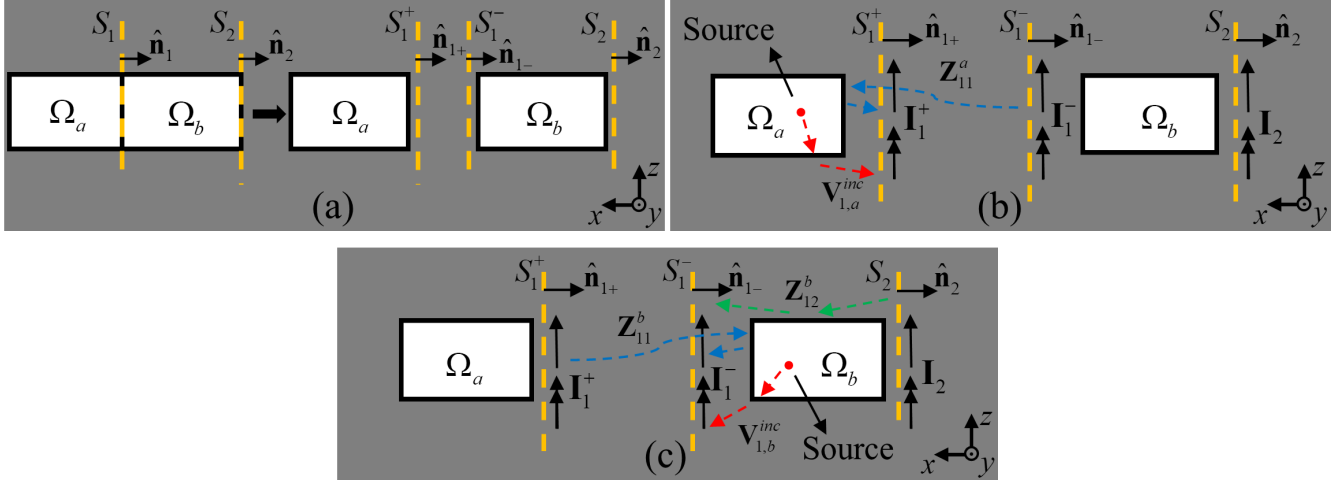


Fig. 3-3: (a) Separation of subdomains  $\Omega_a$  and  $\Omega_b$ . (b) The incident fields on  $S_1^+$ . Red dash line represents the fields due to sources in  $\Omega_a$ ; blue dash line represents the fields radiated by currents on  $S_1^-$  and scattered by  $\Omega_a$ . (c) The incident fields on  $S_1^-$ . Red dash line represents the fields due to sources in  $\Omega_b$ ; blue dash line represents the fields radiated by currents on  $S_1^+$  and scattered by  $\Omega_b$ ; green dash line represents the fields radiated by currents on  $S_2$  and scattered by  $\Omega_b$ .

When the repetitive execution of an EM simulator for many different excitations is required for uncertainty quantification or optimum wireless node placement studies, the proposed DD-based SIE simulator only updates the right hand side of (3.15) and re-solves the inter-domain system for new excitations during the online stage of the simulator. Note that the scattering matrices of individual subdomains are computed only once and stored during the offline stage of the simulator. Furthermore, many mine entries or galleries have repeated geometric features and therefore it is reasonable to assume that many subdomains of mine entries and galleries are identical. Therefore, the scattering matrices for all subdomains decomposing a large mine environment can be obtained by characterizing only a few different subdomains.

#### D) Subdomain Combining Scheme

When the electrically large mine entries and galleries are divided into hundreds of subdomains, solving the inter-domain system could be computationally expensive. To this end, an efficient scheme that combines the adjacent identical subdomains and alleviates this computational burden is proposed here.

Consider two adjacent subdomains  $\Omega_b$  and  $\Omega_c$  (in Fig. 3-1 (d)) with associated equivalent surfaces  $S_p$ ,  $p=1, \dots, 3$ . As derived in (3.2), the relations between currents and fields on these equivalent surfaces are expressed via scattering matrices of these subdomains as

$$\begin{bmatrix} \mathbf{Z}_{11}^b & \mathbf{Z}_{12}^b & 0 \\ \mathbf{Z}_{21}^b & \bar{\mathbf{Z}}_{22}^b + \bar{\mathbf{Z}}_{22}^c & \mathbf{Z}_{23}^c \\ 0 & \mathbf{Z}_{32}^c & \mathbf{Z}_{33}^c \end{bmatrix} \begin{bmatrix} \mathbf{I}_1 \\ \mathbf{I}_2 \\ \mathbf{I}_3 \end{bmatrix} = \begin{bmatrix} \mathbf{V}_1^{sca} \\ \mathbf{V}_2^{sca} \\ \mathbf{V}_3^{sca} \end{bmatrix}, \quad (3.17)$$

By comparing (3.15) and (3.17), one can found that  $\mathbf{V}_2^{sca} = \mathbf{V}_2^{inc}$ . Hence, when there is no source inside these subdomains, i.e.  $\mathbf{V}_2^{sca} = 0$ ,  $\mathbf{I}_2$  can be eliminated from (3.17). The resulting equation is

$$\begin{bmatrix} \mathbf{Z}_{11}^{new} & \mathbf{Z}_{13}^{new} \\ \mathbf{Z}_{31}^{new} & \mathbf{Z}_{33}^{new} \end{bmatrix} \begin{bmatrix} \mathbf{I}_1 \\ \mathbf{I}_3 \end{bmatrix} = \begin{bmatrix} \mathbf{V}_1^{sca} \\ \mathbf{V}_3^{sca} \end{bmatrix}, \quad (3.18)$$

where

$$\mathbf{Z}_{11}^{new} = \mathbf{Z}_{11}^b - \mathbf{Z}_{12}^b (\bar{\mathbf{Z}}_{22}^b + \bar{\mathbf{Z}}_{22}^c)^{-1} \mathbf{Z}_{21}^b, \quad (3.19)$$

$$\mathbf{Z}_{13}^{new} = -\mathbf{Z}_{12}^b (\bar{\mathbf{Z}}_{22}^b + \bar{\mathbf{Z}}_{22}^c)^{-1} \mathbf{Z}_{23}^c, \quad (3.20)$$

$$\mathbf{Z}_{31}^{new} = -\mathbf{Z}_{32}^c (\bar{\mathbf{Z}}_{22}^b + \bar{\mathbf{Z}}_{22}^c)^{-1} \mathbf{Z}_{21}^b, \quad (3.21)$$

$$\mathbf{Z}_{33}^{new} = \mathbf{Z}_{33}^c - \mathbf{Z}_{32}^c (\bar{\mathbf{Z}}_{22}^b + \bar{\mathbf{Z}}_{22}^c)^{-1} \mathbf{Z}_{23}^c, \quad (3.22)$$

Note that (3.18) characterizes the wave propagation between  $S_1$  and  $S_3$ . It implies that the two subdomains are combined and treated as one while  $\mathbf{Z}_{11}^{new}$ ,  $\mathbf{Z}_{13}^{new}$ ,  $\mathbf{Z}_{31}^{new}$ , and  $\mathbf{Z}_{33}^{new}$  are new scattering submatrices of the scattering matrix  $\mathbf{Z}^{new}$  for the combined subdomain. A reduced inter-domain system of equations can then be formed using  $\mathbf{Z}^{new}$  as

$$\begin{bmatrix} \bar{\mathbf{Z}}_{11}^a + \bar{\mathbf{Z}}_{11}^{new} & \mathbf{Z}_{13}^{new} \\ \mathbf{Z}_{31}^{new} & \bar{\mathbf{Z}}_{33}^{new} + \bar{\mathbf{Z}}_{33}^d \end{bmatrix} \begin{bmatrix} \mathbf{I}_1 \\ \mathbf{I}_3 \end{bmatrix} = \begin{bmatrix} \mathbf{V}_1^{inc} \\ \mathbf{V}_3^{inc} \end{bmatrix}, \quad (3.23)$$

where  $\bar{\mathbf{Z}}_{11}^{new} = \mathbf{Z}_{11}^{new} + \mathbf{D}_1$  and  $\bar{\mathbf{Z}}_{33}^{new} = \mathbf{Z}_{33}^{new} + \mathbf{D}_3$ . The matrix system in (3.23) is apparently smaller than that in (3.23). After  $\mathbf{I}_1$  and  $\mathbf{I}_3$  are solved,  $\mathbf{I}_2$  can be computed via

$$\mathbf{I}_2 = -(\bar{\mathbf{Z}}_{22}^b + \bar{\mathbf{Z}}_{22}^c)^{-1} (\mathbf{Z}_{21}^b \mathbf{I}_1 + \mathbf{Z}_{23}^c \mathbf{I}_3), \quad (3.24)$$

Repeating this procedure permits merging any number of source-free subdomains into one subdomain and reduce the dimensionality of the inter-domain system of equation. The reduced inter-domain system is oftentimes small enough to be directly inverted via direct methods regardless of the entry's length. When most of the subdomains are source-free and identical, the subdomain combination operation can be performed in a recursive manner and consequently the computational cost of subdomain combining scheme scales logarithmically with the number of subdomains. It is noteworthy to mention that, in case the impressed sources reside in the same subdomain while performing the analyses with different excitations, the subdomain combining procedure is executed only once for solving all different excitations.

#### E) Cost Analysis

The computational cost and memory requirement of offline and online stages of the proposed DD-based SIE simulator are analyzed as follows.

##### 1) Computing Scattering Matrix of a Subdomain (Offline Stage)

The computation of a scattering submatrix  $\mathbf{Z}_{qp}^i$  for a subdomain  $\Omega_i$ , ( $i \in a, b, c, d$  in Fig. 3-1 (d)) requires multiplication of  $2N_p$  unit vectors with  $\mathbf{C}_q^i (\mathbf{B}^i)^{-1} \mathbf{A}_p^i$ . In steps 1 and 3, the matrix-vector multiplications are computed via the FMM-FFT acceleration scheme with maximum  $O(N_i \log N_i)$

computational and memory resources for one multiplication [32], given that  $2N_i$  is the number of basis functions used to discretize currents on  $\Omega_i$ . In step 2, inversion of  $\mathbf{B}^i$  and its multiplication with vectors from step 1 are performed via the butterfly-based direct solver, which requires  $O(N_i^{1.5} \log N_i)$  and  $O(N_i \log^2 N_i)$  computational and memory resources for computing the inverse and  $O(N_i \log N_i)$  computational resources for multiplying  $(\mathbf{B}^i)^{-1}$  with the vectors [28]. By summing these estimates for three steps and considering that  $N_p N_i \gg N_i^{1.5}$  in general, the total computational cost  $U_{sub}$  and memory requirement  $M_{sub}$  for computing one scattering matrix scale as

$$U_{sub} = O(N_p N_i \log N_i) , \quad (3.25)$$

$$M_{sub} = O(N_p N_i) , \quad (3.26)$$

## 2) Solving Inter-Domain System (Online Stage)

When the subdomain combining scheme is used, the inter-domain system is solved in two phases: combining the subdomains and solving the reduced inter-domain system.

In the first phase, combining a pair of subdomains calls for one matrix inversion and four matrix-matrix multiplications, requiring  $O(N_p^2 \log N_p)$  computational and memory resources, respectively. Since most of the subdomains are identical, subdomains are combined in a recursive manner and abovementioned operations are repeated  $N_p$  times, where  $N_p$  is the number of subdomains. Therefore, the computational cost and memory requirement of the first phase scale as  $O(N_p^3 \log N_p)$  and  $O(N_p^2)$ , respectively.

In the second phase, the reduced inter-domain system is formed using a small number of equivalent surfaces regardless of  $N_p$  and solved by a classical direct method. In case that a direct method is not applicable due to dimensionality of the reduced inter-domain system, an iterative solver [36] is used for inversion. Hence, the computational cost and memory requirement of the second phase scale as maximum  $O(N_p^2 \log N_p)$  and  $O(N_p^2)$ , respectively. To this end, the total computational cost and memory requirement of solving inter-domain system with subdomain combining scheme are

$$U_{int} = O(N_p^3 \log N_p) , \quad (3.27)$$

$$M_{int} = O(N_p^2 \log N_{sub}) . \quad (3.28)$$

It is clear in (3.27) and (3.28) that the computational cost and memory requirement scale logarithmically with the entry length. When the subdomain combining scheme is not used, the sparse inter-domain system of size  $N_p N_{sur} \times N_p N_{sur}$  is solved via an iterative solver [36], where  $N_{sur}$  is the number of equivalent surfaces. Note that the interactions between equivalent surfaces touching to the same subdomains are only included in inter-domain system and the number of scattering submatrices pertinent to each equivalent surface is bounded by a small constant. Therefore, the computational cost and memory requirement of solving inter-domain systems without subdomain combining scheme are

$$U_{int} = O(N_p^2 N_{sur}) , \quad (3.29)$$

$$M_{int} = O(N_p^2 \bar{N}_{sur}) , \quad (3.30)$$

where  $\bar{N}_{sur}$  is the number of equivalent surfaces attached to non-identical subdomains. Due to the repeated features of mine layouts,  $\bar{N}_{sur}$  is oftentimes a small number and does not depend



on  $N_{sub}$  or  $N_{sur}$ . Therefore,  $M_{int}$  scales with  $O(N_p^2)$  for many mine layouts and remains constant with increasing entry length. Note that solving the inter-domain system with subdomain combining scheme requires more memory resources than solving inter-domain system without it. On the other hand, solution with subdomain combining scheme is much faster than the solution without it, given that  $N_p$  is oftentimes a small number (due to the small electrical size of entry's cross sections) and iterative solvers generally have a large leading constant. The estimates of computational cost and memory requirements provided in (3.27) - (3.30) are numerically validated in numerical results.

For electrically large mine environments,  $N_p$  and  $N_i$  (as well as  $N_{sur}$  and  $N_{sub}$ ) are insignificant compared to the number of basis functions needed to discretize the currents on the walls of whole mine entries or galleries. Therefore, the proposed simulator (even without subdomain combining scheme) is much faster and more memory efficient compared to conventional fast full-wave EM simulators with quasi-linear complexity, as numerically proven in numerical results. Moreover, when the simulator is executed repetitively for different excitations, only the inter-domain system needs to be re-solved, leading to even more saving on the computational resources, as shown in the numerical results.

### 3.1.1.3 Code Validation

The DD-based surface integral (SIE) simulator is verified and validated by comparing the numerical results obtained by the proposed simulator to (i) analytical model and (ii) measurement data. The analytical model derives from the well-known multi-modal decomposition method [3]. In this model, mines entries are assumed to be rectangular waveguides with perfect geometrical shape, but with lossy dielectric characterization. EM fields inside the entry are expressed as a combination of waveguide propagation modes. It can compute the received power at any locations in a entry and its performance does not degrade with frequency. To verify the DD-based SIE simulator's applicability to complex mine layouts where the analytical model does not apply, measurement data from the Office of Mine Safety and Health Research (OMSHR) is used. The measurement data are obtained in a straight arched entry at both 455 MHz and 915 MHz. Unless stated otherwise, the entries are decomposed using 2.5-meter length subdomains at 915 MHz and 5-meter length subdomains at 455 MHz. All mine entries considered are surrounded by rock with relative permittivity  $\epsilon_r = 8.9$ , relative permeability  $\mu_r = 1$ , and conductivity  $\sigma = 0.15$  S/m. The width and height of most the rectangular entries and galleries considered are 1.85 m and 2.24 m, respectively. The proposed simulator was implemented using hybrid message passing interface/open multiprocessing (MPI/OpenMP) standards. All simulations were run on a cluster of dual hexacore X5650 Intel processors located at the Center for Advanced Computing, University of Michigan, Ann Arbor, MI, USA.

Numerical Example	Frequency (MHz)	Number of processors	Stage 1: Computing scattering matrices (offline stage)		Stage 2: Solving inter-domain system (online stage)	
			Time (hours)	Average memory per processor (GB)	Time (hours)	Average memory per processor (GB)

Empty rectangular entry	455	16	2.88	1.85	1.06	5.59
	915	32	18.68	3.65	10.25	32.08
Empty arched entry	455	16	3.24	2.46	1.18	7.81
	915	32	21.62	4.04	12.45	46.96

Table 3-1: Specifications of the Simulations Performed by the Proposed Simulator for Numerical Examples.

### 3.1.1.3.1 Comparison to Analytical Model

In this scenario, EM wave propagation is characterized in a smooth empty entry at 455 and 915 MHz. The length of the entry is 600 meters. The transmitting dipole antenna is located at (50.2, 0.925, 1.12) m and either chosen to be vertically or horizontally polarized. The magnitude of electric fields is computed at receiver points on a line connecting (51.0, 0.925, 1.12) m and (600, 0.925, 1.12) m. The results obtained by the DD-based SIE simulator are normalized and compared with results obtained by a multi-modal decomposition method. It is apparent from Fig. 3-4 (b)-(e) that the electric fields computed by the proposed DD-based SIE simulator and multi-mode decomposition method are in good agreement, which demonstrates the accuracy of the proposed simulator.

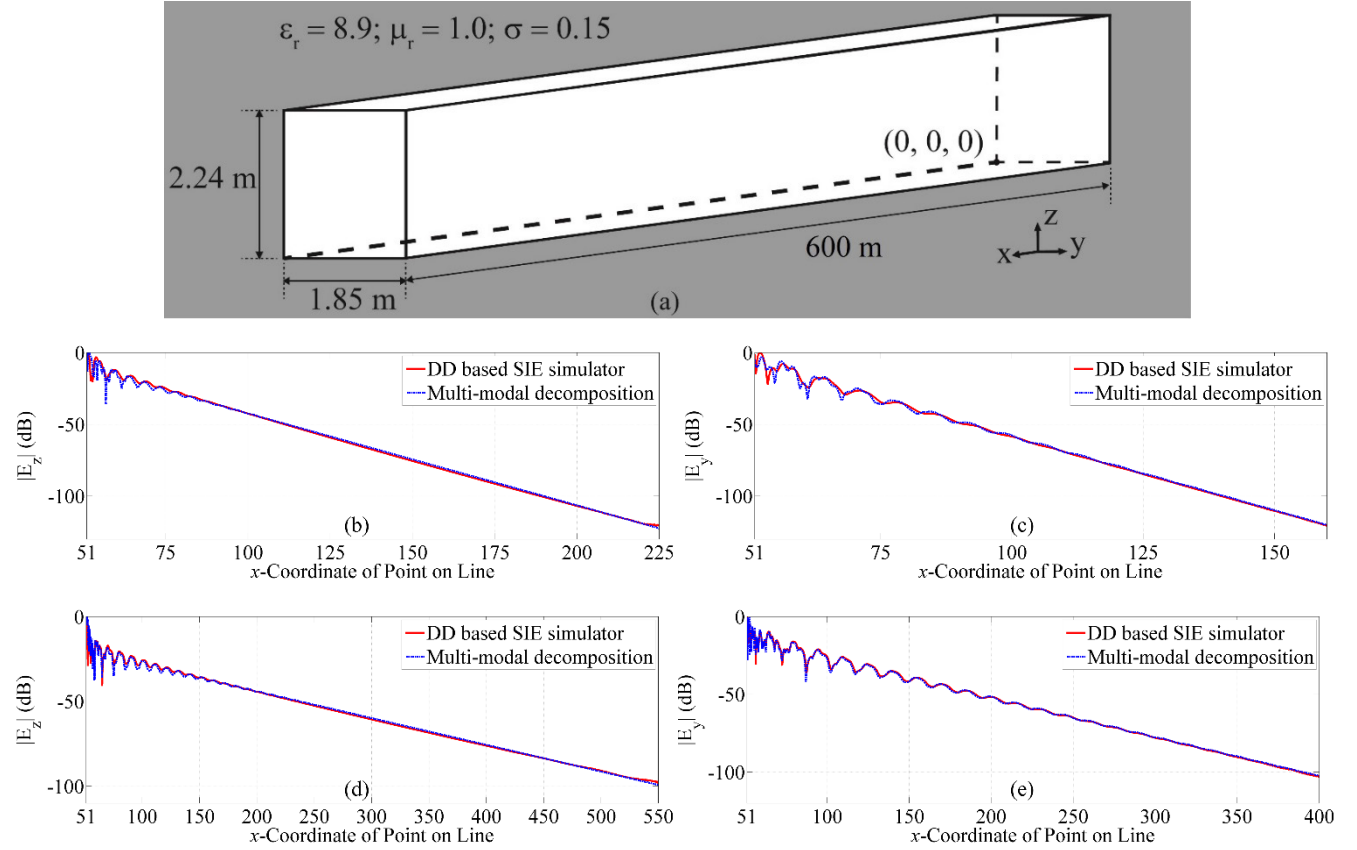
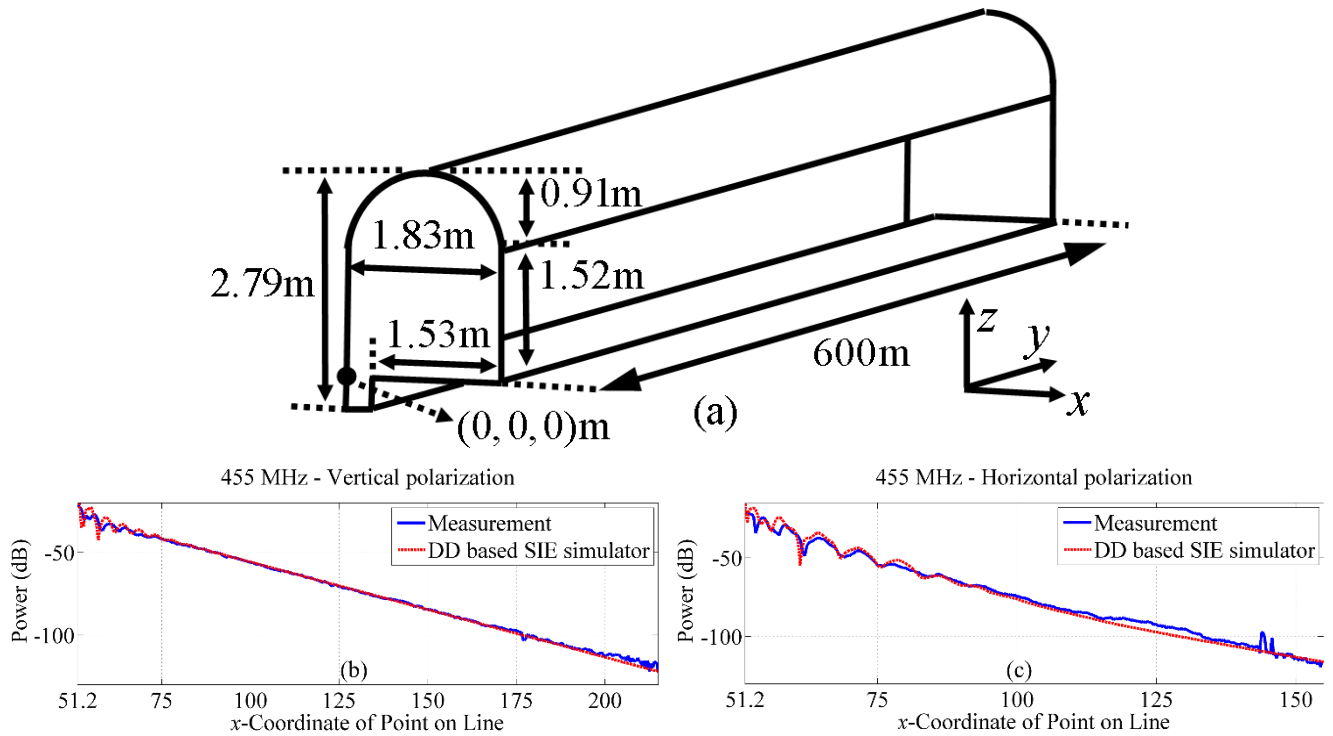


Fig. 3-4: (a) The geometry of an empty 600m-long rectangular entry. The power values on receiver points computed by the proposed simulator and obtained by measurements at 455 MHz for (b) vertical and (c) horizontal polarizations and at 915 MHz for (d) vertical and (e) horizontal polarizations.

### 3.1.1.3.2 Comparison to Measurement Data

To compare with the measurement data, the proposed simulator is used to characterize wave propagation in an arched entry [Fig. 3-5 (a)]. A transmitting electric dipole with unit moment is positioned at (0.915, 50, 1.22) m and power densities are computed at receiver locations spaced 10 cm apart along lines inside entry. The entry itself is surrounded by rock with relative permittivity  $\epsilon_r=8.9$ , relative permeability  $\mu_r=1.0$ , and conductivity  $\sigma=0.15$  S/m. An empty 600m– long arched entry is excited by an electric dipole that is either  $z$ – (vertically) or  $x$ – (horizontally) oriented and operated at 455 MHz or 915 MHz (4 cases) [Fig. 3-5 (a)]; at the lower and higher frequencies, entry walls are discretized using  $N=15,208,572$  and  $N=61,502,286$  RWG basis functions, respectively. For each case, power densities are computed at receivers on the line connecting (0.915, 51, 1.22) m and (0.915, 600, 1.22) m. Computed power densities are compared with measured data [37, 38, 73, 74] following normalization to account for uncertainties/differences in the excitation mechanism [Fig. 3-5 (b)-(e)]. Computed and measured power densities are in good agreement thereby validating the accuracy of the simulator.



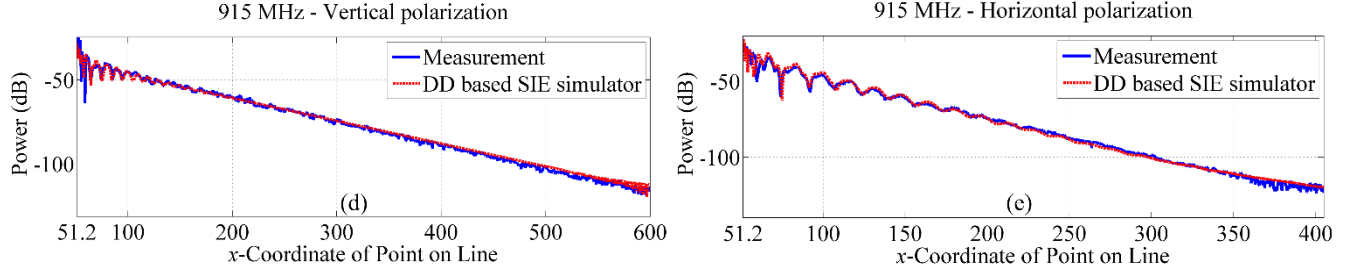


Fig. 3-5: (a) The geometry of an empty 600m-long arched entry (the lateral wall is removed for illustration). The power values on receiver points computed by the proposed simulator and obtained by measurements at 455 MHz for (b) vertical and (c) horizontal polarizations and at 915 MHz for (d) vertical and (e) horizontal polarizations.

### 3.1.1.3.3 Analysis of Empty Entry with Rough Lateral Walls

Next we characterize a straight rough entry with rough walls at 455 MHz. The dimensions and constitutive parameters of the entry and its surrounding environment for this case are the same as above, except that the entry has rough walls and is only 200 meters long [Fig. 3.6]. The incident dipole is again placed at (50.2, 0.9, 0.9) m and it is vertically polarized. The magnitude of the electric field is computed at two sets of receiver points and compared with results obtained by executing the solver assuming smooth walls. The first set of receiver points is located in the middle of the entry, while the second set is placed near the lateral wall. More specifically, the first set of receiver points resides on a line connecting points (51.2, 0.9, 0.9) m and (200, 0.9, 0.9) m, while the second set sits on a line connecting points (51.2, 0.2, 0.9) m and (200, 0.2, 0.9) m. These results show that roughness of the surface may affect the path loss and these effects should be included analysis of wave propagation inside the entry.

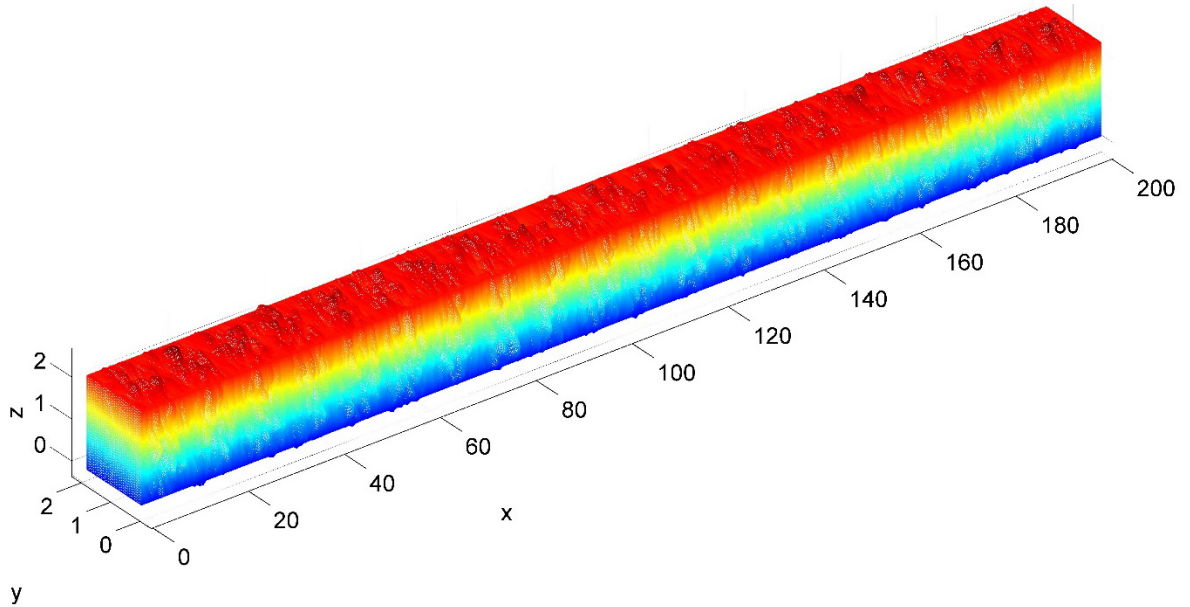


Fig. 3-6: Geometry for the 200-meter long empty entry with rough lateral walls.

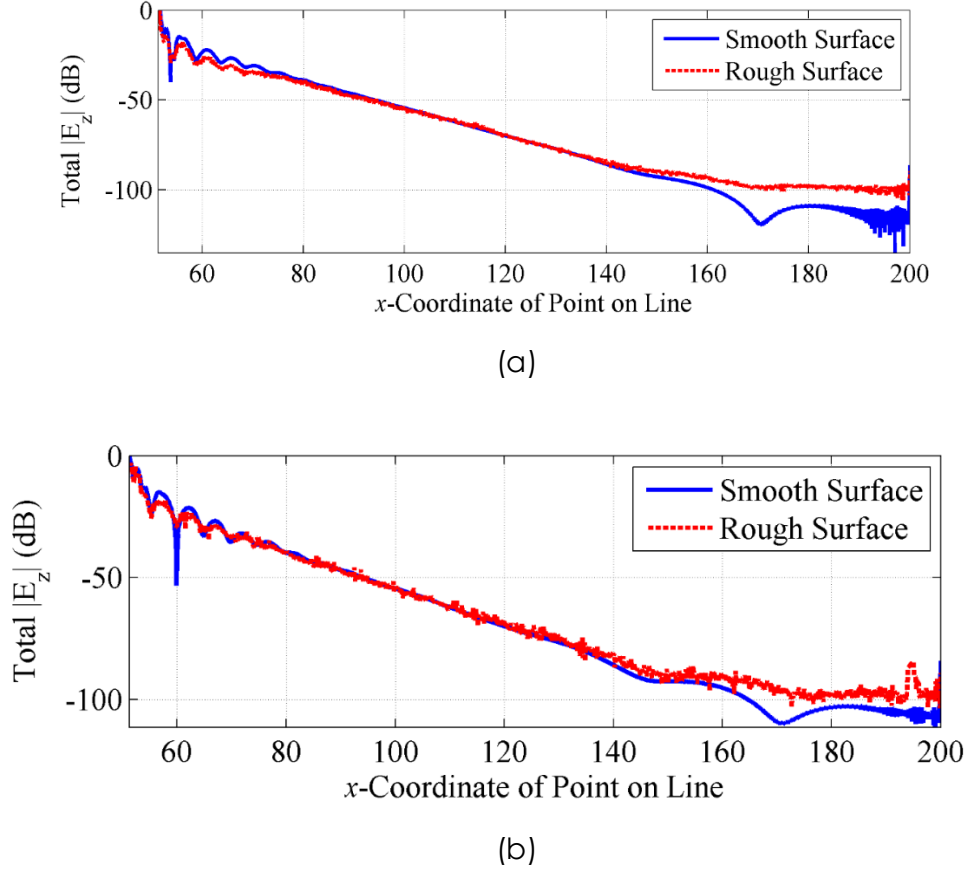


Fig. 3-7: Numerical Results for Rough Straight Entry with Vertically Incident Dipole; (a) Receiver points on the center of the entry; (b) Receiver points on the side of the entry.

#### 3.1.1.3.4 Analysis of Smooth Entry Loaded with Carts

In this example, EM wave propagation in a smooth entry loaded with five perfect electrically conducting (PEC) carts is analyzed at 455 MHz. The dimensions of the entry and surrounding environment for this case again are the same as those in Example 1, except that the length of the entry is now 400 meters [Fig. 3-8]. The mine carts are centered at  $(2.2 + (j-1) \times 80, 0.925, 0.55)$ ,  $j=1, \dots, 5$ ; their bodies are modeled as truncated inverted pyramids [Fig. 3-8]. The dipole generating the incident field is vertically oriented and resides at  $(0.9, 0.9, 0.9)$ ; field receivers are placed along a line connecting points  $(1.0, 0.9, 1.2)$  m and  $(399.9, 0.9, 1.2)$  m. The magnitude of the electric field at the testing points with and without the carts is shown in Fig. 3-9. We notice that the fields in the loaded entry decays faster compared to those in the empty entry especially at receiver points positioned after  $x=100$  m. This suggests that communication channels should be characterized while taking into account mine carts and other objects that inside the mine.

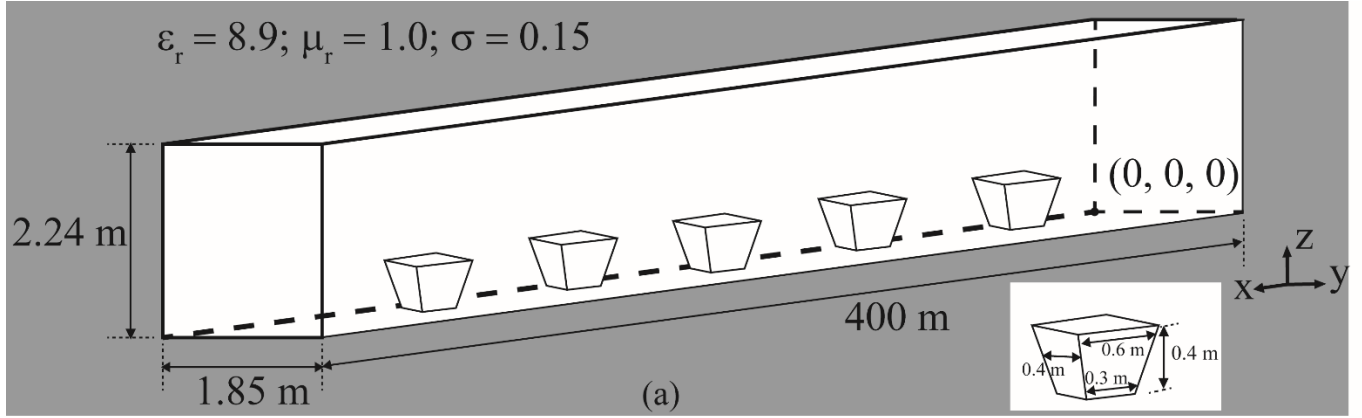


Fig. 3-8: Geometry for the 400-meter long empty entry with carts.

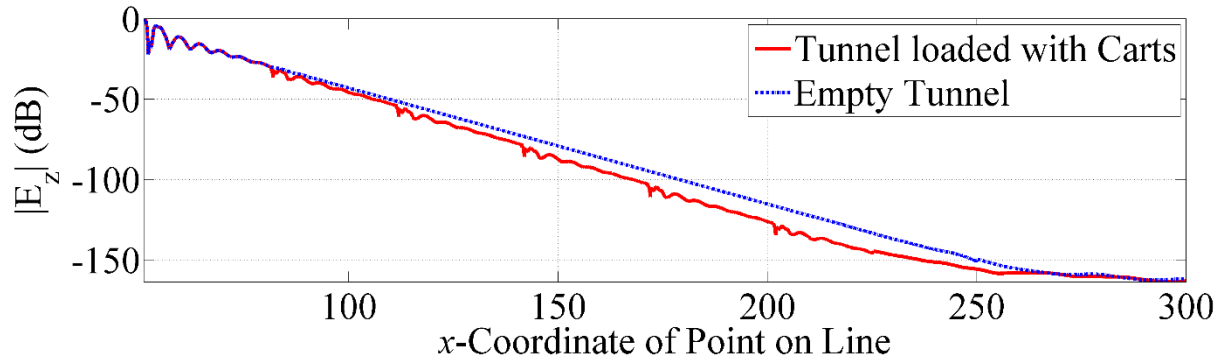


Fig. 3-9: Numerical Results for a 400-meter smooth entry loaded with carts.

### 3.1.1.3.5 Analysis of Mine Gallery

Next, the proposed solver is used to characterize the EM field distribution associated with a wireless network operating an empty mine gallery that consists of six entries. In this gallery, three rectangular entries that run along the  $x$  direction intersected with three entries that run along the  $y$  direction [Fig. 3-10]. The height, width, and length of these rectangular entries are 2.24 m, 1.85 m, and 45.55 m. Two types of subdomains are used to decompose the mine gallery; one is a 5-meter straight subdomain, and the other is an intersection subdomain used to connect the straight subdomains. The wireless network consists of four transmitters operating at 455 MHz, each modeled by a vertical dipole. The locations of the transmitters are (10.925, 13.0, 1.12) m, (22.975, 0.925, 1.12) m, (34.525, 12.825, 1.12) m, and (22.975, 24.43, 1.12) m. In Fig. 3-11 (a)-(e), the electric field amplitudes due to each transmitter and the whole network are shown on the plane  $z = 1.12$  m. The results show that this wireless network provides good signal coverage in the mine gallery when each of the six entries contains at least one transmitter located [Fig. 3-11(e)]. It also shows that the path loss between any pair of transmitters are less than approximately 40 dB, representing good signal connections between transmitters.

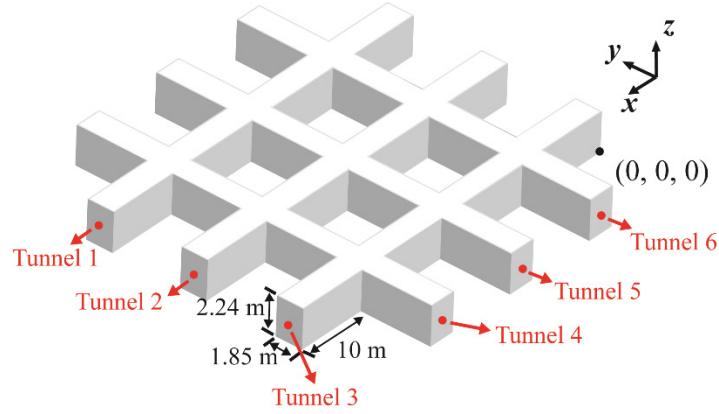


Fig. 3-10: Geometry of gallery

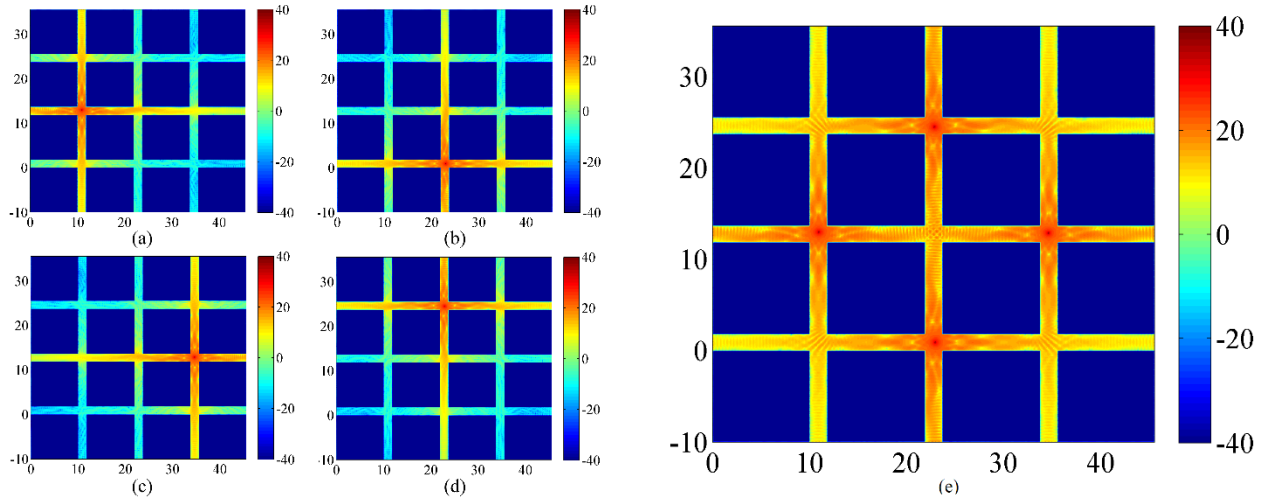


Fig. 3-11: The magnitude of electric fields for each single transmitter (a)-(d) and whole network (e) on observation plane at  $z=1.12$  m in the empty mine gallery computed by the proposed solver.

### 3.1.1.3.6 1000-wavelength Long Entry with Rough Surface and Mine Carts

In this example, EM wave propagation is characterized inside a 1000-wavelength rough entry loaded with mine carts. Specifically, the length of the entry is 350 meters at 915 MHz [Fig. 3-12]. The roughness of the walls has a root mean square (RMS) height and correlation length [29] of 0.1 m and 0.5 m, respectively. For both frequencies, six mine carts are centered at  $(81.5 + (j-1) \times 30, 0.925, 0.55)$ ,  $j = 1, \dots, 6$ . The dimensions of the carts is the same as those in the above example.



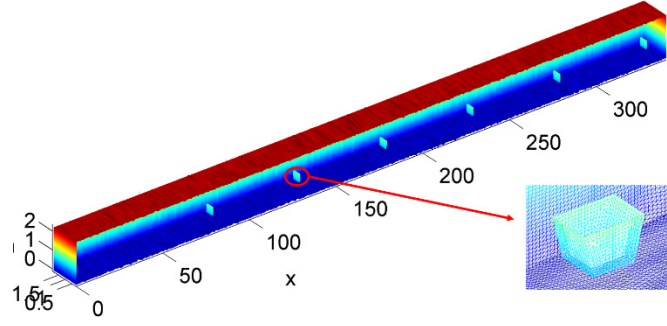


Fig. 3-12: 1000-wavelength entry with rough surfaces and mine carts for 915 MHz (one lateral wall is removed for illustration).

The vertically/horizontally oriented excitation dipole is operated at 915 MHz and located at (50.2, 0.9, 0.9) m. The magnitude of the electric fields are computed at receiver points on a line connecting (51.2, 0.9, 0.9) m and (350, 0.9, 0.9) m for 915 MHz. Fig. 3.13 shows the field distribution. Apparently, the field distribution is no longer as smooth as in an entry with smooth walls and the oscillation of electric fields due to reflections from carts can be observed at testing points where carts are nearby. The results suggest that the rough walls and mining equipment can affect the wave propagation significantly and should be included in EM analysis of an entry.

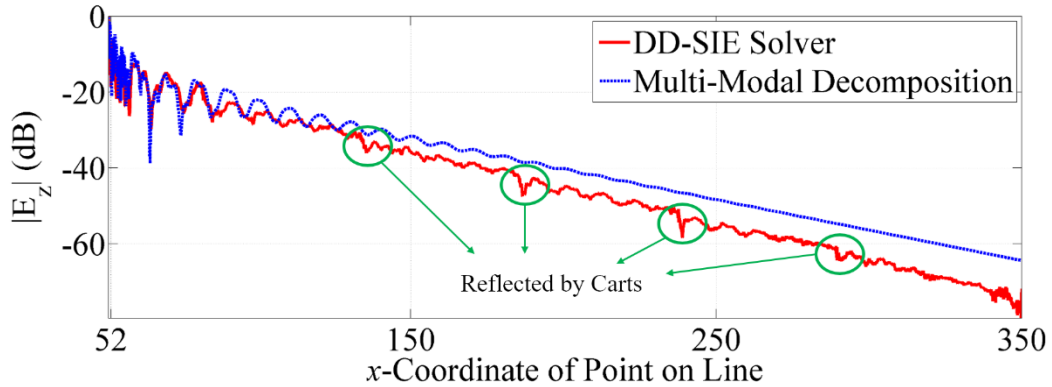


Fig. 3-13: The magnitude of electric fields computed by the proposed solver and multi-modal decomposition for 915 MHz.

### 3.1.2 Tucker Decomposition Enhanced FMM-FFT Simulator

#### 3.1.2.1 Introduction

This section presents a fast, full-wave, CPU and memory efficient 3D SIE technique for analyzing EM wave propagation in electrically large and realistically loaded mine environments. The technique complements the above-described DD-based SIE simulator, and is used for analyzing mine environments loaded with equipment, such as rails, cables, etc., and for environments that are electrically small. The technique leverages Müller and combined field SIEs to model scattering from mine walls and perfect electrically conducting (PEC) objects residing inside mine entries and galleries. The naive iterative solution of such SIEs requires  $O(N^2)$  CPU and memory



resources. Here  $N$  is the number of basis functions used to discretize current densities on the mine walls and PEC objects. These requirements are prohibitive even when characterizing moderately sized entries and galleries. Therefore, the proposed simulator leverages a fast multipole method – fast Fourier transform (FMM-FFT) acceleration scheme [31] with  $O(N^{4/3} \log^{2/3} N)$  CPU and memory resources [32] when applied to mine environments of arbitrary layout, and  $O(N \log N)$  resources when applied to straight long entries or mine galleries populated with dense posts [31]. When applied to the analysis of EM propagation in mine environments, FMM-FFT accelerated SIE simulators tend to be memory- as opposed to CPU-limited. The simulators' memory requirements derive from the requirement to store (i) near-field interaction matrices, (ii) matrices that characterize far-field signatures of basis functions, and (iii) tensors that hold *FFT'*ed translation operators on a structured grid. The proposed simulator compresses the first two and third data structures via singular value decompositions (SVD) and their higher-dimensional counterpart, Tucker decompositions [39], respectively. These compression schemes enable the application of the FMM-FFT accelerated SIE simulator to the analysis of EM wave propagation in much larger and complex mine environments.

This section is organized as follows: it first introduces the Müller-CFIE and the Tucker decomposition enhanced FMM-FFT acceleration scheme. Next, the accuracy, efficiency, and applicability of the proposed simulator are demonstrated via the analysis of EM wave propagation in a 600m long arched entry loaded with conductors, a mine gallery consisting of eight rectangular entries, and a 1500-wavelength long rectangular entry with rough walls and loaded with mine carts.

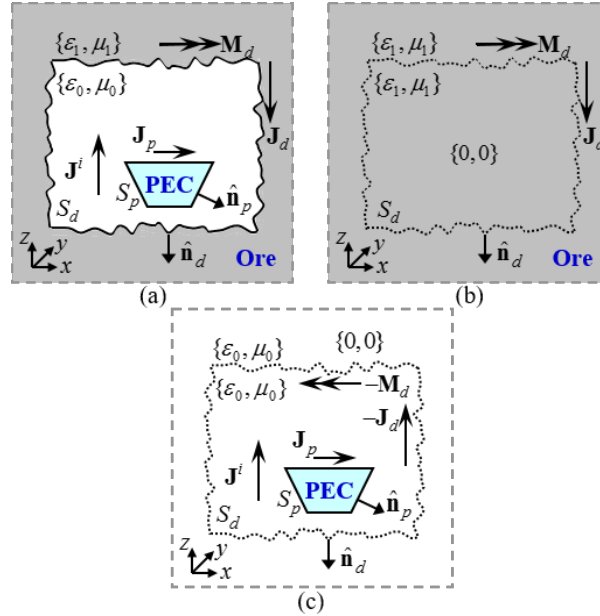


Fig. 3-14 (a) Generic entry geometry for Müller-combined field SIE formulation. (a) Original problem. (b) Equivalent exterior problem. (c) Equivalent interior problem.

### 3.1.2.2 Formulation

This section details the Müller and combined field SIEs and their numerical solution via the method of moments (MoM). It also elucidates the proposed SVD and Tucker-enhanced FMM-FFT acceleration scheme.

#### A) SIEs and Their Discretization

Let  $S_d$  denote the walls of a closed mine entry or gallery, which is surrounded by unbounded lossy rock with permittivity and permeability (medium 1). The entry or gallery is assumed to be filled by air with permittivity and permeability (medium 0) [Fig. 3-14 (a)]. (Note: the scheme detailed below can be trivially modified for entries and galleries filled by dust with permittivity different from .) Let represent the arbitrarily shaped open or closed surfaces of PEC objects (e.g., mine carts, cables or other equipment) residing inside . and are excited by the incident EM field that is generated by a transmitter's electric current density (e.g., an electric dipole) residing within [Fig. 3-14 (a)]. The interaction of with and gives rise to electric and magnetic current densities, and on and electric current densities, on .

To compute  $\mathbf{J}_d(\mathbf{r})$ ,  $\mathbf{M}_d(\mathbf{r})$ , and  $\mathbf{J}_p(\mathbf{r})$ , the surface equivalence principle is invoked to construct the exterior and interior problems illustrated in Fig. 3.14(b)-(c). In the exterior problem [Fig. 3.14(b)],  $\mathbf{J}_d(\mathbf{r})$  and  $\mathbf{M}_d(\mathbf{r})$  radiate in medium 1 and generate total and zero electric and magnetic fields exterior and interior to  $S_d$ , respectively. Imposing boundary conditions on the tangential components of electric and magnetic fields on  $S_d$  yields the following exterior electric field integral equation (EFIE) and magnetic field integral equation (MFIE):

$$0 = (0.5\mathbf{M}_d(\mathbf{r}) - \hat{\mathbf{n}}_d \times \mathfrak{R}_1[\mathbf{M}_d(\mathbf{r})]) + \hat{\mathbf{n}}_d \times \mathfrak{I}_1[\mathbf{J}_d(\mathbf{r})] , \quad (3.31)$$

$$0 = \hat{\mathbf{n}}_d \times \mathfrak{I}_1[\mathbf{M}_d(\mathbf{r})]/\eta_1^2 + (-0.5\mathbf{J}_d(\mathbf{r}) + \hat{\mathbf{n}}_d \times \mathfrak{R}_1[\mathbf{J}_d(\mathbf{r})]) , \quad (3.32)$$

$\mathbf{r} \in S_d$ . Here,  $\hat{\mathbf{n}}_d$  is the outward normal to  $S_d$ ,  $\eta_a = (\mu_a/\epsilon_a)^{0.5}$  with  $\mathbf{a} \in \{0,1\}$  is the wave impedance, and the source-field operators  $\mathfrak{I}_a[\cdot]$  and  $\mathfrak{R}_a[\cdot]$  are

$$\mathfrak{I}_a[\mathbf{X}(\mathbf{r})] = -j\omega\mu_a \int_S (\bar{\mathbf{I}} + \frac{\nabla\nabla'}{k_a^2}) \cdot \mathbf{X}(\mathbf{r}') G_a(\mathbf{r}, \mathbf{r}') d\mathbf{r}' , \quad (3.33)$$

$$\mathfrak{R}_a[\mathbf{X}(\mathbf{r})] = \nabla \times \int_S \mathbf{X}(\mathbf{r}') G_a(\mathbf{r}, \mathbf{r}') d\mathbf{r}' , \quad (3.34)$$

where the integral in (3.34) is evaluated in principle value sense. Here  $G_a(\mathbf{r}, \mathbf{r}') = \exp(-jk_a |\mathbf{r} - \mathbf{r}'|)/(4\pi |\mathbf{r} - \mathbf{r}'|)$  is the scalar Green's function,  $k_a = \omega(\mu_a\epsilon_a)^{0.5}$ ,  $\omega = 2\pi f$ ,  $f$  is the frequency, and  $\mathbf{r}$  and  $\mathbf{r}'$  denote observation and source locations on support  $S$ , respectively.

In the interior problem [Fig. 3.14(c)],  $-\mathbf{J}_d(\mathbf{r})$  and  $-\mathbf{M}_d(\mathbf{r})$  radiate alongside  $\mathbf{J}^i(\mathbf{r})$  and  $\mathbf{J}_p(\mathbf{r})$  in air and generate total and zero electric and magnetic fields interior and exterior to  $S_d$ , respectively. Imposing boundary conditions for tangential electric and magnetic fields on  $S_d$  and  $S_p$  yields the following interior EFIE and MFIE for  $S_d$  and interior EFIE and MFIE for  $S_p$  :

$$\hat{\mathbf{n}}_d \times \mathbf{E}^i(\mathbf{r}) = -(0.5\mathbf{M}_d(\mathbf{r}) + \hat{\mathbf{n}}_d \times \mathfrak{R}_0[\mathbf{M}_d(\mathbf{r})]) + \hat{\mathbf{n}}_d \times \mathfrak{I}_0[\mathbf{J}_d(\mathbf{r})] - \hat{\mathbf{n}}_d \times \mathfrak{I}_0[\mathbf{J}_p(\mathbf{r})] , \quad \mathbf{r} \in S_d , \quad (3.35)$$

$$\hat{\mathbf{n}}_d \times \mathbf{H}^i(\mathbf{r}) = \hat{\mathbf{n}}_d \times \mathfrak{I}_0[\mathbf{M}_d(\mathbf{r})]/\eta_0^2 + (0.5\mathbf{J}_d(\mathbf{r}) + \hat{\mathbf{n}}_d \times \mathfrak{R}_0[\mathbf{J}_d(\mathbf{r})]) - \hat{\mathbf{n}}_d \times \mathfrak{R}_0[\mathbf{J}_p(\mathbf{r})] , \quad \mathbf{r} \in S_d , \quad (3.36)$$

$$\hat{\mathbf{t}}_p \cdot \mathbf{E}^i(\mathbf{r}) = \hat{\mathbf{t}}_p \cdot \left( -\Re_0[\mathbf{M}_d(\mathbf{r})] + \Im_0[\mathbf{J}_d(\mathbf{r})] - \Im_0[\mathbf{J}_p(\mathbf{r})] \right), \quad \mathbf{r} \in S_p, \quad (3.37)$$

$$\hat{\mathbf{n}}_p \times \eta_0 \mathbf{H}^i(\mathbf{r}) = \hat{\mathbf{n}}_p \times \Im_0[\mathbf{M}_d(\mathbf{r})]/\eta_0 + \hat{\mathbf{n}}_p \times \eta_0 \Re_0[\mathbf{J}_d(\mathbf{r})] + \eta_0 \left( 0.5 \mathbf{J}_p(\mathbf{r}) - \hat{\mathbf{n}}_p \times \Re_0[\mathbf{J}_p(\mathbf{r})] \right), \quad \mathbf{r} \in S_p. \quad (3.38)$$

Here  $\hat{\mathbf{n}}_p$  and  $\hat{\mathbf{t}}_p$  are the outward pointing unit normal and arbitrary unit vector tangential to  $S_p$ , respectively. Exterior and interior EFIEs for  $S_d$  in (3.31) and (3.35) can be linearly combined after multiplying them by  $\alpha_1$  and  $\alpha_0$ , respectively, as

$$\begin{aligned} \hat{\mathbf{n}}_d \times \alpha_0 \mathbf{E}^i(\mathbf{r}) = & 0.5(\alpha_1 - \alpha_0) \mathbf{M}_d(\mathbf{r}) - \hat{\mathbf{n}}_d \times \left( \alpha_1 \Re_1[\mathbf{M}_d(\mathbf{r})] + \alpha_0 \Re_0[\mathbf{M}_d(\mathbf{r})] \right) \\ & + \hat{\mathbf{n}}_d \times \left( \alpha_1 \Im_1[\mathbf{J}_d(\mathbf{r})] + \alpha_0 \Im_0[\mathbf{J}_d(\mathbf{r})] \right) - \hat{\mathbf{n}}_d \times \alpha_0 \Im_0[\mathbf{J}_p(\mathbf{r})]. \end{aligned} \quad (3.39)$$

Similarly, exterior and interior MFIEs for  $S_d$  can be multiplied by  $\beta_1$  and  $\beta_0$ , respectively, and combined as

$$\begin{aligned} \hat{\mathbf{n}}_d \times \beta_0 \mathbf{H}^i(\mathbf{r}) = & \hat{\mathbf{n}}_d \times \left( \frac{\beta_1}{\eta_1^2} \Im_1[\mathbf{M}_d(\mathbf{r})] + \frac{\beta_0}{\eta_0^2} \Im_0[\mathbf{M}_d(\mathbf{r})] \right) + 0.5(\beta_0 - \beta_1) \mathbf{J}_d(\mathbf{r}) \\ & + \hat{\mathbf{n}}_d \times \left( \beta_1 \Re_1[\mathbf{J}_d(\mathbf{r})] + \beta_0 \Re_0[\mathbf{J}_d(\mathbf{r})] \right) - \hat{\mathbf{n}}_d \times \beta_0 \Re_0[\mathbf{J}_p(\mathbf{r})]. \end{aligned} \quad (3.40)$$

Finally, linearly combining the  $\alpha_p$  times interior EFIE and  $(1 - \alpha_p)$  times interior MFIE for  $S_p$  yields

$$\begin{aligned} \hat{\mathbf{t}}_p \cdot \alpha_p \mathbf{E}^i(\mathbf{r}) + \hat{\mathbf{n}}_p \times \eta_0 (1 - \alpha_p) \mathbf{H}^i(\mathbf{r}) = & \left( -\hat{\mathbf{t}}_p \cdot \alpha_p \Re_0[\mathbf{M}_d(\mathbf{r})] + \hat{\mathbf{n}}_p \times (1 - \alpha_p) / \eta_0 \Im_0[\mathbf{M}_d(\mathbf{r})] \right) \\ & + \left( \hat{\mathbf{t}}_p \cdot \alpha_p \Im_0[\mathbf{J}_d(\mathbf{r})] + \hat{\mathbf{n}}_p \times \eta_0 (1 - \alpha_p) \Re_0[\mathbf{J}_d(\mathbf{r})] \right) \\ & + \left( -\hat{\mathbf{t}}_p \cdot \alpha_p \Im_0[\mathbf{J}_p(\mathbf{r})] + \eta_0 (1 - \alpha_p) \left( 0.5 \mathbf{J}_p(\mathbf{r}) - \hat{\mathbf{n}}_p \times \Re_0[\mathbf{J}_p(\mathbf{r})] \right) \right) \end{aligned} \quad (3.41)$$

Equations (3.39)-(3.41) with  $\alpha_1 = \varepsilon_1$ ,  $\alpha_0 = -\varepsilon_0$ ,  $\beta_1 = \mu_1$ ,  $\beta_0 = -\mu_0$ , and  $0 \leq \alpha_p \leq 1$  are known as Müller-combined field SIE formulation [40] and can be solved simultaneously for  $\mathbf{M}_d(\mathbf{r})$ ,  $\mathbf{J}_d(\mathbf{r})$ , and  $\mathbf{J}_p(\mathbf{r})$  via the MoM. (Note: In this study,  $\alpha_p$  is set to 0.2 and 1 for closed and open PEC surfaces, respectively.) To this end,  $\mathbf{M}_d(\mathbf{r})$ ,  $\mathbf{J}_d(\mathbf{r})$ , and  $\mathbf{J}_p(\mathbf{r})$  are approximated in terms of Rao-Wilton-Glisson (RWG) basis functions  $\mathbf{f}_n(\mathbf{r})$  [41] as

$$\mathbf{M}_d(\mathbf{r}) = \sum_{n=1}^{N_d} I_n \mathbf{f}_n(\mathbf{r}), \quad \mathbf{J}_d(\mathbf{r}) = \sum_{n=N_d+1}^{2N_d} I_n \mathbf{f}_n(\mathbf{r}), \quad (3.42)$$

$$\mathbf{J}_p(\mathbf{r}) = \sum_{n=2N_d+1}^{2N_d+N_p} I_n \mathbf{f}_n(\mathbf{r}), \quad (3.43)$$

where  $I_n$ ,  $n=1, \dots, 2N_d+N_p$ , are unknown expansion coefficients. Substituting (3.42) and (3.43) into (3.39)-(3.41) and applying Galerkin testing to the resulting equations with  $\mathbf{f}_m(\mathbf{r})$ ,  $m=1, \dots, 2N_d+N_p$ , yields the linear system of equations of dimension  $N=2N_d+N_p$

$$\bar{\mathbf{Z}} \mathbf{I} = \mathbf{V}, \quad (3.44)$$

where  $\bar{\mathbf{Z}}$  is the MoM matrix, and  $\mathbf{I}$  and  $\mathbf{V}$  are vectors of unknown expansion coefficients and tested incident EM fields, respectively. When analyzing electrically large mine entries and galleries loaded with conductors that require large  $N$ , the solution of the matrix system in [42] cannot be obtained using classical algebraic solvers. To mitigate the computational and

memory requirements of the iterative solution of [42], we deploy the SVD and Tucker enhanced FMM-FFT scheme described next.

### B) SVD and Tucker Enhanced FMM-FFT Algorithm

1) *FMM-FFT Algorithm.* FMM-FFT scheme introduces a hypothetical box enclosing the mesh of  $S_d$  (and hence  $S_p$ ). This large box is split into  $N_x$ ,  $N_y$ , and  $N_z$  smaller boxes along the  $x$ ,  $y$ , and  $z$  directions [Fig. 3.15]. The resulting boxes are denoted by  $B_u$  with indices  $\mathbf{u}=(u_x, u_y, u_z)$ ,  $u_x=1, \dots, N_x$ ,  $u_y=1, \dots, N_y$ ,  $u_z=1, \dots, N_z$ , and centered at  $\mathbf{r}_u$  that coincide with the points of a uniform 3D grid [Fig. 3.15]. All boxes that contain triangle pairs of source/testing basis functions,  $\mathbf{f}_n(\mathbf{r}) / \mathbf{f}_m(\mathbf{r})$ , are termed “groups” and enclosed by a sphere of radius  $R^s$ . Two groups  $B_u$  and  $B_{u'}$  constitute a near-field pair if the distance between their centers  $R_{uu'}=|\mathbf{R}_{uu'}|=|\mathbf{r}_{u'}-\mathbf{r}_u|$  is smaller than a prescribed threshold, i.e.  $R_{uu'} < \kappa R^s$  ( $\kappa$  is selected as 4 in this study); otherwise, they form a far-field pair. Interactions between basis functions in the same group and near-field pairs are directly computed via (3.39)-(3.41) and stored, resulting in the first large data structure mentioned in the introduction. A large portion of this data structure is pertinent to interactions between basis functions in near-field pairs and compressed by SVD, as elucidated in the next subsection. The contributions of self and near-field interactions to the result of each matrix-vector multiplication required by the iterative solution of (3.44) are directly computed. The interactions between basis functions in far-field pairs are computed by the FMM-FFT algorithm. To this end, first, the far-field patterns of source basis functions  $\mathbf{P}^+(\hat{\mathbf{k}}_a^{pq}, \mathbf{f}_n)$  with

$$\mathbf{P}^+(\hat{\mathbf{k}}_a^{pq}, \mathbf{c}) = \int_{S_c} \exp(\pm j k_a \hat{\mathbf{k}}_a^{pq} \cdot (\mathbf{r} - \mathbf{r}_u)) (\bar{\mathbf{I}} - \hat{\mathbf{k}}_a^{pq} \hat{\mathbf{k}}_a^{pq}) \cdot \mathbf{c}(\mathbf{r}) d\mathbf{r} \quad (3.45)$$

are computed and stored for all directions  $\hat{\mathbf{k}}_a^{pq} = (\sin \theta^p \cos \phi^q, \sin \theta^p \sin \phi^q, \cos \theta^p)$ ,  $p=1, \dots, K_a+1$ ,  $q=1, \dots, 2K_a+1$ . Here,  $\theta^p$  are the inverse cosine of abscissas of  $(K_a+1)^{\text{th}}$ -order Gauss-Legendre quadrature rule,  $\phi^q = q2\pi/(2K_a+1)$ ,  $K_a = 2k_a R^s + 1.8(\log_{10}(1/\gamma_1))^{2/3} (2k_a R^s)^{1/3}$  is the number of multipoles for medium  $a=\{0,1\}$ ,  $\gamma_1$  is the number of desired accurate digits in the FMM approximation [43],  $S_c$  is the support of  $\mathbf{c}(\mathbf{r})$ , and  $\mathbf{u}$  corresponds to the box containing  $\mathbf{c}(\mathbf{r})$ . Since  $\bar{\mathbf{I}}$  is unit dyad,  $\theta$  and  $\phi$  components of far-field patterns are computed [43]. Note that only the far-field patterns of source basis functions discretizing  $\mathbf{J}_d(\mathbf{r})$  and  $\mathbf{J}_p(\mathbf{r})$  are computed and stored for both media and only air (medium 0), respectively; the ones pertinent to  $\mathbf{M}_d(\mathbf{r})$  can be directly obtained from those related to  $\mathbf{J}_d(\mathbf{r})$  by invoking the duality and thereby are not stored. Similarly, the receiving patterns of testing functions used to test electric and magnetic fields on  $S_d$ ,  $\mathbf{P}^-(\hat{\mathbf{k}}_a^{pq}, \hat{\mathbf{n}}_d \times \mathbf{f}_m)$ , and electric and magnetic fields on  $S_p$ ,  $\mathbf{P}^-(\hat{\mathbf{k}}_a^{pq}, \mathbf{f}_m)$  and  $\mathbf{P}^-(\hat{\mathbf{k}}_a^{pq}, \hat{\mathbf{n}}_p \times \mathbf{f}_m)$ , are computed and stored for both media and only air, respectively. These operations give rise to the second large data structure alluded to in the introduction, which is compressed by SVD as explained in the next subsection. During matrix-vector multiplication, the far-fields of basis functions in each group are summed to construct all groups' outgoing far-field patterns for both media as

$$\mathcal{F}_u(\hat{\mathbf{k}}_a^{pq}) = \sum_{n \in B_u} \mathbf{P}^+(\hat{\mathbf{k}}_a^{pq}, \mathbf{f}_n) \alpha_n c I_n, \quad (3.46)$$

$p=1, \dots, K_a+1$ ,  $q=1, \dots, 2K_a+1$ ,  $a \in \{0,1\}$ . Here  $c$  is -1 for far-field patterns of basis functions used to discretize  $\mathbf{J}_p(\mathbf{r})$  and 1 otherwise. (Note: far-field patterns of basis functions discretizing  $\mathbf{J}_p(\mathbf{r})$  are not computed/stored for medium 1 and not included in summation in (3.46) for  $a=1$ .) Next, for each  $\hat{\mathbf{k}}_a^{pq}$ , these far-field patterns  $\mathcal{F}_u(\hat{\mathbf{k}}_a^{pq})$  are convolved via FFT with the translation tensor  $\mathcal{T}_{u'-u}(\hat{\mathbf{k}}_a^{pq})$  to obtain all groups' incoming plane wave spectra  $\mathcal{G}_u(\hat{\mathbf{k}}_a^{pq})$  as

$$\mathcal{G}_{\mathbf{u}'}(\hat{\mathbf{k}}_a^{pq}) = \Psi^{-1}(\mathcal{T}_{\mathbf{u}'-\mathbf{u}}(\hat{\mathbf{k}}_a^{pq})\Psi(\mathcal{F}_{\mathbf{u}}(\hat{\mathbf{k}}_a^{pq}))). \quad (3.47)$$

Here  $\Psi$  is the FFT operator,  $\mathcal{T}_{\mathbf{u}'-\mathbf{u}}(\hat{\mathbf{k}}_a^{pq}) = \Psi(\mathcal{T}_{\mathbf{u}'-\mathbf{u}}^{\sim}(\hat{\mathbf{k}}_a^{pq}))$  is the tensor that stores *FFT'*ed translation operator values and

$$\mathcal{T}_{\mathbf{u}'-\mathbf{u}}^{\sim}(\hat{\mathbf{k}}_a^{pq}) = \frac{k_a^2 \eta_a}{16\pi^2} \sum_{l=1}^{K_a} (-j)^l (2l+1) h_l^{(2)}(k_a R_{\mathbf{u}'\mathbf{u}}) \Phi_l(\hat{\mathbf{R}}_{\mathbf{u}'\mathbf{u}} \cdot \hat{\mathbf{k}}_a^{pq}). \quad (3.48)$$

where  $\hat{\mathbf{R}}_{\mathbf{u}'\mathbf{u}} = \mathbf{R}_{\mathbf{u}'\mathbf{u}} / R_{\mathbf{u}'\mathbf{u}}$ ,  $\Phi_l(\cdot)$  is the Legendre polynomial of degree  $l$  and  $h_l^{(2)}$  denotes the spherical Hankel function of the second kind. All  $\mathcal{T}_{\mathbf{u}'-\mathbf{u}}(\hat{\mathbf{k}}_a^{pq})$  computed and stored for all directions constitute the third large data structure mentioned in the introduction and can be compressed via Tucker decomposition [39], as explained in the next subsection. In practice, the circular convolution in (3.47) for each  $\hat{\mathbf{k}}_a^{pq}$  is performed as follows. First,  $\mathcal{T}_{\mathbf{u}'-\mathbf{u}}(\hat{\mathbf{k}}_a^{pq})$  is computed by Fourier transforming  $\mathcal{T}_{\mathbf{u}'-\mathbf{u}}^{\sim}(\hat{\mathbf{k}}_a^{pq})$  with indices  $u'_x = -N_x + 1, \dots, N_x$ ,  $u'_y = -N_y + 1, \dots, N_y$ ,  $u'_z = -N_z + 1, \dots, N_z$ , ( $u'_x, u'_y, u'_z \neq 0$ ) and  $\mathbf{u} = (1, 1, 1)$ . Second,  $\mathcal{T}_{\mathbf{u}'-\mathbf{u}}(\hat{\mathbf{k}}_a^{pq})$  is multiplied with the Fourier transform of  $\mathcal{F}_{\mathbf{u}}(\hat{\mathbf{k}}_a^{pq})$  with indices  $u_x = 1, \dots, N_x$ ,  $u_y = 1, \dots, N_y$ ,  $u_z = 1, \dots, N_z$ , after the dimensions of  $\mathcal{F}_{\mathbf{u}}(\hat{\mathbf{k}}_a^{pq})$  are increased to  $(2N_x - 1) \times (2N_y - 1) \times (2N_z - 1)$  by zero padding. After computing all  $\mathcal{G}_{\mathbf{u}'}(\hat{\mathbf{k}}_a^{pq})$ , those are projected onto the testing basis functions and far-field contributions to the matrix-vector multiplication in (3.44) are computed by summing over all directions with quadrature weights  $\omega_a^{pq}$  as

$$\sum_{a=0}^1 \sum_{p=1}^{K_a+1} \sum_{q=1}^{2K_a+1} w_a^{pq} \mathbf{P}^{-}(\hat{\mathbf{k}}_a^{pq}, \hat{\mathbf{n}}_d \times \mathbf{f}_m) \cdot \mathcal{G}_{\mathbf{u}'}(\hat{\mathbf{k}}_a^{pq}), \quad 1 \leq m \leq N_d, \quad (3.49)$$

$$\sum_{a=0}^1 \sum_{p=1}^{K_a+1} \sum_{q=1}^{2K_a+1} w_a^{pq} \left( \mathbf{P}^{-}(\hat{\mathbf{k}}_a^{pq}, \hat{\mathbf{n}}_d \times \mathbf{f}_m) \times \hat{\mathbf{k}}_a^{pq} \right) \cdot \mathcal{G}_{\mathbf{u}'}(\hat{\mathbf{k}}_a^{pq}) (\beta_a / \alpha_a), \quad (3.50)$$

$$N_d + 1 \leq m \leq 2N_d$$

$$\sum_{p=1}^{K_0+1} \sum_{q=1}^{2K_0+1} w_0^{pq} / \alpha_0 \left( \alpha_p \mathbf{P}^{-}(\hat{\mathbf{k}}_0^{pq}, \mathbf{f}_m) - (1 - \alpha_p) \right. \\ \left. \mathbf{P}^{-}(\hat{\mathbf{k}}_0^{pq}, \hat{\mathbf{n}}_p \times \mathbf{f}_m) \times \hat{\mathbf{k}}_0^{pq} \right) \cdot \mathcal{G}_{\mathbf{u}'}(\hat{\mathbf{k}}_0^{pq}), \quad 2N_d + 1 \leq m \leq N \quad (3.51)$$

To execute the FMM-FFT algorithm on high-performance parallel computers for characterizing large scale mine entries/galleries loaded with conductors, a hybrid spatial/angular parallelization strategy, which utilizes hybrid message passing interface/open multiprocessing (MPI/OpenMP) standards, is deployed. This parallelization strategy, described in Appendix II, uniformly partitions the memory and computational loads along angular dimension (i.e., plane-wave directions) and spatial dimension (i.e., groups) among processors. Such parallelization strategy introduces two additional processor-to-processor communications compared to the spatial partitioning strategy in [44]. These additional communications require negligible time when non-blocking MPI operations are used. On the other hand, the hybrid spatial/angular parallelization strategy permits scalable workload partitioning of compression of far-field patterns, while the spatial parallelization strategy in [44] does not.

*2) SVD and Tucker Decomposition Enhancements.* To reduce the memory requirement of the SIE simulator leveraging FMM-FFT algorithm, large data structures storing the near-field interactions, far-field (and receiving) patterns of basis functions, and *FFT'*ed translation operator tensors are compressed via SVD and its higher-dimensional counterpart Tucker decomposition.

*Compression of near-field interaction matrices:* Assume that the near-field interactions between  $N_s$  source basis functions in a group  $B_s$  and  $N_t$  testing basis functions in a group  $B_u$  are stored in a matrix  $\bar{\mathbf{Q}}$  with dimensions  $N_t \times N_s$ , which is a rank deficient block of MoM matrix with entries  $\bar{Z}_{mn}$ ,  $m \in B_u$ ,  $n \in B_s$ , and can be compressed via truncated SVD (TrSVD( $\cdot$ )) as

$$\bar{\mathbf{Q}} \approx \text{TrSVD}(\bar{\mathbf{Q}}) = \bar{\mathbf{U}} \bar{\mathbf{\Sigma}} \bar{\mathbf{V}}^*, \quad (3.52)$$

where  $*$  stands for conjugate transpose,  $\bar{\mathbf{U}}$  and  $\bar{\mathbf{V}}$  are truncated unitary matrices with dimensions  $N_t \times r$  and  $N_s \times r$ , respectively, and  $\bar{\mathbf{\Sigma}}$  is the diagonal matrix with descending  $r$  singular values of  $\bar{\mathbf{Q}}$ ,  $\delta_i$ ,  $i=1, \dots, r$ , which are greater than a prescribe tolerance  $\gamma_2$  times the value of first singular value, i.e.  $\delta_i \geq \gamma_2 \delta_1$ ,  $i=1, \dots, r$ . During setup stage, truncated SVD compression is applied to all MoM matrix blocks that stores the near-field interactions between groups, but not applied to full rank blocks pertinent to self interactions of groups. During the iterative solution of (3.44), the reduced representations in (3.52) are directly used without restoring the full block  $\bar{\mathbf{Q}}$  to compute the contributions of near-field interactions to the matrix vector multiplication.

*Compression of matrices holding far-field patterns:* Assume that one component ( $\theta$  or  $\phi$ ) of far-field (or receiving) pattern of a basis function for a medium  $a \in \{0, 1\}$  is stored in a matrix  $\bar{\mathbf{W}}$  with dimensions  $(K_a + 1) \times (2K_a + 1)$ , which tabulates the farfield samples along elevation and azimuthal directions through its rows and columns, respectively. Given the prescribed tolerance  $\gamma_3$ ,  $\bar{\mathbf{W}}$  can be approximated by its truncated SVD as

$$\bar{\mathbf{W}} \approx \text{TrSVD}(\bar{\mathbf{W}}) \quad (3.53)$$

This operation is applied to  $\theta$  and  $\phi$  components of all basis functions' far-field and receiving patterns for both media. The resulting truncated unitary matrices and singular values obtained and stored during setup stage are used to restore the far-field and receiving patterns one-by-one during the iterative solution of (3.44).

*Compression of FFT'ed translation operator tensors:* The tensor storing the FFT'ed translation operator samples for each  $\hat{\mathbf{k}}_a^{pq}$ ,  $\mathcal{T}_{u'-u}$ , has dimensions  $D_1 \times D_2 \times D_3 = (2N_x - 1) \times (2N_y - 1) \times (2N_z - 1)$  and can be compressed via Tucker decomposition as [45]

$$\mathcal{T}_{u'-u} \approx \mathcal{X} \times_1 \bar{\mathbf{U}}_1 \times_2 \bar{\mathbf{U}}_2 \times_3 \bar{\mathbf{U}}_3, \quad (3.54)$$

where  $\mathcal{X}$  is the core tensor with dimensions  $r_1 \times r_2 \times r_3$ ,  $\bar{\mathbf{U}}_i$ ,  $i=1, \dots, 3$ , denote the factor matrices with dimensions  $D_i \times r_i$ ,  $i=1, \dots, 3$ , and  $\times_i$ ,  $i=1, \dots, 3$ , stands for the  $i$ -mode matrix product of a tensor, which can be performed as explained in [46]. The core tensor and factor matrices are obtained via the following procedure: (i) The unfolding matrices of  $\mathcal{T}_{u'-u}$ ,  $\bar{\mathbf{T}}_i$ ,  $i=1, \dots, 3$ , are formed. (Note: An example of forming unfolding matrices of a tensor is given in Eqn. 2.1. of [46].) (ii) Given the prescribed tolerance  $\gamma_4/\sqrt{3}$ , the truncated SVDs of unfolding matrices,  $\text{TrSVD}(\bar{\mathbf{T}}_i) = \bar{\mathbf{U}}_i \bar{\mathbf{\Sigma}}_i \bar{\mathbf{V}}_i^*$ ,  $i=1, \dots, 3$ , are obtained. The resulting truncated unitary matrices  $\bar{\mathbf{U}}_i$ ,  $i=1, \dots, 3$ , are the factor matrices of (3.54). (iii) The core tensor can be obtained via

$$\mathcal{X} = \mathcal{T}_{u'-u} \times_1 \bar{\mathbf{U}}_1^* \times_2 \bar{\mathbf{U}}_2^* \times_3 \bar{\mathbf{U}}_3^*. \quad (3.55)$$

The core tensors and factor matrices of *FFT'*ed translation operator tensors for all  $\hat{\mathbf{k}}_a^{pq}$  directions are obtained during the setup stage and used to restore  $\mathcal{T}_{u'-u}$  one  $\hat{\mathbf{k}}_a^{pq}$  at a time during the iterative solution stage.

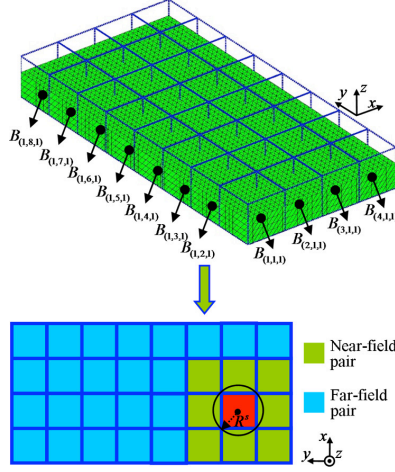


Fig. 3-15 Partitioning a fictitious box enclosing the mesh of an example structure into small boxes and tabulating near/far-field pairs of a selected group  $B_{(2,2,1)}$  in FMM-FFT scheme.

### 3.1.2.3 Code Validation

The proposed EM simulator is verified and validated by comparing its numerical results to (i) an analytical model and (ii) measurement data. See Section 3.1.3 for details.

#### 3.1.2.3.1 Comparison to Analytical Model

To compare the results obtained by the multi-modal method and our proposed EM simulator, EM wave propagation is characterized in a rectangular empty entry at 455 and 915 MHz. The length of the entry is 200 meters. To demonstrate the applicability of the proposed simulator, the medium surrounding the entry is chosen different for the two frequencies. At 455 MHz, the entry is surrounded by a low-loss medium with relative permittivity  $\epsilon_r = 3.0$ , relative permeability  $\mu_r = 1.0$ , and conductivity  $\sigma = 0.001 \text{ S/m}$  [Fig. 3-16(a)]; at 915 MHz, the medium is highly lossy with relative permittivity  $\epsilon_r = 8.9$ , relative permeability  $\mu_r = 1.0$ , and conductivity  $\sigma = 1.5 \text{ S/m}$  [Fig. 3-16(b)]. The transmitting dipole is vertically polarized and located at  $(50.0, 0.925, 1.12) \text{ m}$  for both frequencies. The magnitudes of electric fields in the  $z$ -direction are computed at receiver points on a line connecting  $(51.0, 0.925, 1.12) \text{ m}$  and  $(200, 0.925, 1.12) \text{ m}$ . It is apparent from Fig. 3.17(a)-(b) that the electric fields computed by the proposed simulator and the multi-mode decomposition method are in good agreement, which demonstrates its accuracy. It should be noted that the tail of the electric fields computed by the EM simulator are oscillating, which is due to standing-wave phenomena caused by reflections at the end of the entry.

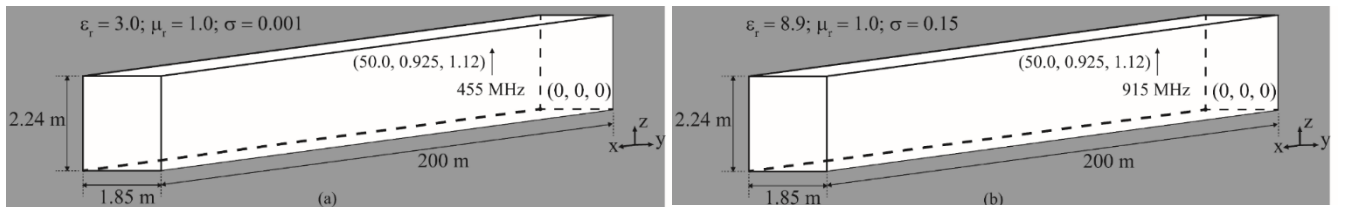


Fig. 3-16 Geometry for a 200-meter entry with incident dipole operated at (a) 455 MHz and (b) 915 MHz.



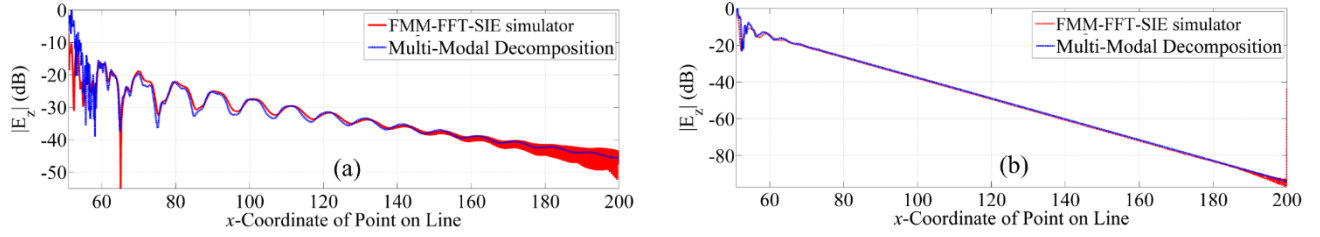
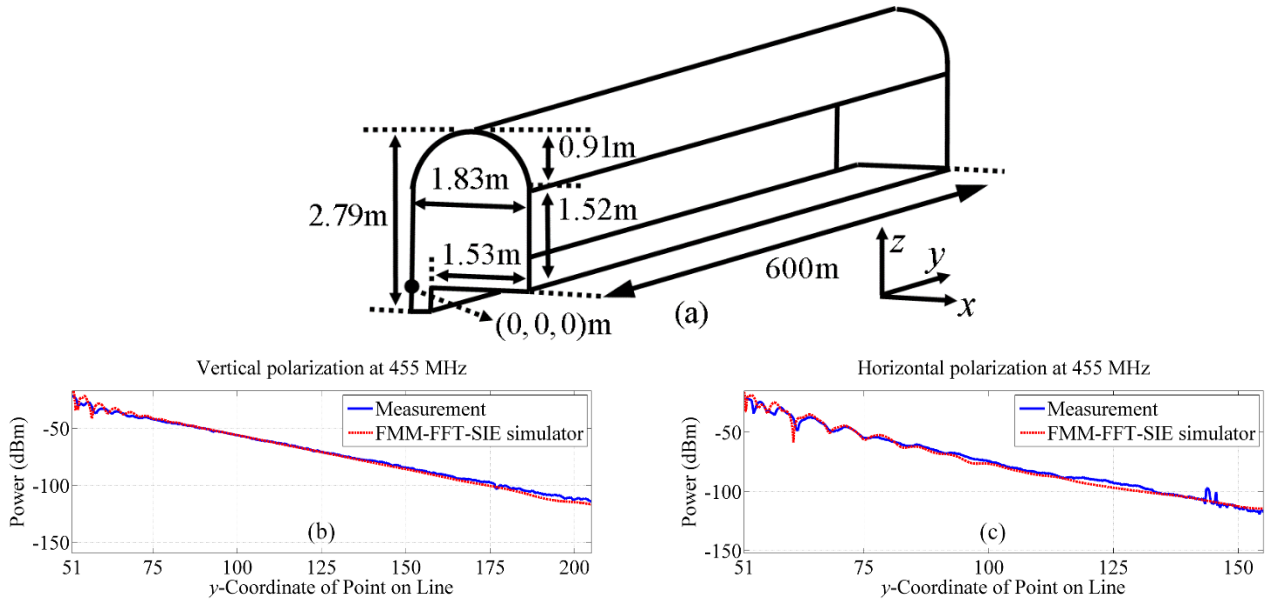


Fig. 3-17: Comparison between the proposed EM simulator and the multi-modal decomposition method at (a) 455 MHz and (b) 915 MHz.

### 3.1.2.3.2 Comparison to Measurement Data

To compare with measurement data, the proposed simulator is used to characterize wave propagation in an arched entry [Fig. 3-18(a)]. A transmitting electric dipole with unit moment is positioned at  $(0.915, 50, 1.22)$  m and power densities are computed at receiver locations spaced 10 cm apart along lines inside the entry. The entry itself is surrounded by rock with relative permittivity  $\epsilon_r = 8.9$ , relative permeability  $\mu_r = 1.0$ , and conductivity  $\sigma = 0.15$  S/m. An empty 600m-long arched entry is excited by an electric dipole that is either  $z$ - (vertically) or  $x$ - (horizontally) oriented and operated at 455 MHz or 915 MHz (4 cases) [Fig. 3-18 (a)]; at the lower and higher frequency, entry walls are discretized using  $N=15,208,572$  and  $N=61,502,286$  RWG basis functions, respectively. For each case, power densities are computed at receivers on the line connecting  $(0.915, 51, 1.22)$  m and  $(0.915, 600, 1.22)$  m. Computed power densities are compared with measured data [37, 38] following normalization to account for uncertainties/differences in the excitation mechanism [Fig. 3-18 (b)-(e)]. Computed and measured power densities are in good agreement thereby validating the accuracy of the simulator. Moreover, the magnitudes of the computed electric current density on the entry walls for each orientation of the transmitting dipole and frequency are displayed in Figs. 3-18 (f)-(i); their decay along the entry is consistent with the decay of power density.





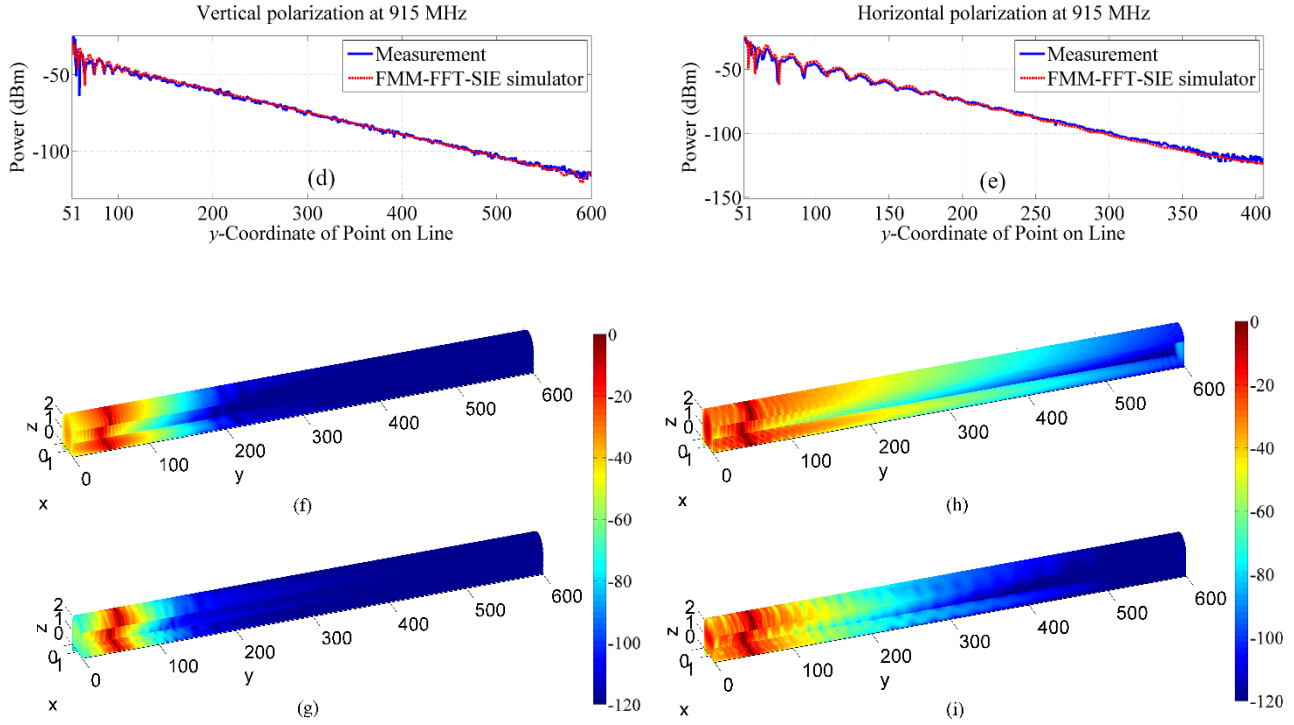


Fig. 3-18: (a) The geometry of an empty 600m-long arched entry (the lateral wall is removed for illustration). The power values on receiver points computed by the proposed simulator and obtained by measurements at 455 MHz for (b) vertical and (c) horizontal polarizations and at 915 MHz for (d) vertical and (e) horizontal polarizations. Electric current density on entry walls computed by the proposed solver at 415 MHz for (f) vertical and (g) horizontal polarizations and at 915 MHz for (h) vertical and (i) horizontal polarizations (in dB scale).

### 3.1.2.3.3 Analysis of Mine Gallery

Next, the proposed solver is used to characterize EM wave propagation in an empty mine gallery formed by eight rectangular entries [Fig. 3-19].

All entries are surrounded by rock with relative permittivity  $\epsilon_r = 3$ , relative permeability  $\mu_r = 1$ , and conductivity  $\sigma = 0.001 \text{ S/m}$ . The gallery is excited by an electric dipole with unit moment that is centered at  $(7.5, 15.91, 1.12) \text{ m}$ ,  $z$ - (vertically) or  $y$ - (horizontally) oriented, and operated at 455 MHz. Walls are discretized using  $N = 15,766,560$  RWG basis functions. For each polarization, computed normalized power densities at receivers spaced 10 cm apart positioned along four lines in the  $x$ -directed entries connecting  $(8.5, y, 1.12) \text{ m}$  to  $(81.5, y, 1.12) \text{ m}$  with  $y$  set to 15.91, 32.73, 49.55, and 66.37 are displayed in Fig. 3-20 (a) and (b).

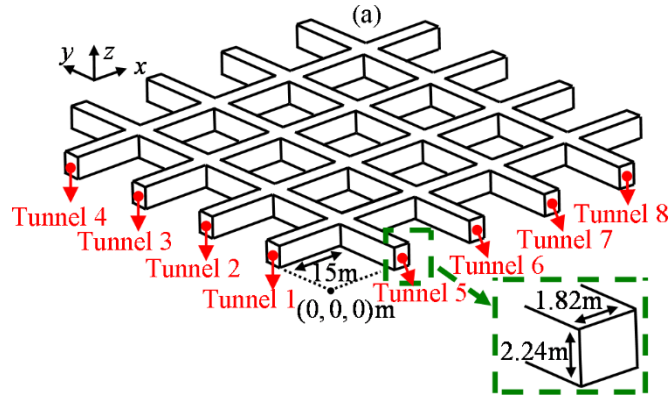
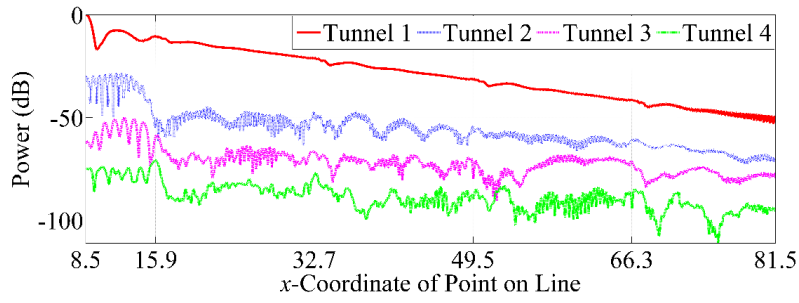
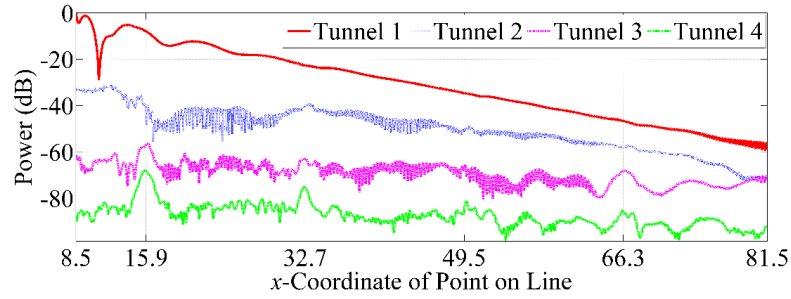


Fig. 3-19: The geometry of a mine gallery formed by eight entries.



(a)



(b)

Fig. 3-20: The power values at receiver points on lines in entry 1, 2, 3, and 4 computed by the proposed EM solver at 455 MHz for (a) vertical and (b) horizontal polarizations.

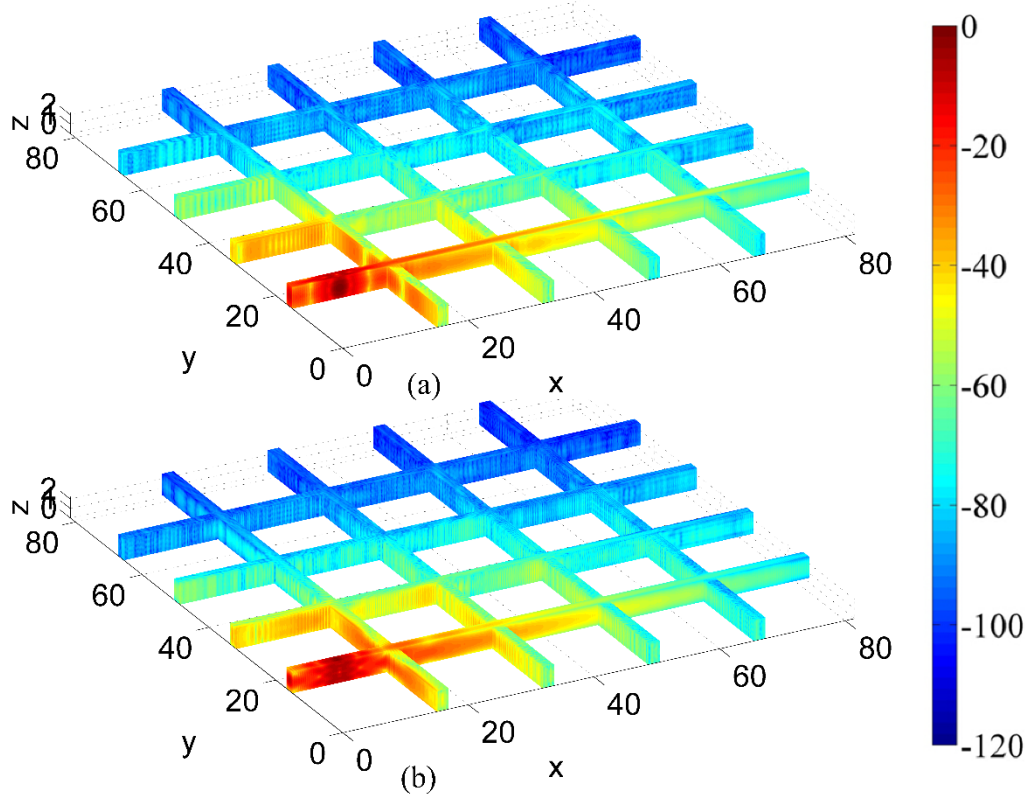


Fig. 3-21: Electric current density on entry walls computed by the proposed solver at 455 MHz for (a) vertical and (b) horizontal polarizations.

The following observations are in order:

- (i) In entry 2, power densities at receivers with  $x$ -coordinates less than 15.91 m are always larger than the those at receivers with  $x$ -coordinates greater than 15.91 m [Fig 3-20 (a) and (b)]. Slight or no decay is observed for receivers with  $x$ -coordinates less than 15.91 m as direct coupling from the transmitter to these receiver points occurs through the low-loss rock.
- (ii) Small or large spikes appear for the power values around the receiver points with  $x$ -coordinates 15.9 m, 32.7 m, 49.5 m, and 66.3 m in entries 3 and 4 [Fig 3-20 (a) and (b)]. Note that these receiver points reside at the intersections of entries 3 and 4 with entries 5, 6, 7, and 8 and the spikes are due to the contributions of EM waves guided in entries 5, 6, 7, and 8. Additionally, computed electric current densities on gallery walls for each polarization are displayed in Fig. 3-21 (a)-(b); these plots are consistent with the above power density observations.

Table 3-2 presents the memory savings obtained by the Tucker decomposition and the total CPU time of the simulation for vertical and horizontal polarized dipoles. The results demonstrate that the Tucker compression is able to yield 86.8% reduction in memory requirements. The CPU time for the two cases are 11.42 and 12.37 hours, respectively. For comparison purposes, the CPU times of a PMCHWT-based solver [5] for the same cases are also obtained. It is apparent that the proposed solver is 3-4 times faster than conventional PMCHWT-based solvers.

Methods	Muller-CFIE		PMCHWT
Memory saving at 455 MHz (%)	86.8		86.8
CPU Time (hours)	v-pol	12.37	38.85
	h-pol	11.42	36.71

Table 3-2, Memory savings and computational overhead in gallery simulation

#### 3.1.2.3.4 Analysis of 1500-Wavelength Entry with Rough Walls and loaded with Metal Carts

Next, the proposed solver is applied to the characterization of EM wave propagation in a 1500-wavelength entry with rough walls that is loaded with mine carts. Specifically, the length of the entry is 1000 meters at 455 MHz and 500 meters at 915 MHz [Fig. 3-22 (a) and (b)]. The entries are surrounded by lossy rock with relative permittivity  $\epsilon_r = 8.9$ , relative permeability  $\mu_r = 1.0$ , and conductivity  $\sigma = 0.15 \text{ S/m}$ . The roughness of the entry walls is characterized by root mean square (RMS) height and correlation length of 0.1 m and 0.5 m, respectively. PEC carts are modeled as truncated inverted pyramids [Fig. 3-22]. For both frequencies, six mine carts are centered at  $(81.5 + (j-1) \times 30, 0.925, 0.55)$ ,  $j = 1, \dots, 6$ .

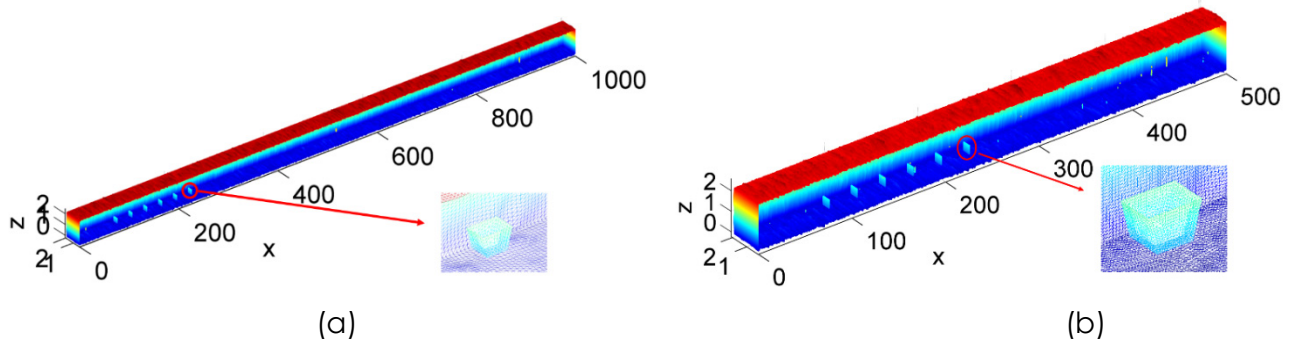
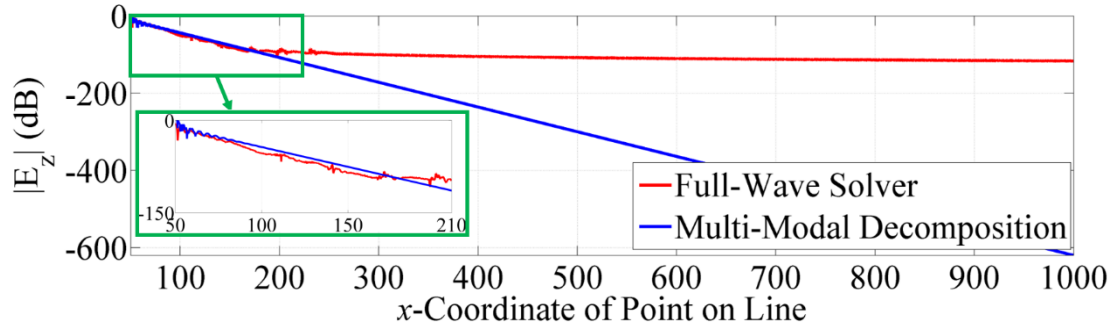
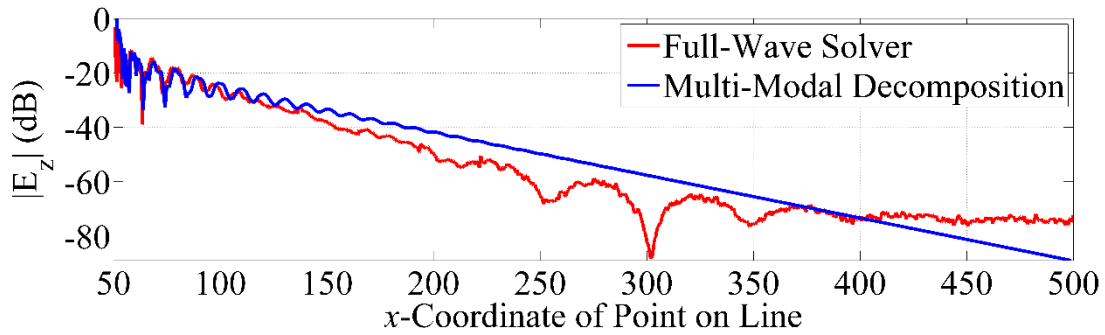


Fig. 3-22: 1500-wavelength entry with rough surfaces and mine carts for (a) 455 MHz case and (b) 915 MHz case (one lateral wall is removed for illustration).

The vertically oriented excitation dipole is operated at 455 and 915 MHz and located at  $(50.0, 0.925, 1.12)$  m. The magnitudes of electric fields are computed at receiver points on lines connecting  $(51.0, 0.925, 1.12)$  m and  $(1000, 0.925, 1.12)$  m for 455 MHz and  $(51.0, 0.925, 1.12)$  m and  $(500, 0.925, 1.12)$  m for 915 MHz. Figs. 3-23 (a) and (b) show the field distribution for the 455 MHz and 915 MHz cases. Apparently, the field distribution computed by the proposed solver has a faster decay rate than that computed by the multi-modal decomposition. The spikes and fluctuations shown in the electric fields curve are due to the reflections from metal carts. The results suggest that the rough walls and mining equipment can affect the wave propagation significantly and should be included in the analysis of wireless systems in entries.



(a)



(b)

Fig. 3-23: The magnitude of electric fields computed by the proposed solver and multi-modal decomposition for (a) 455 MHz and (b) 915 MHz.

### 3.1.2.3.5 Analysis of a Curved Entry of Larger Cross Section

Finally, we apply the proposed simulator to the analysis of wave propagation in a curved tunnel. The entry's cross section measures 4.26m x 2.13m (width x height). The entry is excited by a z directed dipole operated at 455 MHz. The mine wall's permittivity is set to 3-0.03950572j. The entry's radius of curvature is 213m which is the 50 times more than the width of entry (or 100 times more than the height of entry); the fact that the entry is gently curved allows for the application of multimodal decomposition methods. Fig. 3-24 shows the magnitude of the electric field computed by the proposed solver and multi-modal decomposition along the entry. Results are in good agreement.

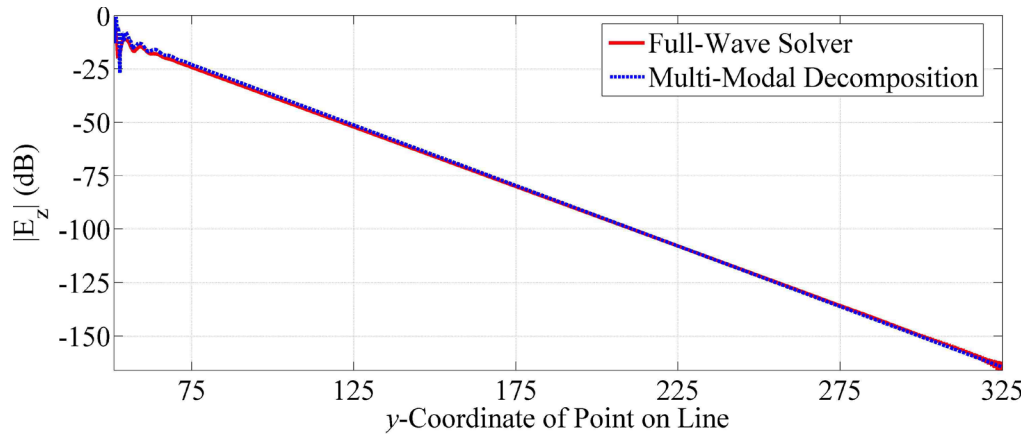


Fig. 3-24: The magnitude of electric fields computed by the proposed solver and multi-modal decomposition along the entry.

### 3.1.3 Concluding Remarks / Lessons Learned

We successfully developed, implemented, and validated new full-wave EM simulators for analyzing wireless signal propagation in realistic mine environments.

The proposed solvers apply to nearly arbitrary environments. They make no assumption regarding the shape of entry cross sections, their extent/length, the roughness of the mine walls, or the electric properties of the surrounding material, or the mining and communication equipment present in the mine. They also apply across many frequency regimes. These properties set the new simulators apart from all prior methods.

The computational methodologies underpinning the solvers derive from fast surface integral equation techniques developed in the 1990s and 2000s for the purpose of analyzing radar cross sections of stealth aircraft. As such, they are highly accurate and capable of predicting signals with very large dynamic range, spanning distances from a transmitter to receivers where signals are down in excess of 150 dB (in practice this means no reception). Compared to existing technologies, the proposed solvers remain expensive to execute. Most results included in this report were obtained on a computing cluster with roughly 1,000 cores. We note that such computing resources are readily available from commercial cloud providers. The solvers are capable of analyzing structures larger than those shown here using additional computational resources.

The simulators were applied to a wide range of entry and gallery geometries (rectangular and arched entries with smooth and rough walls, curved entries, and galleries involving up to eight entries). Our simulations demonstrate the need to account for the shape of entry cross sections, the presence of mining equipment, and wall roughness when analyzing signal coverage. That said, we caution against generalizing our results as the quantification of effects depends on the specifics of the case studied.

## 3.2 Objective 2: UQ Method Development

Many unknowns affect the propagation of EM waves in mine environments: examples include the material properties and surface roughness of the (lossy) rock that surrounds the mine entries and galleries; the shape, material composition, and positions of the mining equipment, trolleys, and rails; and the positions and orientations of transmitting and receiving antennas. This section describes techniques for calculating statistics of key observables, e.g., the *Probability Density Function\** (PDF) of the electric field at a receiver, given a parametric description of these uncertainties.

Quantification of uncertainties in EM analysis is most frequently performed via Monte Carlo (MC) methods. Classical MC methods require the evaluation of observables using EM simulators for many deterministic realizations of the system and its excitation, which are sampled as random variables with known/assumed *probability density function\** (PDF). Although classic MC methods can be simply implemented with EM simulators to provide the statistical moments and PDFs of the observables, they often converge quite slowly and require a large number of deterministic EM simulations to yield reliable statistical data. This slow convergence limits the applicability of classic MC methods to the uncertainty quantifications of EM phenomena in complex and large-scale mine environments, for which each deterministic simulation (using the above described techniques) requires significant CPU resources. This section outlines a family of UQ methods that are far more powerful than the basic MC method.

All methods discussed below take as input:

- All inputs required by the above-described simulators – see introduction to Section 3.1.
- A list of all unknown/uncertain quantities (e.g. the x, y , and z-coordinates of a transmitter), and the assumed or known PDF for each of them. If the probability density function is not known or cannot be estimated, but if bounds on the quantity are known, we oftentimes assume the quantity is uniformly distributed over the interval set by the bounds.
- A list of quantities of interest (also called “observables”). Oftentimes these are electric and magnetic fields and power densities at receivers.

All methods produce:

- PDFs of the quantities of interest. The maximum of the PDF indicates the most likely value of an observable. Its spread is indicative of the degree of uncertainty. When computing PDFs of received power densities, the spread also can be indicative of the likelihood of signal fading.

### 3.2.1 Polynomial Chaos (PC) and Multi-Element Polynomial Chaos (ME-PC) Methods

Assume that unknown parameters (material properties and surface roughnesses of the (lossy) rock that surrounds the mine entries and galleries; the shape, material composition, and positions of the mining equipment, trolleys, and rails; and the positions and orientations of transmitting and receiving antennas) are parametrized by an  $N_{\text{dof}}$ -dimensional vector  $\mathbf{x} = [x^1, x^2, \dots, x^{N_{\text{dof}}}]$ ,  $\mathbf{x} \in \Omega = \prod_{i=1}^{N_{\text{dof}}} \Omega^i$  where each random variable  $x^i$  resides in domain  $\Omega^i = [a^i, b^i]$ .

Let  $F(\mathbf{x})$  represent the electric field at a receiver, or any other observable deemed important in the design of a wireless communication network. Its statistical characterization *in principle*

could proceed by applying MC, that is by evaluating  $F(\mathbf{x})$  for many  $\mathbf{x}$ 's sampled according to the (assumed/known) pdfs of the random variables. Unfortunately, MC methods converge very slowly, all but ruling out the use of a CPU-intensive full-wave EM simulator to compute  $F(\mathbf{x})$ . To circumvent this difficulty, we apply MC methods to an approximate representation or surrogate model of  $F(\mathbf{x})$  constructed using the ME-PC method.

The ME-PC method leverages generalized polynomial chaos (gPC) expansions to construct a surrogate model from orthogonal polynomials. PC and stochastic collocation (SC) methods are rapidly gaining traction for the purpose of statistically characterizing EM phenomena. They are non-intrusive, that is they can use existing deterministic simulators to generate surrogate models via multivariate integration rules. Unfortunately, classically gPC or SC generated surrogate models lack accuracy when the observable exhibits rapid variations across the random domain  $\Omega$ , as do electric fields in mine environments. To address this shortcoming, the ME-PC method adaptively and recursively divides the random domain  $\Omega$  into subdomains using the decay rate of the relative error in the gPC expansion as a guide. While constructing a low-order local gPC approximation on each subdomain, the FMM-FFT-based EM simulator is used to compute the observable/electric field values at integration (collocation) points dictated by an efficient multivariate integration rule. In what follows, the PC method is reviewed first. The ME-PC method for adaptively constructing local and low-order polynomial approximations to  $F(\mathbf{x})$  is explained next.

The PC method relies on constructing gPC expansion via multivariate orthogonal Legendre polynomials  $\Psi(\mathbf{x})$  as

$$F(\mathbf{x}) = \sum_{m=0}^{N_p} f_m \Psi_m(\mathbf{x}). \quad (3.56)$$

Here,  $N_p = (N_{\text{dof}} + p)! / (N_{\text{dof}}! p!) - 1$ ,  $p$  is the order of the expansion, and  $f_m$  is the  $m^{\text{th}}$  gPC expansion coefficient expressed as

$$f_m = \int_{\Omega} F(\mathbf{x}) \Psi_m(\mathbf{x}) d\mathbf{x}. \quad (3.57)$$

The  $N_{\text{dof}}$ -dimensional integral in (3.57) is evaluated numerically using tensor product (TP) or sparse grid (SG) integration rules. The reason for selecting Legendre polynomials to expand  $F(\mathbf{x})$  is that they lead to exponential/optimal convergence of the gPC expansion in (3.56) for random variables that are uniformly distributed as assumed in this study.

Unfortunately, when the observable varies rapidly in the random variables, the gPC expansion in (1) becomes inefficient as it requires polynomials of very high order to yield sufficient accuracy. The ME-PC method circumvents this bottleneck by recursively and adaptively dividing the initial random domain  $\Omega$  into subdomains  $\tilde{\Omega}$ ,  $\tilde{\Omega} = \prod_{i=1}^{N_{\text{dof}}} \tilde{\Omega}^i$ , with  $\tilde{\Omega}^i = [\tilde{a}^i, \tilde{b}^i]$ , using the decay rates of  $F(\mathbf{x})$ 's local variances as a guide [9, 10], and using the gPC expansion in (3.56) with low-order polynomials within each subdomain to locally approximate  $F(\mathbf{x})$ . The local variance of  $F(\mathbf{x})$  in  $\tilde{\Omega}$  is approximated by that of the  $p^{\text{th}}$ -order gPC expansion as

$$\text{var}_p[F(\mathbf{x})] = \sum_{m=1}^{N_p} \tilde{f}_m^2. \quad (3.58)$$

Here,  $\tilde{f}_m$  is the  $m^{\text{th}}$  coefficient of the gPC expansion constructed in  $\tilde{\Omega}$  and is computed using (3.57). The decay rate of the local gPC expansion's relative error is defined as  $\gamma = (\text{var}_p[F(\mathbf{x})] - \text{var}_{p-1}[F(\mathbf{x})]) / \text{var}_p[F(\mathbf{x})]$ . The subdomain  $\tilde{\Omega}$  is selected for adaptive refinement in case  $\gamma^{\tau_1} J > \varepsilon_1$ , where  $\varepsilon_1$  and  $\tau_1$  are the desired tolerance and a user-defined constant ( $0 < \tau_1 \leq 1$



), respectively;  $J$  is the ratio of the volume of  $\tilde{\Omega}$  to that of  $\Omega$ . The refinement is performed along dimensions in which  $F(\mathbf{x})$  varies rapidly. The sensitivity of each dimension in  $\tilde{\Omega}$  is defined as  $\alpha^i = \tilde{f}^i / (\text{var}_p[F(\mathbf{x})] - \text{var}_{p-1}[F(\mathbf{x})])$ , where  $\tilde{f}^i$  stands for the coefficient of the  $p^{\text{th}}$ -order gPC expansion that applies to the  $i^{\text{th}}$  dimension. Refinement is performed along the  $i^{\text{th}}$  dimension if  $\alpha^i \geq \tau_2 \cdot (\max_{i=1, \dots, N_{\text{dof}}} \alpha^i)$ , where  $\tau_2$  is a user-defined constant ( $0 < \tau_2 \leq 1$ ). The adaptive and recursive application of this procedure generates  $N_d$  non-overlapping subdomains  $\tilde{\Omega}_j = \prod_{i=1}^{N_{\text{dof}}} \tilde{\Omega}_j^i$ ,  $j=1, \dots, N_d$ , with  $\tilde{\Omega}_j^i = [\tilde{a}_j^i, \tilde{b}_j^i]$ , which do not need refinement. Using the gPC coefficients of such subdomains,  $\tilde{f}_{m,j}$ , the global mean of  $F(\mathbf{x})$  over  $\Omega$  can be approximated as

$$E[F(\mathbf{x})] \cong \sum_{j=1}^{N_d} \tilde{f}_{0,j} J_j \quad (3.59)$$

where  $J_j = \prod_{i=1}^{N_{\text{dof}}} (\tilde{b}_j^i - \tilde{a}_j^i) / (b^i - a^i)$  and  $\tilde{f}_{0,j}$  denotes the 0<sup>th</sup> order coefficient in the  $p^{\text{th}}$ -order local gPC expansion (in  $\tilde{\Omega}_j$ ). Similarly, the global variance of  $F(\mathbf{x})$  over  $\Omega$  can be computed using

$$\text{var}[F(\mathbf{x})] \cong \sum_{j=1}^{N_d} [\sum_{m=1}^{N_p} \tilde{f}_{m,j}^2 + (\tilde{f}_{0,j} - E[F(\mathbf{x})])^2] J_j. \quad (3.60)$$

The pdf of  $F(\mathbf{x})$  can be estimated by applying an MC method to the surrogate model obtained using local gPC coefficients of  $N_d$  non-overlapping subdomains.

### 3.2.2 High Dimensional Model Representations

To further reduce the cost of the above PC and ME-PC UQ methods, we propose to hybridize them with high dimensional model representation (HDMR) methods [18, 54]. The HDMR method reduces the cost of the surrogate model construction by iteratively including only the component functions pertinent to the “most important” random variables. The component functions, which are approximated by the multi-element probabilistic collocation (ME-PC) method [18], can represent either individual or combined contributions of random variables to the observables.

#### 3.2.2.1 HDMR Formulation

Let  $\mathbf{x} = [x^1, x^2, \dots, x^{N_{\text{dof}}}]$  denote a random vector defined over a domain  $D$ . Each element in  $\mathbf{x}$  is a random variable that has a known PDF and parameterizes an uncertain quantity in the mine environments. The HDMR expansion approximates an unknown function  $V(\mathbf{x})$ , which represents an observable in mine communication systems, in terms of component functions as

$$V(\mathbf{x}) = \sum_{\mathbf{u} \subseteq \Omega} V_{\mathbf{u}}(\mathbf{x}^{\mathbf{u}}), \quad (3.61)$$

where  $\Omega = \{1, \dots, N_{\text{dof}}\}$  is the general set of random variable indices,  $\mathbf{u}$  is a subset of  $\Omega$ , i.e.  $\mathbf{u} \subseteq \Omega$ , and  $|\mathbf{u}|$  denotes the cardinality of subset  $\mathbf{u}$ .  $\mathbf{x}^{\mathbf{u}}$  is a  $|\mathbf{u}|$ -dimensional random vector and  $V_{\mathbf{u}}(\mathbf{x}^{\mathbf{u}})$  represents the component functions defined over  $D$ . For example, for  $\mathbf{u} = \emptyset$ ,  $V_{\mathbf{u}}(\mathbf{x}^{\mathbf{u}}) = V_{\emptyset}(\mathbf{x}^{\emptyset}) = V_0$  is the zeroth-order component function which is constant over  $D$ ; for  $\mathbf{u} = \{1\}$ ,  $V_{\mathbf{u}}(\mathbf{x}^{\mathbf{u}}) = V_1(x^1)$  is the first-order component function that represents the individual contribution of  $x^1$  to  $V(\mathbf{x})$ . The HDMR construction can be better described by an example. Assume that  $N_{\text{dof}} = 3$  and  $\Omega = \{1, 2, 3\}$ , all possible subsets of  $\Omega$ ,  $\mathbf{u}$  and all component functions  $V_{\mathbf{u}}(\mathbf{x}^{\mathbf{u}})$  corresponding to these possible subsets are given in Table 3-3.

Subset, $\mathbf{u}$	$V_{\mathbf{u}}(\mathbf{x}^{\mathbf{u}})$	$ \mathbf{u} $
----------------------	-------------------------------------------	----------------

$\emptyset$	$V_0$	1
$\{1\}$	$V_1(x^1)$	1
$\{2\}$	$V_2(x^2)$	1
$\{3\}$	$V_3(x^3)$	1
$\{1,2\}$	$V_{12}(x^1, x^2)$	2
$\{1,3\}$	$V_{13}(x^1, x^3)$	2
$\{2,3\}$	$V_{23}(x^2, x^3)$	2
$\{1,2,3\}$	$V_{123}(x^1, x^2, x^3)$	3

Table 3-3 The correspondence between subsets of  $\Omega = \{1,2,3\}$  and the component functions used to build HDMR expansion and the cardinalities of subsets.

For this example, one can construct the HDMR expansion in (3.61) using the component functions given in Table 3-2 as

$$\begin{aligned}
 V(\mathbf{x}) = & V_0 + V_1(x^1) + V_2(x^2) + V_3(x^3) + V_{12}(x^1, x^2) \\
 & + V_{13}(x^1, x^3) + V_{23}(x^2, x^3) + V_{123}(x^1, x^2, x^3).
 \end{aligned} \tag{3.62}$$

The advantage of such construction can be illustrated by selecting an observable that consists of a constant term and monomials such as  $V(\mathbf{x}) = 1 + (x^1)^2 + (x^2)^2 + (x^3)^2$ , (Note: the indices (or superscripts) of random variables are written inside parentheses while their powers are intentionally left outside to avoid confusion). The component functions  $V_0$ ,  $V_1(x^1)$ ,  $V_2(x^2)$ , and  $V_3(x^3)$  are needed to approximate  $V(\mathbf{x})$  while the remaining component functions in (3.62) are redundant. In many practical communication systems, like in this example, the behavior of observables can be efficiently approximated by including only the low-order component functions. This fact renders the HDMR expansions highly suitable for surrogate model generation of  $V(\mathbf{x})$  that is in high-dimensional random domains but can be approximated by surrogate models constructed in low dimensional domains.

### 3.2.2.2 Component Functions in HDMR

The component functions are expressed in terms of observable values on cuts passing through a reference point  $\bar{\mathbf{x}}$ , i.e.

$$V_u(\mathbf{x}^u) = V(\mathbf{x}^u) \Big|_{\mathbf{x}=\bar{\mathbf{x}} \setminus \mathbf{x}^u} - \sum_{\mathbf{v} \subset \mathbf{u}} V_{\mathbf{v}}(\mathbf{x}^v) \tag{3.63}$$

where  $\mathbf{x} = \bar{\mathbf{x}} \setminus \mathbf{x}^{\mathbf{u}}$  indicates that the random variables with indices that do not belong to subset  $\mathbf{u}$  are set to the corresponding values at reference point  $\bar{\mathbf{x}}$ . The reference point in this study is select as the mass center of  $D$ , i.e.,

$$\bar{\mathbf{x}} = [\bar{x}^1, \dots, \bar{x}^{N_{dof}}] = [(a^1 + b^1) / 2, \dots, (a^{N_{dof}} + b^{N_{dof}}) / 2]. \quad (3.64)$$

The choice of reference point is not unique, it may also be selected as the centroid of SG integration rule [55], as a random point at which the observable value is closest to the global mean [56], or as a random point determined due to the prescribed weights of dimensions [57]. For the example given above, the component functions obtained are given as follows:

$$\begin{aligned} V_0 &= V(\bar{\mathbf{x}}) \\ V_1(x^1) &= V(x^1, \bar{x}^2, \bar{x}^3) - V_0; \\ V_2(x^2) &= V(\bar{x}^1, x^2, \bar{x}^3) - V_0; \\ V_3(x^3) &= V(\bar{x}^1, \bar{x}^2, x^3) - V_0; \\ V_{12}(x^1, x^2) &= V(x^1, x^2, \bar{x}^3) - V_0 - V_1(x^1) - V_2(x^2); \\ V_{13}(x^1, x^3) &= V(x^1, \bar{x}^2, x^3) - V_0 - V_1(x^1) - V_3(x^3); \\ V_{23}(x^2, x^3) &= V(\bar{x}^1, x^2, x^3) - V_0 - V_2(x^2) - V_3(x^3); \\ V_{123}(x^1, x^2, x^3) &= V(x^1, x^2, x^3) - V_0 - V_1(x^1) - V_2(x^2) - V_3(x^3) \\ &\quad - V_{12}(x^1, x^2) - V_{13}(x^1, x^3) - V_{23}(x^2, x^3); \end{aligned} \quad (3.65)$$

To iteratively select the component functions that significantly contribute to observable, the weight associated with the first-order functions are defined as

$$\varsigma_{\mathbf{u}} = |E[V_{\mathbf{u}}(\mathbf{x}^{\mathbf{u}})] / V_0|; |\mathbf{u}| = 1. \quad (3.66)$$

Here,  $E[V_{\mathbf{u}}(\mathbf{x}^{\mathbf{u}})]$  is the means of first-order component functions. In case  $V_0$  is zero, the weight is set to  $E[V_{\mathbf{u}}(\mathbf{x}^{\mathbf{u}})]$ . A component function is assumed to be significant when its associated weight is larger than a prescribed value  $\delta_1$ . During the iterations with the second-order component functions, only those involving the significant first-order component functions are computed and are added to the second-level HDMR expansion only if their associated weights are larger than the prescribed value. This scheme is then repeated for all levels. Note that the weights of component functions at higher levels are defined as

$$\varsigma_{\mathbf{u}} = |E[V_{\mathbf{u}}(\mathbf{x}^{\mathbf{u}})] / \sum_{|\mathbf{v}| < |\mathbf{u}|-1} E[V_{\mathbf{v}}(\mathbf{x}^{\mathbf{v}})]|; |\mathbf{u}| > 1, \quad (3.67)$$

An additional stopping criterion is the decay rate of relative difference  $\kappa$  between observable means computed at two consecutive levels, which is defined as

$$\kappa = \left| \sum_{|\mathbf{v}|=|\mathbf{u}|} E[V_{\mathbf{v}}(\mathbf{x}^{\mathbf{v}})] - \sum_{|\mathbf{v}| < |\mathbf{u}|-1} E[V_{\mathbf{v}}(\mathbf{x}^{\mathbf{v}})] \right| / \left| \sum_{|\mathbf{v}| < |\mathbf{u}|-1} E[V_{\mathbf{v}}(\mathbf{x}^{\mathbf{v}})] \right|. \quad (3.68)$$

If this relative difference is smaller than a prescribed tolerance  $\delta_2$ , the HDMR is assumed to have converged. To provide additional accuracy for the surrogate model, the component functions identified as insignificant are also included in the final HDMR expansion that construct the surrogate model of  $V(\mathbf{x})$ .

### 3.2.2.3 Approximating HDMR Component Functions

To recursively obtain the component functions, the observable value on reference point  $\bar{\mathbf{x}}$  (for  $|\mathbf{u}|=0$ ) is computed and the observable values on lines (for  $|\mathbf{u}|=1$ ), planes (for  $|\mathbf{u}|=2$ ), and hyperplanes (for  $|\mathbf{u}| \geq 3$ ) passing through  $\bar{\mathbf{x}}$  are interpolated using the ME-PC method. To do that, the component function  $V(\mathbf{x}^v)$  are approximated using  $p$ th-order local gPC expansion as

$$V(\mathbf{x}^v) \Big|_{\mathbf{x}=\bar{\mathbf{x}} \setminus \mathbf{x}^v} = \sum_{m=0}^{N_p} v_m^v \mathbf{P}_m(\mathbf{x}^v) \Big|_{\mathbf{x}=\bar{\mathbf{x}} \setminus \mathbf{x}^v} \quad (3.69)$$

where  $v_m^v$  and  $\mathbf{P}_m(\mathbf{x}^v)$  denotes the local gPC coefficients and  $|\mathbf{v}|$ -variate local orthogonal Legendre polynomial basis functions (defined over the domain of  $V(\mathbf{x}^v) \Big|_{\mathbf{x}=\bar{\mathbf{x}} \setminus \mathbf{x}^v}$ ). The local gPC coefficients  $v_m^v$  are obtained by evaluating a  $|\mathbf{v}|$ -variate integral. During the ME-PC's construction of expansion coefficients, an adaptive refinement process is performed and the refinement parameters are also computed separately for all component functions. The final approximation of  $V(\mathbf{x})$  is to sum up the ME-PC approximations of all component functions. To this end, the ME-PC enhanced HDMR method is introduced. Further information about this method can be referred to [18, 54].

### 3.2.3 Code Validation

Next, the proposed statistical framework is used to statistically characterize EM wave propagation in a rectangular mine entry populated with PEC mine carts [Fig. 3-25(a)]. The mine entry houses four PEC mine carts which are centered at  $(cx_j, cy_j, cz_j)$ ,  $j=1, \dots, 4$ , and modeled by truncated inverted pyramids with the base and top cross-sections of  $0.5\text{m} \times 0.6\text{m}$  and  $0.8\text{m} \times 0.6\text{m}$ , respectively; the heights of the truncated inverted pyramids are  $0.6\text{m}$ . The wheels of mine carts are formed by circular plates with the radii of  $0.1\text{m}$ . The mine entry is excited by a z-directed electric dipole (with unit moment) positioned at  $(dx, dy, dz)$ . The observables are the magnitudes of the E-field's z-component,  $|E_z|$ , computed on a grid of receiver points selected in a cube with the side length of  $0.6\text{m}$  and centered at  $(0.925, 25.0, 1.12)\text{m}$ ; the spacing between receiver points along each direction is  $0.06\text{m}$  and the total number of receiver points in the cube is 1331. The error in surrogate model is computed using

$$err = \sqrt{\sum_{i=1}^{160} (|E_z(\mathbf{x}_i)| - |E_z^s(\mathbf{x}_i)|)^2 / \sum_{i=1}^{160} |E_z(\mathbf{x}_i)|^2} \quad (3.70)$$

where  $|E_z^s(\mathbf{x})|$  is the surrogate model generated using the ME-PC method with  $\varepsilon_1=10^{-1}$  and  $\tau_1=\tau_2=0.5$  and  $\mathbf{x}_i$  is the randomly chosen evaluation point. The approximation to the pdf of  $|E_z(\mathbf{x})|$  is generated by running a 1,000,000 point MC on  $|E_z^s(\mathbf{x})|$ . Two different scenarios are considered.

In the first scenario,  $dx$ ,  $dy$ , and  $dz$  are random variables uniformly distributed in  $[0.625, 1.125]\text{m}$ ,  $[0.82, 1.42]\text{m}$ , and  $[1.0, 1.6]\text{m}$ , respectively, while the centers of mine carts  $(cx_j, cy_j, cz_j)$ ,  $j=1, \dots, 4$ , are set to  $(0.65, 6+(j-1) \times 5, 0.55)\text{m}$ ,  $j=1, \dots, 4$ , ( $\mathbf{x}=[dx, dy, dz]$ ,  $N_{\text{dof}}=3$ ). The surrogate models  $|E_z^s(\mathbf{x})|$  are constructed via the ME-PC method that uses the TP integration method with five Gauss-Legendre points in each dimension to compute the coefficients of local gPC expansions

with  $p=4$ . To obtain  $|E_z^s(\mathbf{x})|$ , the proposed method required 375 deterministic simulations. The maximum of  $err$  is computed as  $6.4387 \times 10^{-3}$ . The pdf of  $|E_z(\mathbf{x})|$  (approximated by that of  $|E_z^s(\mathbf{x})|$ ) computed at receiver points reasonably match a the Nakagami distribution [Fig. 3.25(b)].

In the second scenario,  $cy_j$ ,  $j=1,\dots,4$ , are random variables uniformly distributed in  $[5.7,6.3]$  m,  $[10.7,11.3]$  m,  $[15.7,16.3]$  m, and  $[20.7,21.3]$  m, respectively, while  $cx_j$  and  $cz_j$  are set to 0.65 m and 0.55 m, respectively, and the electric dipole is positioned at  $(0.925,1.0,1.12)$  m ( $\mathbf{x}=[cy_1,\dots,cy_4]$ ,  $N_{\text{dof}}=4$ ). The surrogate models  $|E_z^s(\mathbf{x})|$  are constructed via the ME-PC method that employs the Gauss-Legendre quadrature based SG integration method (with  $l=2$ ) (for the definition of  $l$  see the appendix of [10]) to compute the coefficients of local gPC expansions with  $p=2$ . The proposed method required 969 deterministic simulations to obtain  $|E_z^s(\mathbf{x})|$ . The maximum of  $err$  is found to be  $5.0691 \times 10^{-2}$ . The pdf of  $|E_z(\mathbf{x})|$  (approximated by that of  $|E_z^s(\mathbf{x})|$ ) computed at receiver points reasonably match the Weibull distribution [Fig. 3-25(c)].

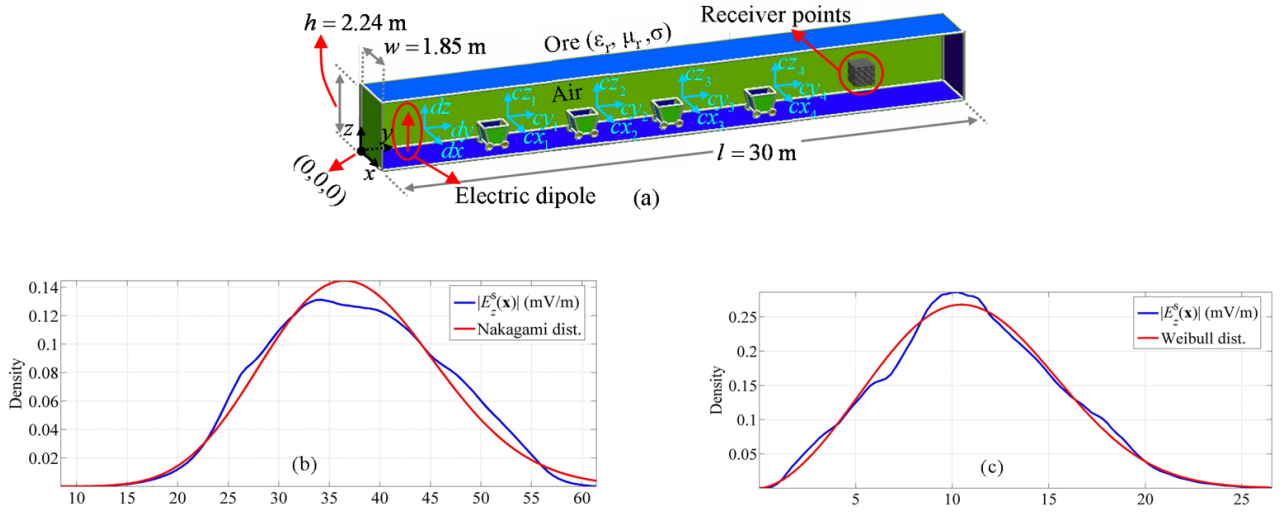
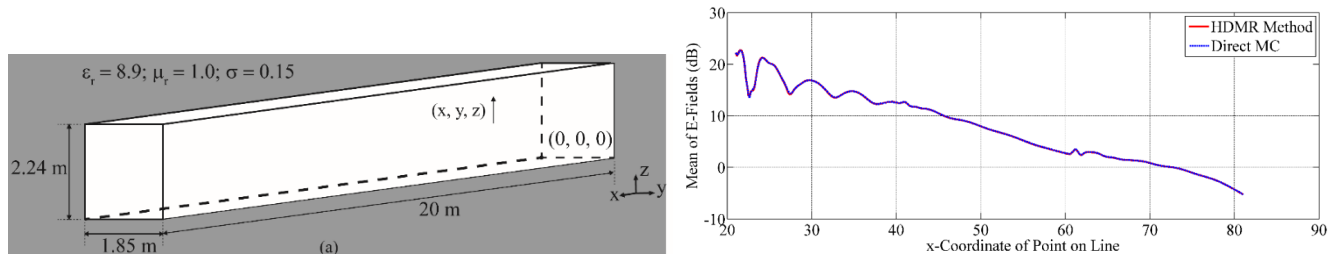


Fig. 3-25: (a) The geometry of 30m long rectangular mine entry populated with mine carts (the lateral wall is removed for illustration). (b) The pdf of  $|E_z^s(\mathbf{x})|$  computed at receiver points and its best fitting distribution (scenario I). (c) The pdf of  $|E_z^s(\mathbf{x})|$  computed at receiver points and its best fitting distribution (scenario II).

Finally, the HDMR is used to demonstrate the accuracy and efficiency of the HDMR method when applied to the statistical characterization of EM observables.



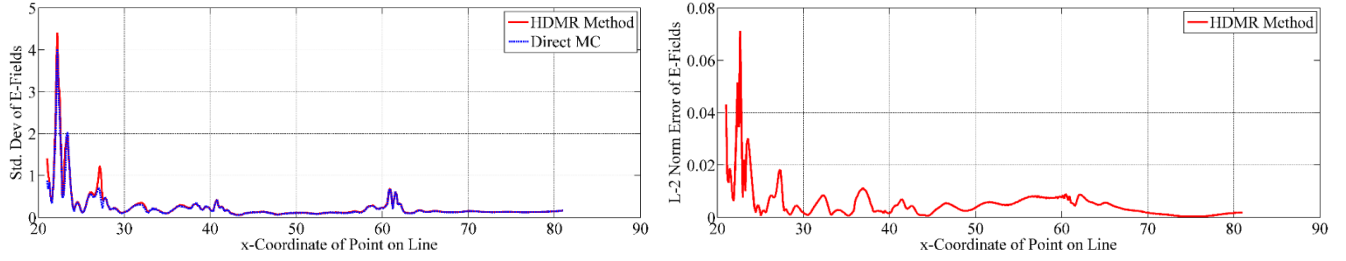


Fig. 3-26: (a) Geometry of a 100-meter rectangular entry. (b) Mean and (c) standard deviation of the electric fields computed at receiving points. (d) L-2 norm error between HDMR method and direct MC method.

Specifically, wave propagation inside a 100-meter rectangular entry is analyzed. The height, width, and length of the entry are 2.24 meters, 1.85 meters, and 20 meters, respectively. A 455 MHz dipole antenna that generates the illuminating fields is vertically oriented and located at  $(x, y, z)$  m. Variables  $(x, y, z)$  are uniformly distributed between  $[20.0, 20.5]$ ,  $[0.8, 1.05]$ , and  $[1.0, 1.24]$ , respectively. Two PEC carts are placed inside the entry and are modeled by truncated inverted pyramids centered at  $(x_1^{pec}, 0.925, 0.4)$  and  $(x_2^{pec}, 0.925, 0.4)$ . Variables  $x_1^{pec}$  and  $x_2^{pec}$  are uniformly distributed between  $[40.0, 40.5]$  and  $[60.0, 60.5]$ . A fixed 5-point HDMR is used to extract the statistics of this problem. Geometry and statistics are shown in Fig. 3-7 (a)-(d). Electric fields are computed at receiver locations along lines from  $(21, 0.925, 1.12)$  m to  $(81, 0.925, 1.12)$  m inside each entry. It can be shown that the field distribution and its statistics are affected by the presence of the mine carts. That said, the statistics obtained by HDMR and direct MC method are in good agreement. In this example, the total number of observable evaluations is 175 and is far less than the number of simulations needed by direct MC methods.

### 3.2.4 Concluding Remarks / Lessons Learned

We developed and implemented several UQ algorithms to estimate statistics/PDFs of signal strength in mine environments given uncertainty in the mine layout (geometry, material makeup) and operational state (presence and location of mining equipment).

Given a parametric description of the uncertain quantities (in practice, bounds on values these quantities can attain), the algorithms repeatedly execute the EM simulators in Section 3.1 to estimate the statistics of quantities of interest, typically received field strengths or observed power densities. The PDFs generated not only reveal the most likely signal strength observed, but also the size of likely excursions of the signal from its expected value. For example, referring to Fig. 3-25(a), while the expected value of the observed signal strength is around 35 mV/m, variations between 20 and 55 mV/m are not unlikely. Likewise, referring to Figs. 3.26(b) and (c), the expected signal strength along the mine entry is seen to experience a drop by 20 dB along the length of the entry while the standard deviation of the electric field amplitude at the beginning of the entry is higher than at the end. System designers can use this information to estimate the probability of fading and the need to add repeaters to the channel.

More examples of the application of this UQ framework are presented in Section 4.

### 3.3 Wireless System Design and Reconfiguration

#### 3.3.1 Introduction

The ability to efficiently analyze propagation of wireless signals in realistic mining environments (Section 3.1) coupled with the capacity to estimate their potential variations due to uncertainty in the mine's layout or operational state (Section 3.2) opens up possibilities for automating the design and (re-)configuration of such systems. The design of wireless systems aims to maximize coverage with as few transmitters/repeaters as possible, while their re-configuration seeks to move transmitters/repeaters to re-establish coverage following an even leading to obstruction of the channel.

The design and reconfiguration of wireless networks is best posed as an optimization problem.

Here, we incorporate the so-called DIRECT (Dividing RECTangles) global optimization algorithm [25-27] into the DD-based SIE simulator reported in Section 3.1. Any optimization method, including the DIRECT scheme, requires the repetitive execution of the EM simulator for different candidate realizations of the network. The DD simulator in Section 3.1 only requires re-solves the inter-domain system during each execution, and hence is far more efficient when used in a closed loop optimization environment that simulators that do not leverage domain decomposition.

The DIRECT algorithm was first purposed by Jones et al. in 1993 [27] as an effective approach to solve global optimization problems with simple constraints. The algorithm constitutes a Lipschitzian optimization method but does not require knowledge of the Lipschitz constant. In a nutshell, the algorithm performs a series of moves through the search space, say the positions of transmitters and receivers, thereby exploring the behavior of the objective function, say a measure of signal quality or coverage. The DIRECT scheme is unique in that it very carefully picks the realizations of the system to be evaluated by the DD scheme, thereby minimizing the computational cost and maximizing the speed of the optimization.

The objective functions used in this study are adopted from the work on wireless network optimization by Sherali et al. [58] and consist of a minisum and a minimax objective, comprising the average and maximum of the weighted path loss measured at receivers (typically miners, or access points that allow the wireless network to connect to a wired network). A penalty term applies to the objective function if the maximum tolerated path loss is violated at certain receivers. A convex combination of the two objective functions is used if an overall measure of performance is needed.

The optimization framework is designed to improve (ideally, maximize) the desired properties of a wireless network in a mine environment by adjusting a set of parameters that influence its performance. In practice, signal coverage often is the most important characteristic of a wireless network in mine environments, but other properties, such as the cost of equipment and maintenance, also may be considered [59, 60]. Parameters that one can readily adjust in a network optimization problem typically include the positions of transmitters and receivers and the topology of the network [61, 62]. To demonstrate the efficiency and applicability of the proposed optimization framework, the problem considered here involves optimization of the positions of transmitters, given a set of fixed receivers, to attain the desired network coverage.

The proposed framework may also be applicable to other wireless network optimization problems.

While much of the optimization literature is devoted to the quality of the optima different schemes produce, it is important to note that in the context of wireless system design it oftentimes is not necessary to seek positions of transmitters leading to a global optimum of the objective function [59]. One reason is that there is no point in distinguishing very small differences of the desired coverage property, since the EM simulator is only an approximate tool. Additionally, there oftentimes are multiple sets of transmitter positions that produce almost identical coverage inside a mine environment; this oftentimes is the case when all receivers have Line of Sight (LoS) connections to the transmitters. Hence, the aim of the optimization schemes described here is to find a “good solution” as opposed to the “globally optimal one” using as little computational resources as possible.

In this section and Section 4, the proposed optimization framework is applied to the optimum placement of nodes in a partial mesh wireless networks operated at 455 MHz and 915 MHz inside mine entries and galleries.

### 3.3.2 Optimization Algorithm

The DIRECT optimization algorithm [27] is a modification of standard Lipschitzian optimization approaches and is widely-used in engineering applications (see [26] and references therein). It has two major advantages. First, instead of sampling the vertices of a search space like standard Lipschitzian methods, it samples at midpoints, thereby allowing the algorithm to be applied in high dimensions. Second, it does not require knowledge of the Lipschitz constant and the objective function to be Lipschitz continuous. It uses the function value at the center of a region in the search space and the region's size to determine if it should be divided into sub-regions during an iteration.

#### A) Initialization

Without loss of generality, let the domain describing the parameters subject to optimization be a unit hyper-cube, i.e.

$$D = \{x \in \mathbb{R}^n : 0 \leq x_k \leq 1, k = 1, \dots, n\}. \quad (3.71)$$

The domain of optimization for any problem can be easily transformed into a unit hyper-cube. During the initialization phase of the algorithm, it first evaluates the objective function at the center of the hyper-cube and points  $\mathbf{c}_1 \pm (1/3)\mathbf{e}_k$ ,  $k = 1, \dots, n$ , and computes

$$v_k = \min(f(\mathbf{c}_1 + (1/3)\mathbf{e}_k), f(\mathbf{c}_1 - (1/3)\mathbf{e}_k)), \quad k = 1, \dots, n \quad (3.72)$$

where  $\mathbf{c}_1$  is the center of the space and  $\mathbf{e}_k$  is the unit vector in the  $k$ th dimension. Next, the algorithm divides the hyper-cube. The division begins by dividing the whole region into thirds along the dimension with smallest  $v_k$ , and continues by dividing the central sub-region (the one resulted from previous division and containing  $\mathbf{c}_1$ ), along the dimension with the next smallest  $v_k$ , until all dimensions are divided. Fig. 3-27 illustrates this procedure for a two-dimensional objective function.



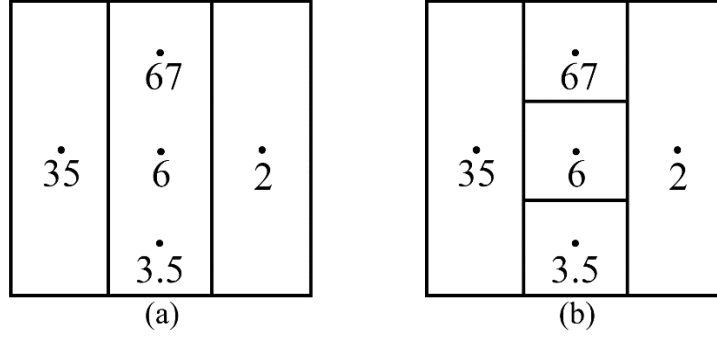


Fig. 3-27: (a) Divide the searching domain into three sub-regions along the dimension with smallest  $v_k$ . (b) Divide the central sub-region along the dimension with second smallest  $v_k$  and finish initialization. Sampling points are represented by black dots and the value of objective function at sampling points are shown below the dots.

### B) Iteration

Let  $\varepsilon > 0$  be a positive constant and  $f_{\min}$  be the smallest value of the objective function identified. Denote  $I$  denote the set of indices of all currently active regions. A region  $j$  is defined to be potentially optimal if there exists an  $\tilde{L} > 0$  such that [27]

$$f(\mathbf{c}_j) - \tilde{L}d_j \leq f(\mathbf{c}_i) - \tilde{L}d_i, \forall i \in I, \text{ and} \quad (3.73)$$

$$f(\mathbf{c}_j) - \tilde{L}d_j \leq f_{\min} - \varepsilon |f_{\min}|, \quad (3.74)$$

where  $\mathbf{c}_i$  and  $d_i$  are the center and a measure of size of region  $i$ , respectively. Various definitions of  $d_i$  are used in the literature [25, 63]. Here,  $d_i$  is defined as the distance from  $\mathbf{c}_i$  to the vertices of region  $i$ . Note that the same definition applies to those with subscript  $j$ . The graphical interpretation of the first condition is shown in Fig. 3-28(a). When (3.73) is satisfied, a line with slope  $\tilde{L}$  passing  $f(\mathbf{c}_j)$  must intercept the vertical axis at  $f(\mathbf{c}_j) - \tilde{L}d_j$ , which is lower than all the other vertical intercepts of the line with the same slope but passing other points. Hence, the first condition requires the potentially optimal regions to be on the bottom of the convex hull of the points [Fig. 3-28(b)]. The second condition requires that  $f(\mathbf{c}_j) - \tilde{L}d_j$  exceeds the current best solution by a nontrivial value, which prevents the algorithm from pursuing extremely small improvements. As demonstrated in [27], the choice of  $\varepsilon$  between  $1 \times 10^{-2}$  and  $1 \times 10^{-7}$  has only a negligible effect on the performance.

The definition of potentially optimal regions does not provide a practical way to identify if a region  $j$  is potentially optimal. Hence, an interpretation of the definition is given to help the identification [26]. Let  $I_1 = \{i \in I : d_i < d_j\}$ ,  $I_2 = \{i \in I : d_i > d_j\}$ , and  $I_3 = \{i \in I : d_i = d_j\}$ . Region  $j$  is potentially optimal if

$$f(\mathbf{c}_j) \leq f(\mathbf{c}_i), \forall i \in I_3, \quad (3.75)$$

$$\max_{i \in I_1} \frac{f(\mathbf{c}_j) - f(\mathbf{c}_i)}{d_j - d_i} \leq \min_{i \in I_2} \frac{f(\mathbf{c}_i) - f(\mathbf{c}_j)}{d_i - d_j}, \quad (3.76)$$

and

$$\varepsilon \leq \frac{f_{\min} - f(\mathbf{c}_j)}{|f_{\min}|} + \frac{d_j}{|f_{\min}|} \min_{i \in I_2} \frac{f(\mathbf{c}_i) - f(\mathbf{c}_j)}{d_i - d_j}, \quad f_{\min} \neq 0, \quad (3.77)$$

or

$$f(\mathbf{c}_j) \leq d_j \min_{i \in I_2} \frac{f(\mathbf{c}_i) - f(\mathbf{c}_j)}{d_i - d_j}, \quad f_{\min} = 0. \quad (3.78)$$

The proof of this interpretation is provided in [26]. Eqs (3.75) - (3.78) can be easily implemented into computer codes.

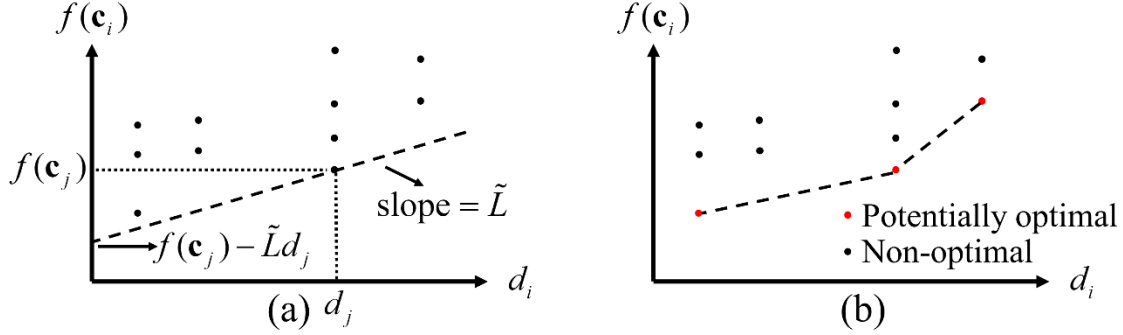


Fig. 3-28: (a) First condition of potentially optimal regions. (b) Set of potentially optimal regions. Dot represents the value of objective function evaluated at the center of each region.

After potentially optimal regions are identified, the algorithm proceeds to divide these regions along their longest dimension(s). If a region is a hyper-cube (i.e. all dimensions have the same length), the division is done along all dimensions via the procedures in the initialization phase. The dividing strategy contains the following three steps:

Step 1: Identify the set  $U_i$  that contains all dimensions of the maximum side length for the potentially optimal region  $i$ .

Step 2: Evaluate the objective function at points  $\mathbf{c}_i \pm \delta_i \mathbf{e}_k$  and compute  $v_k = \min \{f(\mathbf{c}_i + \delta_i \mathbf{e}_k), f(\mathbf{c}_i - \delta_i \mathbf{e}_k)\}$  for all  $k \in U_i$ . Here,  $\mathbf{c}_i$  and  $\delta_i$  are the center and one-third of the maximum side length of the region  $i$ , respectively.  $\mathbf{e}_k$  is the unit vector in the  $k$ th dimension.

Step 3: Divide region  $i$  into thirds along the dimension with smallest value of  $v_k$ , and continue the division for the central sub-region (the one resulted from the previous division and containing  $\mathbf{c}_i$ ) in the dimension with next smallest  $v_k$  until it is repeated for all the dimensions in  $U_i$ .

As demonstrated in [27], this strategy ensures that the regions to be divided will shrink on all dimensions. Once the division of all potentially optimal regions are done, an iteration of the algorithm is completed. Fig. 3-29(a) illustrates first two iterations for the example two-dimension objective function. Note that the initialization is done in the example given in Fig. 3-27.

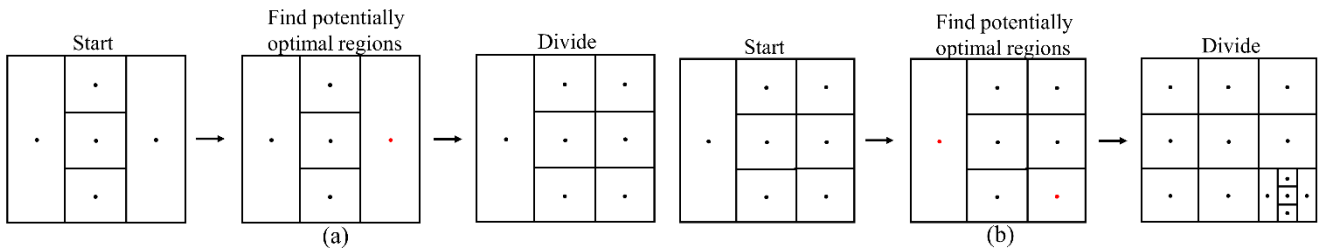


Fig. 3-29: First two iterations of the DIRECT algorithm for the example objective function: (a) iteration 1 and (b) iteration 2. Red dots represent the center of potentially optimal regions

### C) Termination Criterion, Algorithm, and Discussion

When the global minimum of the objective function is unknown, frequent choices of the termination criterion include the number of iteration or objective function evaluation, size of the smallest regions, and the convergence rate of objective function [64]. Since the aim of the optimization is to find an approximation that lies within a certain range of the optimal positions, the size of smallest regions is chosen as the termination criterion, i.e., the algorithm stops when the size of smallest region reaches a prescribed threshold. To this end, the DIRECT algorithm is given below.

---

#### DIRECT Algorithm

---

- 1: Normalize the problem domain to a unit hyper-cube.
  - 2: Set  $i = 0$ , compute  $f(\mathbf{c}_1)$ , set  $f_{\min} = f(\mathbf{c}_1)$ , and divide the hyper-cube
  - 3: **while** size of smallest regions > threshold, **do**
  - 4: Identify all potentially optimal regions
  - 5: Evaluate objective function at points required to divide the potentially optimal regions
  - 6: Divide all potentially optimal regions, update  $f_{\min}$ ,  $i = i + 1$ .
  - 7: **end while**
- 

Table 3-2 DIRECT Algorithm

The DIRECT algorithm is a direct search method. It does not require any knowledge of objective function gradient. Instead, it evaluates function at sampling points over the searching domain and uses the information obtained from the sampling to decide the searching direction. Hence, it is well-used in engineering applications, where the value of objective function is obtained from numerical simulation and the gradient is unavailable or unreliable. On the other hand, the DIRECT algorithm will converge to global optimum, while many other direct search methods, such as Nelder-Mead algorithm [23] and Hooke-Jeeves pattern search method [24], are only guaranteed to converge to local optimum. Hence, it can avoid local traps and provide better performance when there are many local optimums in the problem.

The main weakness of the DIRECT algorithm is the slow convergence rate [65]. It can quickly find region(s) containing the optima but will slowly converge to it. That said, this burden is alleviated in the application of wireless network optimizations. As discussed in the introduction part, the exact optimal positions of transmitters are not necessarily needed, but good approximations close to the optimal positions are enough. Since the DIRECT algorithm can quickly locate regions containing the optimum, the points it samples will likely to be close to the optimum and a good set of approximations can be quickly obtained.

### 3.3.3 Objective Function

The quality of an optimization depends on the measure of the desired properties, which is represented by an objective function. The objective functions considered here facilitate the location of transmitters that yield optimal average coverage, optimal worst coverage, or a convex combination of them. Based on this idea, the objective functions is defined as [58]

$$f_1 = \frac{1}{m} \sum_{i=1}^m w_i [p_i + u_i \max\{0, p_i - s_i\}], \quad (3.79)$$

$$f_2 = \max_{i=1,\dots,m} \{w_i [p_i + u_i \max\{0, p_i - s_i\}]\}, \quad (3.80)$$

where  $f_1$  is a minisum function and  $f_2$  is a minimax function.  $m$  and  $n$  are the total number of receivers/access points and transmitters, respectively. The path loss function is  $p_i = \min_{j=1,\dots,n} \{g_{i,j}\}$ , where  $g_{i,j}$  is the path loss at the  $i$ th receiver due to the  $j$ th node;  $w_i$ ,  $u_i$  and  $s_i$  are the weight, penalty factor, and maximum tolerated path loss prescribed for the  $i$ th receiver, respectively. The minisum function is the weighted average of all path losses at the different receiver positions, and a penalty term is added if a maximum path loss threshold is violated. The minimax function is the weighted path loss experienced by the worst served receiver. The choice of  $f_1$  or  $f_2$  depends on the specific optimization scenario and requirements. When an overall measure of coverage quality is required, a convex combination of  $f_1$  and  $f_2$  is used, which is defined as

$$f_c = \varphi f_1 + (1 - \varphi) f_2 \quad (3.81)$$

where  $\varphi$  is the combination parameter. The convex combination parameter can be adjusted based on the path loss profiles obtained during optimization.

### 3.3.4 Code Validation

This section validates the proposed optimization framework via its application to transmitter placement problems in electrically large mine galleries. In all examples below, mine entries are filled with air and surrounded by rock with relative permittivity  $\varepsilon_r = 8.9$ , relative permeability  $\mu_r = 1$ , and conductivity  $\sigma = 0.15$  S/m; here  $\varepsilon_r$ ,  $\mu_r$ ,  $\sigma$  are related to  $\varepsilon_1$  and  $\mu_1$  via  $\mu_1 = \mu_r \mu_0$  and  $\varepsilon_1 = \varepsilon_0 \varepsilon_r - j\sigma/\omega$ . The smallest region size threshold for terminating the optimization algorithm is set to 0.05 m. The combination parameter  $\varphi$  for  $f_c$  is 0.5 for all examples. The transmitters are modeled as electric dipoles with unit moment. The power values obtained by the proposed simulator and other methods are normalized to their maxima. The optimization algorithm was implemented in MATLAB [66] and incorporated with the DD-based SIE simulator, which was executed in parallel on a cluster of dual hexacore X5650 Intel processors.

The proposed framework is used to optimize 915 MHz wireless networks inside a mine gallery formed by two 71.05 m - long entries that extend along  $x$  and connect to each other via three 11 m - long branches extending along  $y$  [Fig. 3-30(a)]. It is used to optimize a three-transmitter network and reconfigure the optimized network after a catastrophic event. Six access points are placed inside the mine gallery [Fig. 3-30(a)]. Three of them are placed 2 meters before the end of entry. The remaining three access points are placed at the center of each branch that connects two entries. The average CPU time for one distinct simulation for this mine gallery is approximately 3 hours.

The positions of transmitter 1, 2, and 3 are  $(x_1, 0.925, 1.12)$ ,  $(x_2, 13.775, 1.12)$ , and  $(x_3, 0.925, 1.12)$ , respectively, where  $x_1 \in [20, 50]$ ,  $x_2 \in [30, 80]$ , and  $x_3 \in [51, 71]$  are to be determined with respect to the overall coverage measured by  $f_c$  [Fig. 3-30(a)]. The results are  $x_1 = 41.33$ ,  $x_2 = 54.20$ , and  $x_3 = 67.83$ . Power densities are computed on the  $xy$ -plane at  $z = 1.12$  m [Fig. 3-30(b)]. It can

be visually observed that after optimization all access points have LOS connection with transmitters.

Next, the proposed framework is used to reconfigure the optimized three-transmitter network following a catastrophic event. A cave-in appeared in branch 2 and blocks the signal [Fig. 3-30 (c)]. Hence, the access point in branch 2 lost its LoS connection with transmitters. To perform the reconfiguration, the positions of transmitter 1, 2, and 3 are reset to  $(x_1, 0.925, 1.12)$ ,  $(x_2, 13.775, 1.12)$ , and  $(x_3, 0.925, 1.12)$ , respectively, where  $x_1 \in [20, 50]$ ,  $x_2 \in [30, 80]$ , and  $x_3 \in [51, 71]$  are variables to be reconfigured [Fig. 3-30(c)]. The reconfiguration process took 151 objective function evaluations to converge. The reconfigured positions of transmitter 1, 2, and 3 are (41.42, 0.925, 1.12), (66.91, 13.775, 1.12), and (54.64, 0.925, 1.12), respectively. The power values of the reconfigured network are computed on the  $xy$ -plane at  $z = 1.12$  m [Fig. 3-30(d)]. Apparently, the LOS connection between access point in branch 2 and transmitters is restored.

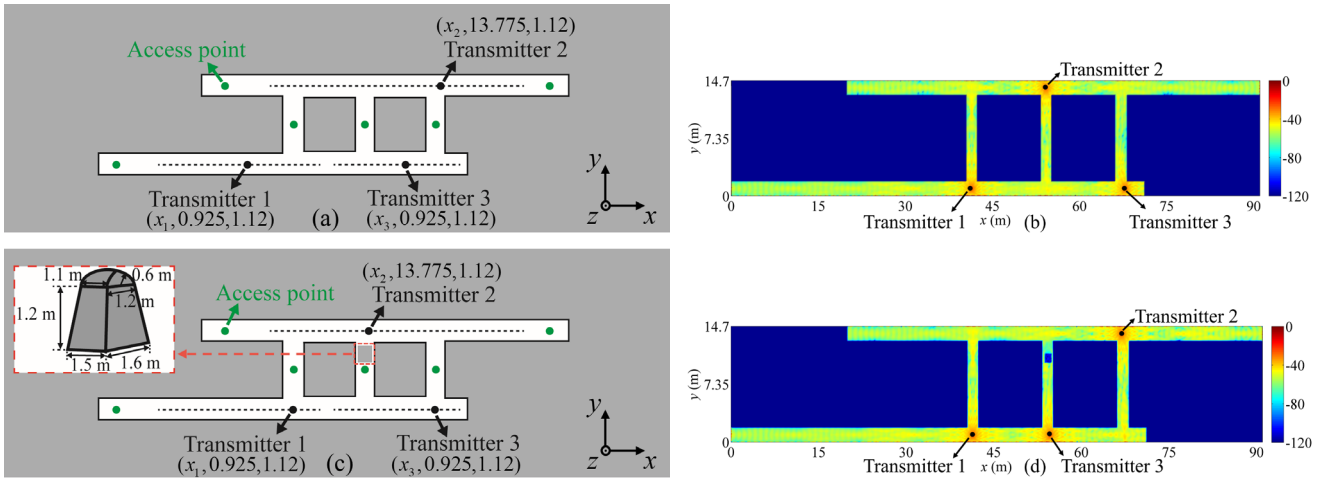


Fig. 3-30: (a) Three-transmitter network and access points on plane  $z = 1.12$  m. (b) Power densities computed on plane  $z = 1.12$  m for optimization of overall coverage (scale: dBm). (c) Optimized network and the cave-in. (d) Power values computed on plane  $z = 1.12$  m after reconfiguration (scale: dBm)

### 3.3.5 Concluding Remarks / Lessons Learned

We developed and implemented a closed-loop scheme for designing and reconfiguring wireless mine communication systems. The scheme heavily leverages the full wave EM simulators of Section 3.1 to determine positions of transmitters/repeaters that maximize power densities at user-defined receiver locations (the latter oftentimes cover large portions of entries and galleries, corresponding to possible locations of miners).

The algorithm uses a search scheme called DIRECT, which strikes a nice balance between the number of objective function evaluations (i.e. calls to full wave EM simulators) and the quality of the optimum identified. Without fail, the scheme identifies network layouts that establish LoS connections between transmitters and receivers when possible; when no transmitter constellation that achieves LoS connection exists, the scheme is capable of identifying non-intuitive designs that nonetheless maximize signal coverage (see Section 4).

Even though the DIRECT scheme minimizes the number of executions of the EM simulators in Section 3.1, the computational cost of these optimization schemes remains very high, often requiring hundreds of hours of CPU time. To reduce the cost, the DIRECT scheme should perform

approximate function evaluations early on in the optimization process, for example using a ray tracer, and only invoke the full wave solvers for its final few iterations. Such a scheme remains to be implemented.

More examples of the application of the DIRECT scheme to network optimization are presented in Section 4.

## 4 Research Findings and Accomplishments

This section describes research performed towards Objective (iv) and reports results obtained by applying the proposed EM simulators, UQ, and optimization framework to a variety of mine communication systems.

### 4.1 Leaky Feeders

#### 4.1.1 Introduction

Leaky feeders are often used in mines with complex tunnel networks [Fig. 4-1]. Leaky feeders have dual functionality; they not only transmit a radio signal along the cable but also radiate the signal through carefully designed slots. Leaky feeders have good noise characteristics and enough bandwidth to simultaneously support multiple signals (e.g. voice, text, and video). The leaky feeder system also is capable of powering embedded cable amplifiers and active wireless nodes.

Leaky feeder systems have been studied extensively in the archival literature. Fan et al. [67] studied the radiation characteristics of a leaky coaxial cable and compared them with those of a helical antenna. Feng et al. [68] theoretically analyzed the radiating modes of leaky coaxial cables. However, these techniques rely on simplified assumptions and/or approximations that limit their real-world application. Full-wave analysis methods do not suffer from these limitations. In [69], Wang et al. used the finite-difference time-domain (FDTD) method to calculate the electric field distribution in a slot cut in the outer conductor of a coaxial leaky feeder cable. Unfortunately, the FDTD is computationally expensive, especially when applied to the analysis of cables spanning long mine entries; moreover, the technique cannot be directly applied to the computation of fields inside the mine entry as it assumes a free-space external environment.

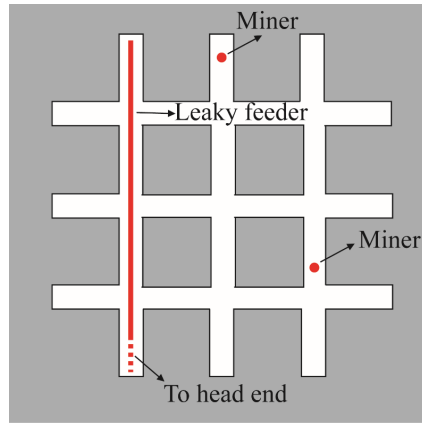


Fig. 4-1 Example of leaky feeder system. The two miners can communicate with each other if they are within the range of the leaky feeder cable.

In this section, the proposed EM-UQ framework is used to analyze leaky feeder systems that reside inside mine entries and galleries. In all examples, the cable is operating in radiating mode and the signal decay in the cable is modeled by the diffuse model detailed in [70]. In this model, a cable element of specified length (in our analysis 1 m) is represented by a point source radiating the per unit length power

$$P = (\pi D/8)(4\pi/\lambda)^2 10^{-L/10} \exp(-2\alpha x) P_{feed} \quad (4.1)$$

in the appropriate polarization. Here,  $D$  is the reference distance between the axis of the cable and a half-wave dipole residing parallel to its axis;  $\alpha$  is the attenuation constant in  $Np/m$ ;  $L$  is the standard coupling loss of a leaky coax;  $D$  is usually 20 ft.; values for  $\alpha$  and  $L$  can be easily found in manuals for commercially available leaky cable systems - here,  $\alpha$  and  $L$  are chosen as 0.0152 and 65.0, respectively; and  $x$  is the distance between the radiating and feed points.

#### 4.1.2 250-Meter Cable

In the first example, a leaky feeder that resides in a 250-meter long tunnel of width 1.85 m and height 2.24 m is analyzed. The cable extends from (5, 0.925, 2.10) m to (245, 0.925, 2.10) m and is fed at one end. The frequency is 455 MHz and cable slots are spaced 1 meter apart [Fig. 4-2]. The medium around the tunnel is lossy (conductivity is 0.15 S/m) and its relative permittivity and permeability are 8.9 and 1.0, respectively. The electric current and field distribution on the plane  $y=0.925$  are shown in Figs. 4-3 and 4-4, respectively. The electric field and the current density decay by over 60 dB along the 250-meter tunnel.

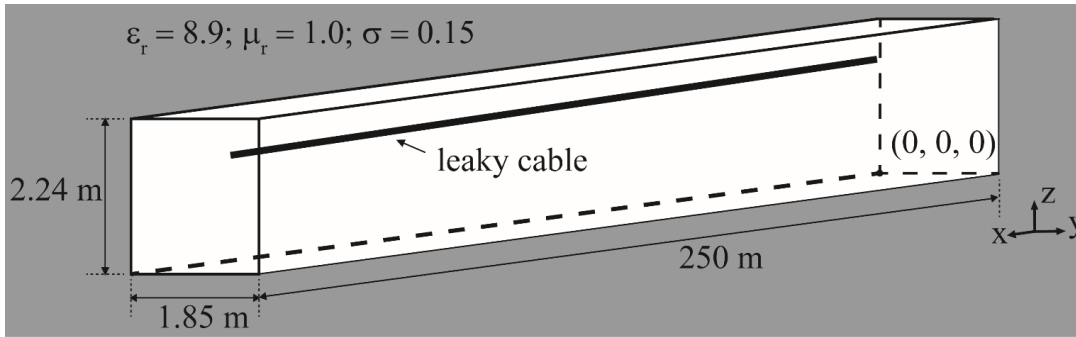


Fig. 4-2: Geometry of a leaky feeder system in a 250-meter tunnel.

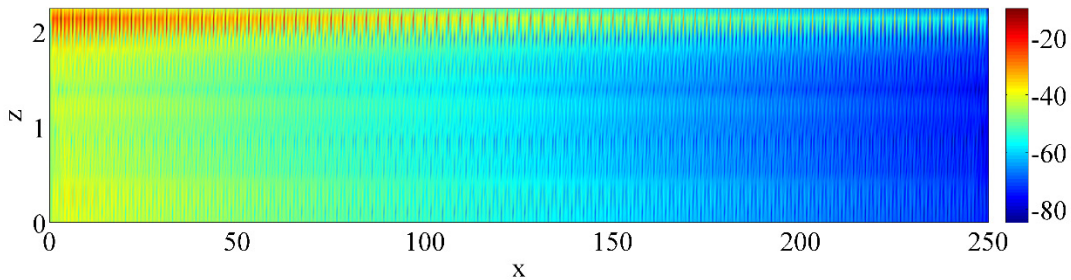


Fig. 4-3: Field distribution on the  $y=0.925$  plane.



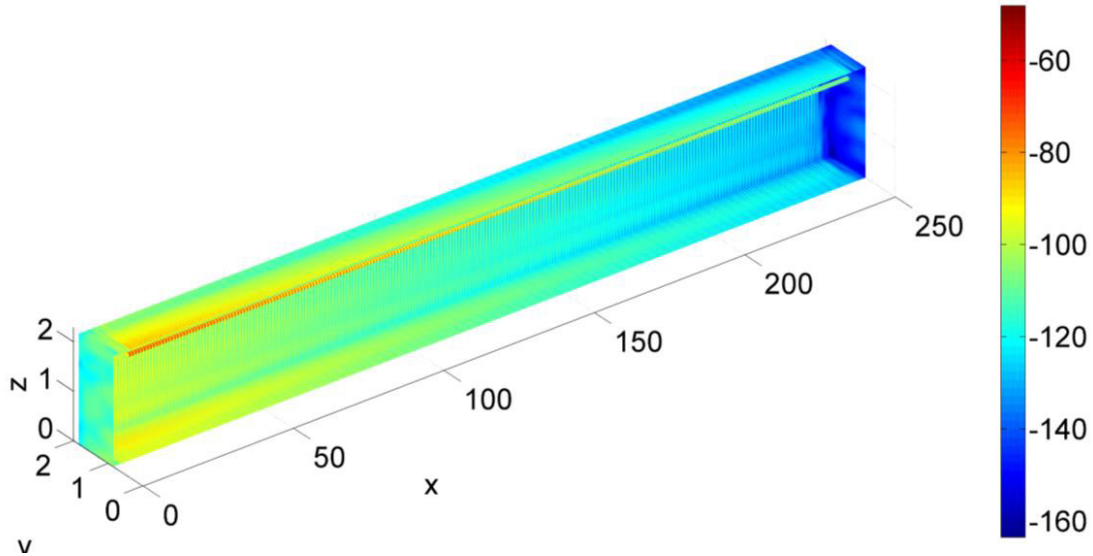


Fig. 4-4: Current distribution on the tunnel walls and leaky cables. Wall on right side has been removed for illustration.

#### 4.1.3 1400-Meter Cable with Amplifiers

In the second example, a 1400-meter leaky feeder that resides in a straight tunnel with two amplifiers is analyzed. The amplifiers extend the signal coverage well beyond what is possible using the system in the above example. The width and height of the tunnel again are 1.85m and 2.24m. The cable extends from (5, 0.925, 2.10) m to (245, 0.925, 2.10) m. The frequency is 455 MHz and radiating slots are spaced 1 meter apart. The amplifiers are separated by 400 m. The geometry, electric current distribution, and field distribution on the plane  $y=0.925$  are shown in Figs. 4-5, 4-6, and 4-7, respectively. Inclusion of the amplifiers boosts the field strength in the tunnel when its level drops too much.

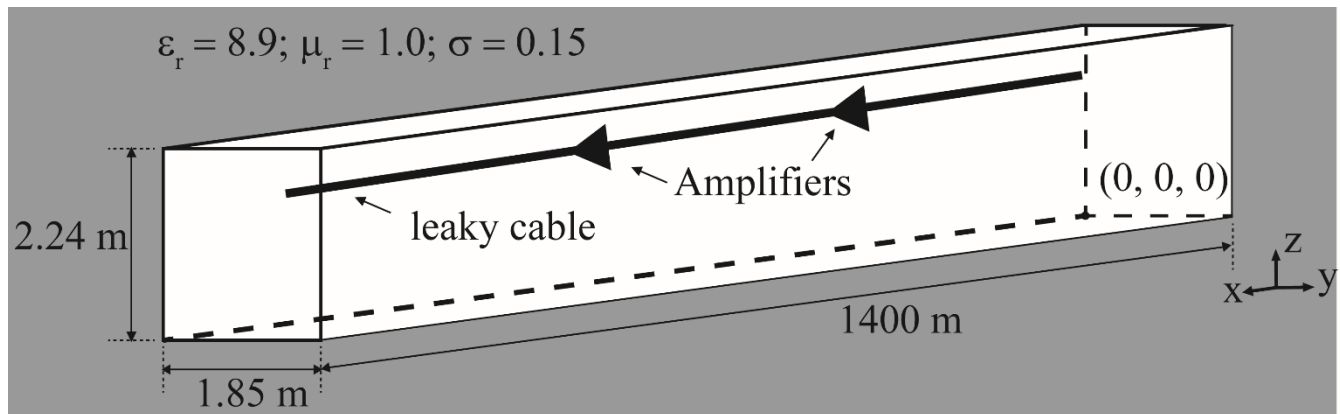


Fig. 4-5: Geometry of a leaky feeder system in 1400-meter tunnel. Two amplifiers 400m apart are installed on the cable.

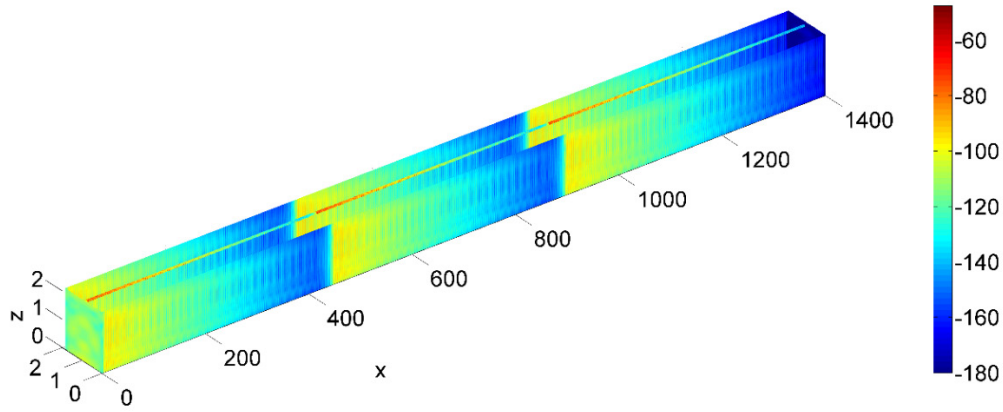


Fig. 4-6: Current Distribution on the tunnel walls and leaky cables. Wall on the top has been removed for illustration (scale: dB).

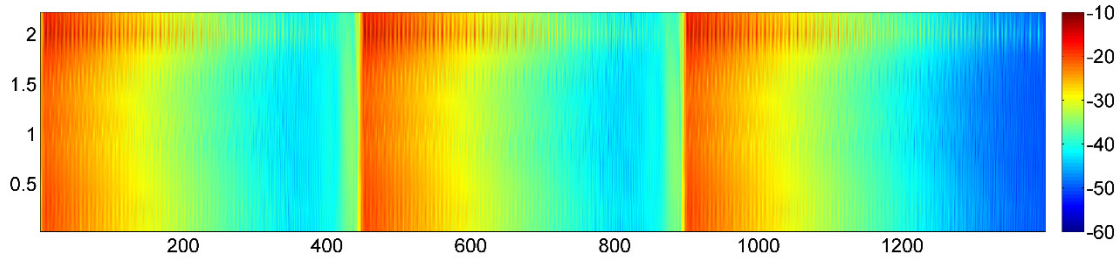


Fig. 4-7: Field distribution along  $y=0.925$  plane (scale: dBm).

#### 4.1.4 Uncertainty quantification

In realistic environments, many uncertainties may affect the performance of a leaky feeder system.

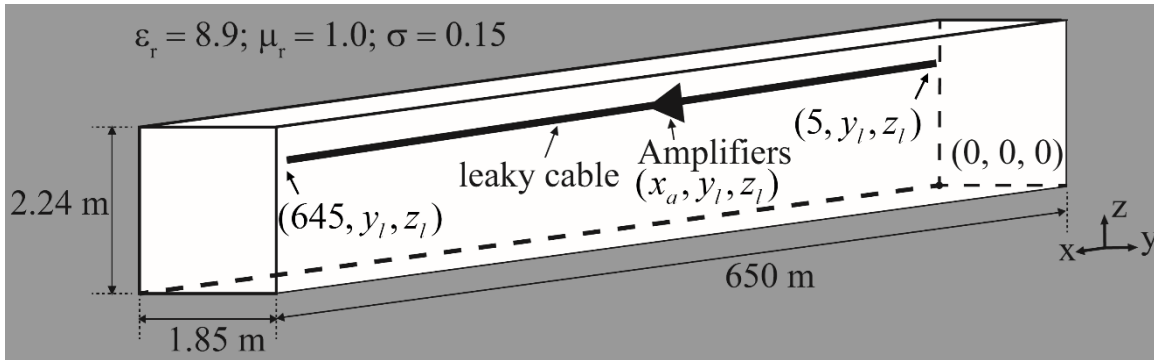


Fig. 4.8 Geometry of a straight entry and a leaky cable with amplifier.

Here, the effect of uncertainties in the cable's location and the position of an amplifier located roughly midway the cable on the power received at two locations is quantified. The leaky feeder is installed in a 650-meter long entry. The width and height of the entry are 1.85 m and 2.24 m, respectively. The relative permittivity  $\epsilon_r$ , permeability  $\mu_r$  and conductivity  $\sigma$  of the surrounding medium are 8.9, 1.0, and 0.15, respectively. The cable is 640 m long and extends from  $(5, y_l, z_l)$  m to  $(645, y_l, z_l)$  m, where  $y_l$  and  $z_l$  are random variables uniformly distributed in the ranges

[0.6, 1.25] m and [1.90, 2.10] m. The amplifier is installed near the center of the cable and positioned at  $(x_a, y_l, z_l)$  m, where  $x_a$  is a random variable uniformly distributed in the range [290, 310] m. Two receivers are positioned inside the entry. Receiver 1 resides at (300, 0.925, 1.12) (near the center of the entry) and receiver 2 is at (640, 0.925, 1.12), (near the end of the entry). The observables are the received power strength at both receivers. Table 4-1 presents the observables' averages and standard deviations computed by the proposed EM-UQ framework.

It is observed that the power strength at receiver 1 has a much larger standard deviation than that at receiver 2. This is expected as the amplifier is placed near receiver 1, where field strengths are larger and more variable due to uncertainty of the relative position of the amplifier w.r.t. the observer. The PDFs of power densities at the two receivers are obtained by performing 5000-point MC simulations on an HDMR constructed surrogate model [Fig. 4.9(a)-(b)]. These PDFs confirm the data in the table. The means and standard deviations reported in Table 4-1 (represented by the peaks and widths of the curves in Fig. 4.9) provide system designers with knowledge of expected and worst case signal strengths at receivers.

Statistics	Observables	Proposed Framework
Mean (dBm)	Power Strength at Receiver 1	-6.97
	Power Strength at Receiver 2	-30.39
Standard Deviation (dBm)	Power Strength at Receiver 1	3.83
	Power Strength at Receiver 2	1.96
Number of Simulations		61

Table 4-1 Statistics and number of deterministic simulations obtained by the proposed EM-UQ framework.

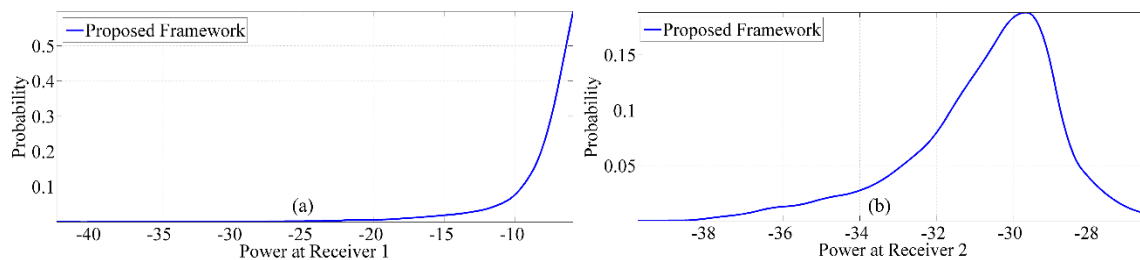


Fig. 4.9: PDF of power densities at (a) receiver 1 and (b) receiver 2 (scale: dBm).

## 4.2 Through-the-Earth System

The Mine Improvement and New Emergency Response Act of 2006 (MINER Act) requires that every underground mine in the U.S. has an emergency response plan. The plan must include a two-way wireless post-accident communication system between the underground environment and the surface to electronically track, and communicate with, miners. In an emergency, conventional communication systems may be interrupted or disabled if communication infrastructure becomes damaged; in such situations backup communication systems between rescuers at the surface and miners become particularly important. One way to establish post-

accident communication is to directly communicate from the surface to the miners using Through the Earth (TTE) systems [Fig. 4.10 (a)]. Although past research showed that TTE transmission between the surface and miners may be difficult to establish, recent technological advances offer new possibilities for TTE communication. Current TTE communications tested in mine environments use large loop antennas operating at ultra-low frequencies to send/receive signals. A major advantage of TTE systems is that they require much less underground and surface infrastructure than high frequency communication systems in post-accident situations.

In an emergency, the configuration of a TTE communication system too may become affected or damaged. For example, an earthquake or an explosion inside mine entries may change the position and orientation of communication devices, influencing the signal transmission path and the connection quality. To enhance the reliability and functionality of a TTE communication system, these uncertainties must be accurately quantified. In the example below, uncertainties in the transmitter's location and polarization are quantified via the proposed EM-UQ framework.

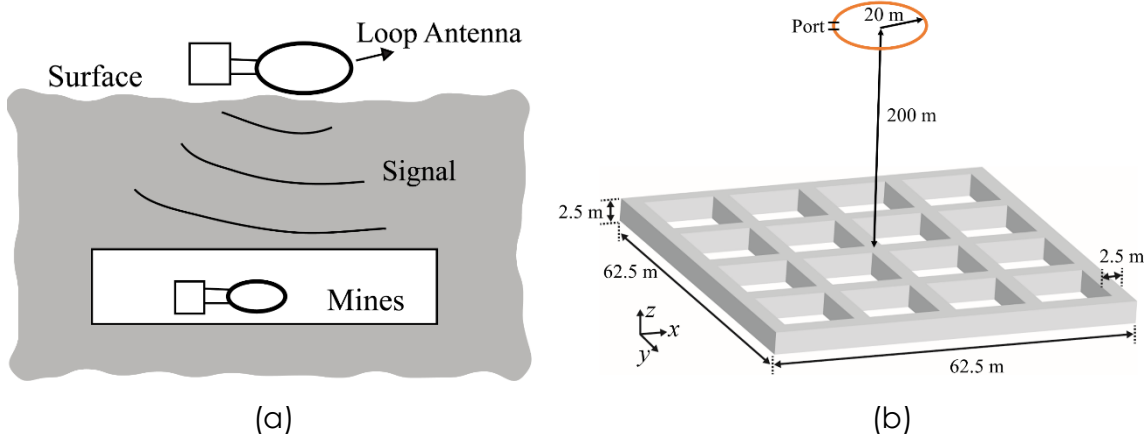


Fig. 4.10: (a) TTE communication system. (b) UQ example of the TTE system.

Specifically, we characterize a TTE system in a mine gallery located 200 m underground [Fig. 4.10(b)]. The gallery is surrounded by homogeneous lossy soil with relative permittivity 3.0, relative permeability 1.0, and conductivity 0.01. The gallery occupies a 62.5 m by 62.5 m area and the cross section of each entry is 2.5 m by 2.5 m. A magnetic dipole, which is used to model the transmitting loop antenna and which operates at 5000 Hz, is located at  $(x, y, z)$  and is "oriented" towards direction  $(\theta, \phi)$ . Variables  $x$ ,  $y$ ,  $z$ ,  $\theta$ , and  $\phi$  (physical angle w.r.t. the feed point) are assumed uncertain and vary uniformly in the intervals  $[-0.5, 0.5]$  m,  $[-0.5, 0.5]$  m,  $[-200.5, -199.5]$  m,  $[0, 10]$  degrees and  $[0, 360]$  degrees, respectively. The observables are the amplitude and phase of the current flowing through the load of the receiving loop antenna (inside the mine). Table 4-2 presents these observables' averages and standard deviations computed via application of the Monte Carlo (MC) method and the EM-UQ framework. Additionally, probability density functions of these observables are estimated via a 5000-point MC simulation performed on an HDMR-constructed surrogate model, and compared with those directly obtained via MC simulations [Fig. 4-11 (a)-(b)]. Clearly, the EM-UQ framework provides accurate averages and standard deviations for the current magnitude and phase.

It can be observed that the mean of the current at port of the receiving loop antenna is above values detectable by modern receivers [71]. Hence, the TTE system holds significant potential to aid in post-event communications.

Statistics	Observables	Direct MC	Proposed framework
Mean	Magnitude of currents	4.14 $\mu\text{A}$	4.12 $\mu\text{A}$
	Phase of currents	8.26 degrees	7.76 degrees
Standard deviation	Magnitude of currents	4.10 $\mu\text{A}$	4.16 $\mu\text{A}$
	Phase of currents	110.2 degrees	111.35 degrees

Table 4-2 Comparison of statistics and number of deterministic simulations obtained via direct MC method and the proposed framework for magnitude and phase of port current.

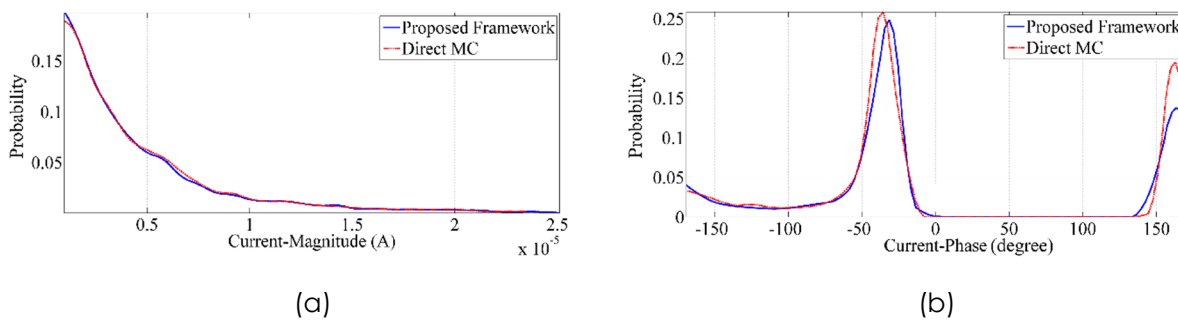


Fig. 4-11: PDF of (a) magnitude and (b) phase of port current.

### 4.3 Medium Frequency System

Medium frequency (MF) communications systems operate in the 300 kHz to 3 MHz band. Higher frequency radios operating in the VHF (30 MHz to 300 MHz) and UHF bands (300 MHz to 3 GHz) oftentimes are restricted to Line-of-Sight (LoS) coverage, and they signals cannot propagate around sharp corners and through rock falls. MF radio waves, in contrast, can propagate through complex geometries especially if they are parasitically coupled to nearby existing metallic conductors present in the mine [Fig. 4-12]. These conductors, for example, can be mine telephone wires, rails, water pipes, or leaky feeder cables. Among them, solid copper twisted-pair phone wire and leaky feeder cable oftentimes serve as excellent conductors for propagating MF signals. These conductors also act as distributed antennas that aid in the reception and transmission of MF signals. Because they operate at such low frequencies, MF radios are significantly larger and heavier than typical hand-held UHF or VHF ones, and are not easily carried around by miners [72]. MF systems nonetheless may provide important alternative communications paths from a working section to the surface. For example, in an emergency

event, MF communication may still be possible through conductors in boreholes that extend from the surface to a tunnel or gallery.

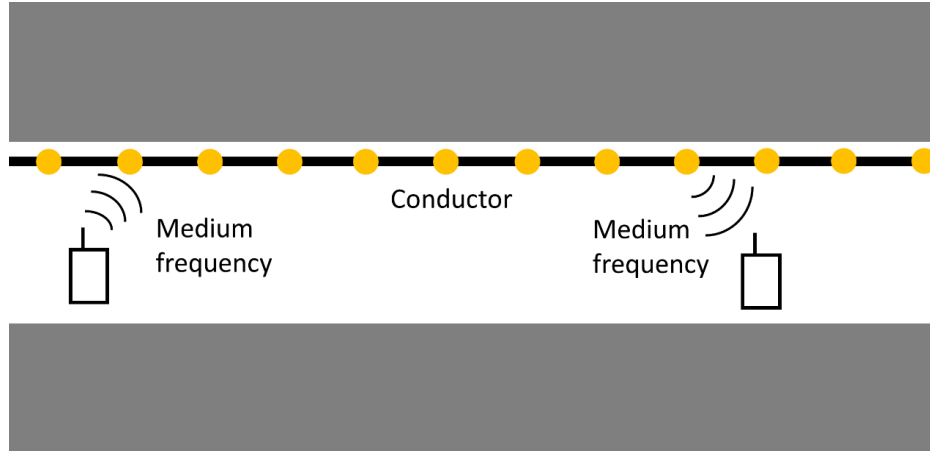
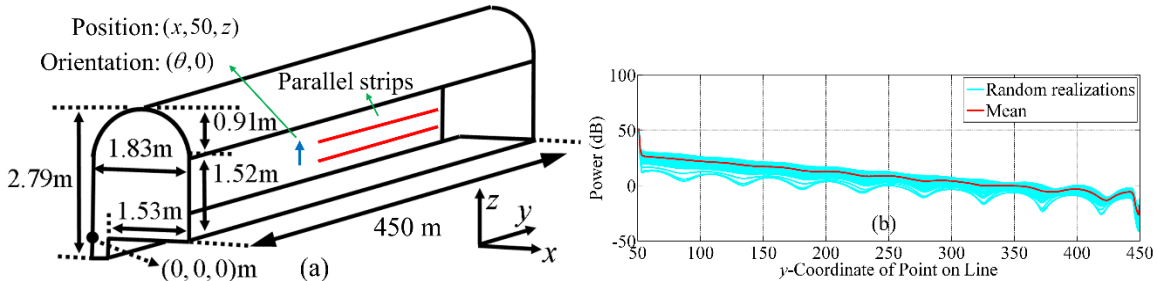


Fig. 4-12: A simple medium frequency communication system.

To determine what factors affect the behavior of MF propagation in mines, extensive numerical modeling is called for. Here, the proposed full-wave EM-UQ framework is used to analyze the MF systems in Fig. 4-13. The tunnel is 450 m long and arched; two parallel PEC strips model a transmission line inside the entry [Fig. 4-13(a)]. These strips, which are 400-m long, infinitesimally thin, 6 cm wide, and separated by 0.6 m, model a transmission line placed near the lateral entry wall and are centered at  $(0.17, 245, 0.87)$  m and  $(0.17, 245, 1.47)$  m. The full wave simulation is performed without FMM-FFT acceleration as the FMM-FFT algorithm is numerically unstable for low frequencies. The electric dipole that models the transmitter is oriented in the  $(\theta, 0)$  direction, operated at 3 MHz, and located at  $(x, 50, z)$ , where  $\theta$ ,  $x$  and  $z$  are random variables uniformly distributed in the ranges  $[0, 90]$ ,  $[0.875, 0.945]$  and  $[1.0, 1.44]$ , respectively. The mean and standard deviation of power densities along a line connecting points  $(0.915, 51, 1.22)$  m and  $(0.915, 350, 1.22)$  m are obtained by the EM-UQ framework [Fig. 4.12 (b)-(c)]. Finally, the PDF of the power density at point  $(0.915, 320, 1.22)$  m is computed [Fig. 4-13(d)]; 41 deterministic simulations are required in this example.

From the data presented, one concludes that the orientation and location of the transmitter relative to the metal strips plays an important role in controlling wave propagation along the entry. Random variations in these quantities may change observed power densities by 10 to 20 dB, implying that great care should be exercised when deploying the system to ensure optimal functionality.





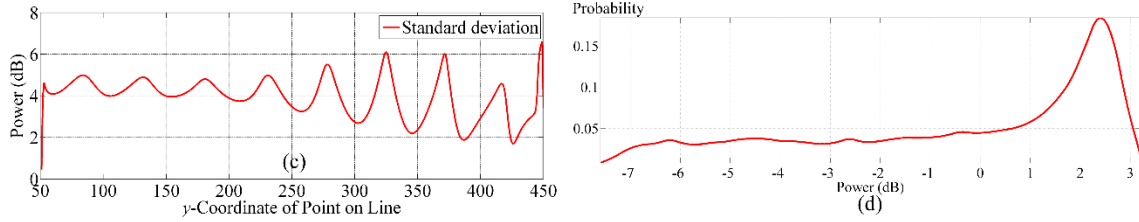


Fig. 4-13: (a) Geometry of a 450-meter arched entry and the parallel strips modeling conductors. (b) Mean and some random realizations of power values along a line in center of the entry. (c) Standard deviation of power values along a line in the center of the entry (d) PDF of the power values at a selected receiver. (Scale: dBm + 40).

#### 4.4 Optimal Placement of Nodes in Wireless Communication systems

This section expands on the results in Section 3.3.4.

In all examples below, mine entries are air-filled and surrounded by rock with relative permittivity  $\epsilon_r = 8.9$ , relative permeability  $\mu_r = 1$ , and conductivity  $\sigma$ ; here  $\epsilon_r$ ,  $\mu_r$ ,  $\sigma$  are related to  $\epsilon_1$  and  $\mu_1$  via  $\mu_1 = \mu_r \mu_0$  and  $\epsilon_1 = \epsilon_0 \epsilon_r - j \sigma / \omega$ . The smallest region size threshold for terminating the optimization algorithm is set to 0.05 m. The combination parameter  $\rho$  for  $f_c$  is 0.5 for all examples. The transmitters are modeled by infinitesimal electric dipoles with unit moment. The power values obtained by the proposed simulator and other methods are normalized to their maxima.

##### 4.4.1 Mine Gallery with Straight Entries

The proposed EM framework is used to optimize a four-transmitter network inside a mine gallery formed by eight entries. Four of them extend along the  $x$ -direction and intersect with the remaining four entries that extend along  $y$  [Fig. 4-14(a)]. The wireless network includes four transmitters that operate at 455 MHz and are placed inside the entries that extend along the  $x$ -direction. The positions of transmitters 1, 2, 3 and 4 are  $(x_1, 0.925, 1.12)$  m,  $(x_2, 13.775, 1.12)$  m,  $(x_3, 26.625, 1.12)$  m, and  $(x_4, 39.475, 1.12)$  m, respectively [Fig. 4-14(b)]. The variables  $x_1$ ,  $x_2$ ,  $x_3$ , and  $x_4$  are optimized over the ranges [20, 60] m, [30, 60] m, [30, 80] m, and [42, 80] m, respectively. Eight access points (i.e. wireless nodes connected to a wired network) reside in the mine gallery [Fig. 4-14(b)]. Seven of them reside 2 m before the ends of the entries and the remaining one is placed at the center of entry 7. The optimization is terminated after 221 objective function evaluations. The optimized results are  $x_1 = 31.11$ ,  $x_2 = 45.10$ ,  $x_3 = 56.85$ , and  $x_4 = 70.44$ . The power densities are computed on the  $xy$ -plane at  $z = 1.12$  m [Fig. 4-11 (c)]. Apparently, all access points obtain LoS connections to transmitters. It should be noted that the optimization results avoided many local optima. For example, one can move transmitter 2 to the intersection of entries 2 and 7 and transmitter 3 to the intersection of entry 3 and 6, while the LoS connections between access points and transmitters are maintained. However, this is not the globally best solution as the value of objective function for this placement is inferior to that for the above configuration. Average CPU time of one distinct simulation is approximately 1.2 hours.

Next, the proposed framework is used to reconfigure the optimized the network after a catastrophic event. Two cave-ins appeared in entries 6 and 7, blocking the LOS connection between access points in those entries and transmitters. During reconfiguration, the variables  $x_1$ ,  $x_2$ ,  $x_3$ , and  $x_4$  are reset, and re-optimized in the ranges [20, 60] m, [30, 60] m, [30, 80] m, and [42, 80] m, respectively [Fig. 4-14(d)]. The reconfiguration process took 255 objective function

evaluations to converge. After reconfiguration, the positions of transmitter 1, 2, 3 and 4 are (43.95, 0.925, 1.12), (32.11, 13.775, 1.12), (57.20, 26.625, 1.12), and (70.38, 39.475, 1.12) respectively. The power values of the reconfigured network are computed on the  $xy$ -plane at  $z = 1.12$  m [Fig. 4-11 (e)]. Note that the access point in entry 7 did not have a LoS connection with any transmitter. The positions of transmitters and power values on the  $xy$ -plane of a manually configured network are shown in Fig. 4-11 (f). While after optimization all access points have LoS connections, it is observed that those in entries 5 and 3 are not well served as they are far from the transmitters.

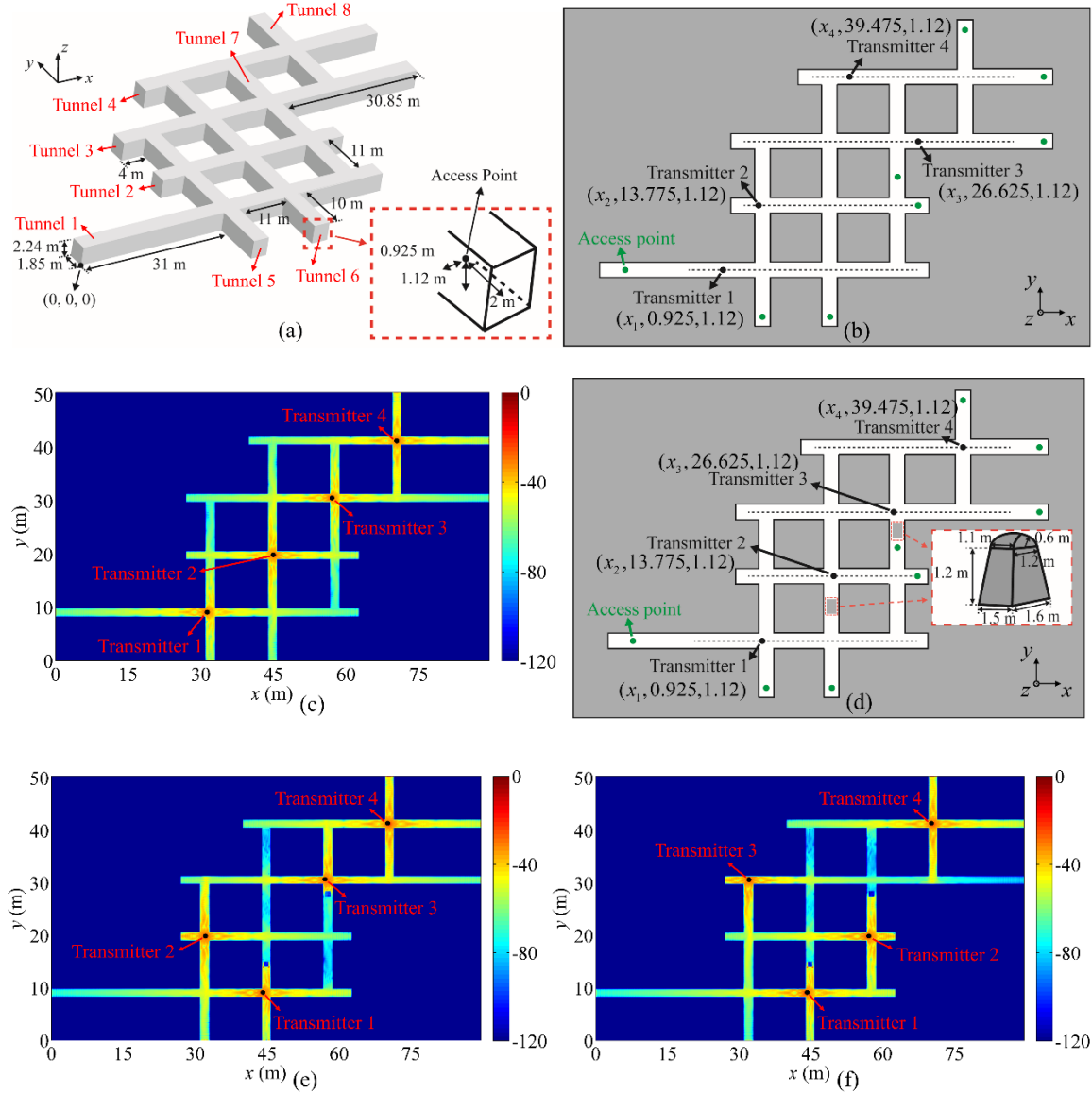


Fig. 4-14 (a) Geometry of the 4 by 4 mine gallery. (b) Transmitters and access points on plane  $z = 1.12$  m. (c) Power values of the optimized network computed on plane  $z = 1.12$  m (scale: dB). (d) Optimized



network and the cave-in. (e) Power values computed on plane  $z = 1.12$  m after reconfiguration (scale: dB) (f) Power values of the manually configured network computed on plane  $z = 1.12$  m (scale: dB)

#### 4.4.2 Mine Gallery with Nonorthogonally Intersecting Entries

Next the EM framework is used to optimize a four-transmitter network inside a mine gallery formed by three entries. Two of them extend along the  $x$ -direction and obliquely intersect the remaining entry [Fig. 4-15(a)]. The wireless network includes four transmitters that operate at 455 MHz. The positions of transmitters 1, 2, 3 and 4 are  $(x_1, 0.925, 1.12)$  m,  $(x_2, 0.925, 1.12)$  m,  $(x_3, 32.22, 1.12)$  m, and  $(x(y_4), y_4, 1.12)$  m, respectively [Fig. 4-15(b)]. The variables  $x_1$ ,  $x_2$ ,  $x_3$ , and  $y_4$  are to be determined in the ranges  $[10, 45]$  m,  $[75, 100]$  m,  $[80, 101]$  m, and  $[-13, 30]$  m, respectively. Note that  $x(y_4)$  is a function that maintains the position of transmitter 4 in the middle of the cross-section of entry 3. Seven access points are positioned at  $(5.0, 0.925, 1.12)$  m,  $(50, 0.925, 1.12)$  m,  $(70, 0.925, 1.12)$  m,  $(108.45, -12.78, 1.12)$  m,  $(110, 16.57, 1.12)$  m,  $(76, 0.925, 1.12)$  m, and  $(108.45, 45.93, 1.12)$  m [Fig. 4-15(b)]. The EM framework converged after 231 objective function evaluations. The optimized positions of transmitters 1-4 are  $(24.93, 0.925, 1.12)$  m,  $(75.16, 0.925, 1.12)$  m,  $(100.16, 32.22, 1.12)$  m, and  $(107.6, -11.31, 1.12)$  m, respectively. The power values computed in the  $z=1.12$  plane is shown in [Fig. 4-15(c)]. While not all access points have LoS connections, the optimized constellation serves them as well as is possible given 4 transmitters.

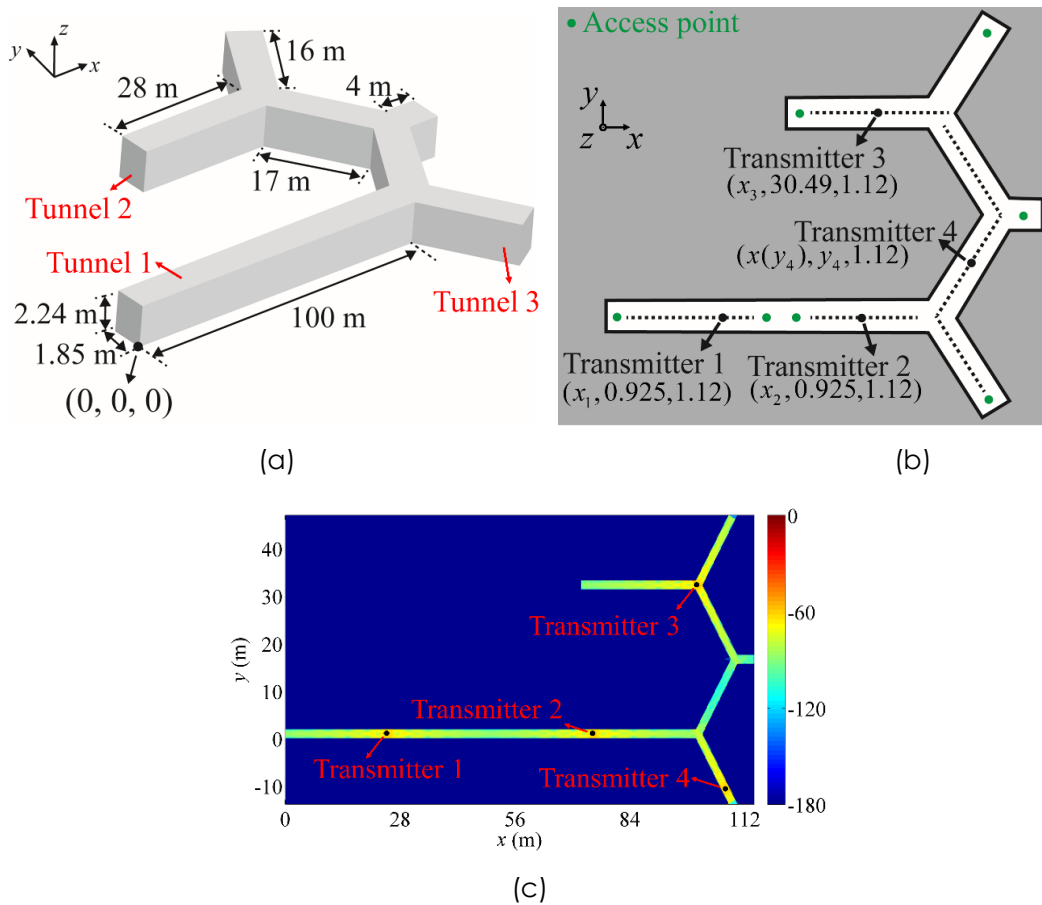


Fig. 4-15 (a) Geometry of the gallery. (b) Transmitters and access points on plane  $z=1.12$  m. (c) Power values computed on plane  $z=1.12$  m (scale: dB).

## 5 Publication Record and Dissemination Efforts:

### 5.1 Publication Record

#### A) Journal Papers

- [1] W. Sheng, A. C. Yucel, Yang Liu, Han Guo, and E. Michielssen, "A Domain Decomposition based Surface Integral Equation Simulator for Characterizing EM Wave Propagation in Mine Environments", in preparation
- [2] W. Sheng, A. C. Yucel, Yang Liu, Han Guo, and E. Michielssen, "Optimization of Wireless Communication Network in Mine Environments Using Full Wave EM Simulator", in preparation
- [3] W. Sheng, Yang Liu, A. C. Yucel, Han Guo, and E. Michielssen, A Hierarchical Off-Diagonal Butterfly Factorization Enhanced Domain Decomposition Simulator for Analyzing Wave Propagations in Electrically Large Mine Entrys, in preparation
- [4] A. C. Yucel, W. Sheng, C. Zhou, Y. Liu, H. Bagci and E. Michielssen, "An FMM-FFT Accelerated SIE Simulator for Analyzing EM Wave Propagation in Mine Environments Loaded with Conductors," in *IEEE Journal on Multiscale and Multiphysics Computational Techniques*, vol. 3, pp. 3-15, 2018.
- [5] A. C. Yücel, L. J. Gomez and E. Michielssen, "Compression of Translation Operator Tensors in FMM-FFT-Accelerated SIE Solvers via Tucker Decomposition," in *IEEE Antennas and Wireless Propagation Letters*, vol. 16, pp. 2667-2670, 2017.

#### B) Conference Papers

- [1] W. Sheng, Y. Liu, A. C. Yucel, H. Guo, and E. Michielssen, "Compression of Scattering Matrices in Domain Decomposition Based Surface Integral Equation Simulator via Randomized Hierarchically Off-Diagonal Butterfly Factorization", in *Proc CNC-USNC/URSI National Radio Sci. Meet.*, 2018
- [2] W. Sheng, A. C. Yucel, Yang Liu, Han Guo, and E. Michielssen, "Optimization and Reconfiguration of Wireless Communication Network in Mine Environments", in *Proc CNC-USNC/URSI National Radio Sci. Meet.*, 2018
- [3] W. Sheng, H. Guo, Y. Liu, A. C. Yucel, and E. Michielssen, "A butterfly-based domain decomposition SIE simulator for EM analysis of wireless communication systems in mine environments," in *Proc CNC-USNC/URSI National Radio Sci. Meet.*, 2017
- [4] W. Sheng, A. C. Yucel, and E. Michielssen, "Tucker compressed Muller-SIE for EM analysis of mine communication systems," in *Proc CNC-USNC/URSI National Radio Sci. Meet.*, 2017
- [5] W. Sheng, A. C. Yucel, and E. Michielssen, "Optimization of wireless network configurations in mine environments," in *Proc CNC-USNC/URSI National Radio Sci. Meet.*, 2016
- [6] W. Sheng, A. C. Yucel, and E. Michielssen, "A domain decomposition based surface integral equation solver for characterizing electromagnetic wave propagation in mine environments," in *Proc IEEE Int. Symp. Antennas Propagat.*, 2016
- [7] A. C. Yucel, L. J. Gomez, and E. Michielssen, "Tucker decomposition for compressing translation operator tensors in FMM-FFT accelerated SIE solvers," in *Proc CNC-USNC/URSI National Radio Sci. Meet.*, 2015

## 5.2 Dissemination Efforts

In addition to the three full papers listed above as in preparation, the PI will continue to disseminate the findings of the study through:

- (i) Conference presentations. Additional presentations on optimization and reconfiguration of networks is planned for 2019.
- (ii) Short courses (e.g. PI Michielssen oftentimes teaches a short course on preconditioners for computational electromagnetics at the annual IEEE Antenna and Propagation Symposium and the DD methods developed under this grant make a perfect example of an advanced preconditioner).

Finally, the PI is available to anyone in the Alpha Foundation and Mine Safety community for consultation and presentation of the methods and findings.

## 6 Conclusions and Impact Assessment

This report presents a comprehensive EM framework to efficiently and accurately perform analysis, optimization, and statistical analysis of communication systems in realistic and electrically large mine environments.

First, a DD-based SIE simulator developed specifically to efficiently analyzing EM wave propagation in large mine environments with multiple excitations is presented. It alleviates the computational burden of full wave EM simulators by dividing the mine entries or galleries into subdomains that are characterized separately and constructing an inter-domain system assembling the solutions of subdomains. The inter-domain system can be efficiently solved by judiciously combining subdomains. The simulator can be more than 10 times faster than traditional EM simulators such as an FMM-FFT-SIE simulator when used to solve problems with multiple excitations.

Second, a fast Tucker decomposition-enhanced FMM-FFT-SIE simulator for analyzing EM wave propagation in electrically large and realistically loaded mine environments is presented. The simulator leverages Muller and combined field SIEs to model scattering from mine walls and perfect electrically conducting (PEC) objects residing inside mine entries and galleries. A FMM-FFT acceleration scheme is used to accelerate the computation. The solver uses singular value and Tucker decompositions to reduce the memory requirements of the simulator. The simulator can efficiently characterize wave propagations in practical mine environments loaded with equipment.

Next, a HDMR uncertainty quantification scheme is presented that leverages the above two EM simulators. The HDMR scheme permits the accurate and efficient construction of surrogate models for EM observables in high dimensions. Numerical results demonstrated the efficiency and accuracy of the UQ framework. The HDMR method is coupled with the EM simulators to statistically analyze four commonly used communication systems in mine environments, including a leaky-feeder system, a through-the-earth system, a medium frequency system, and a partial-mesh network.

Finally, a DIRECT optimization algorithm is presented and incorporated within the DD-based SIE simulator to efficiently optimize and/or reconfigure wireless communication networks in mine environments. The DIRECT algorithm is a modified version of Lipschitzian optimization methods and is highly efficient in the context of wireless network optimization. Numerical results demonstrate that the optimization framework can efficiently place transmitters in a mine environment, and adapt configurations post-disaster.

The research conducted in this project has provided a comprehensive framework to produce qualitative insights and actionable quantitative data to aid in the design, deployment, and post-event reconfiguration of communication systems commonly used in mine environments. The proposed framework can aid mine operators and designers of mine communication and tracking systems to (i) determine survivability thresholds and assessment metrics for communication and tracking systems; (ii) evaluate signal path transmission loss and noise interference in communication technologies, including through - the - earth communication devices; and (iii) assess the coverage capability, quality of service and accuracy of current communication and tracking technologies.

## 7 Recommendations for Future Work

First, the DD-based simulators can be further accelerated by techniques for rapid compression and computation of very large scattering matrices. An example of these techniques is hierarchical off-diagonal butterfly factorization (HDOBF) scheme. Besides the direct adaption of this technique, the current HDOBF scheme is serially implemented and hence unable to compress very large scattering matrices that are inevitable when analyzing EM problems in high frequencies. Hence, the HDOBF scheme will be parallelized and incorporated with the DD based SIE simulator to characterize EM wave propagations for high-frequency wireless communication systems (such as WLAN systems) in large mine environments. On the other hand, the current HDOBF method only achieves  $O(N_p^{1.25} \log^2 N_p)$  CPU and memory complexities when applying the HDOBF compressed scattering matrices to matrix vector multiplications. It can be further reduced to  $O(N_p \log^2 N_p)$  by using other hierarchical matrix structures, or the butterfly plus scheme. The implementation of the butterfly plus scheme to the HDOBF structure will be investigated.

Next, due to the limited availability of measurement data for complex mine geometry and configurations of mine communication systems, the simulations conducted by the EM framework developed in this project, while realistic, remain relatively simple.

- More complex, real world communication systems. The EM framework should be further applied to more complex and real-world communication systems to provide further insights into the design, deployment, and reconfiguration of communication systems in mine environments and hence to help protect the safety and health of miners. While our study identified the impact of mine carts, parasitic transmission lines (MF systems), and partial cave ins, we did not analyze the effect of “smaller” structures made of penetrable materials (plastic equipment, miners). We believe their effect to be minor relative to that of conducting structures and large (partially penetrable) cave-ins, but recommend their effect be analyzed in depth in follow-up studies.
- Material inhomogeneity. Further studies to quantify the impact of inhomogeneity in a mine's surroundings are called for. All our analyses assumed the entire mine environment was embedded in rock with constant electromagnetic properties/constitutive parameters (permittivity and loss). In practice, this assumption may not hold true. For high-frequency communication systems, where signal penetration into the mine walls is limited, our current solvers can be easily tailored to address inhomogeneity in rock formations, however. Specifically, the domain decomposition methods allow for each mine section to be surrounded by rock with different properties (in other words, rock properties are allowed to vary every few meters). The application of the proposed solvers to inhomogeneous environments at lower frequencies, especially Through the Earth systems, requires more invasive changes. Specifically, they require the use of new Green's functions for media external to the mine. The computation of Green's functions in inhomogeneous media is nontrivial and remains an area of active research in the electromagnetics community.
- “Mine-scale analysis”. All our numerical examples involved sections of mines that are at most a few hundred meters long. From a practical perspective, this suffices to provide insight into signal decay rates, which dictates the placement of amplifiers and repeaters. Analysis of larger mine sections or a full mine-scale analysis is by no means impossible, however (though

the marginal benefits/insights gained from such analysis may not be worth the effort). All examples contained in the report were obtained on a small supercomputer with less than 1000 cores. Using the domain decomposition approach, much larger structures can be analyzed at a cost that scales sublinearly with the mine size. A back of the envelope estimate of the computational resources required for a mine-scale analysis indicates that an environment measuring two miles across containing hundreds of nodes can be analyzed on a supercomputer with roughly 30,000 cores. We note that such infrastructure is readily available from commercial cloud providers.

Finally, the current framework remains a research tool, and as such lacks the coding efficiency and robustness to achieve its full potential. The framework can be further hardened by applying enterprise-grade coding principles and endowed with a graphical user interface to increase its reliability, efficiency, and user friendliness.

## 8. Appendix: important terms

**Uncertainty quantification (UQ)** “is the science of quantitative characterization and reduction of [uncertainties](#) in both computational and real world applications. It tries to determine how likely certain outcomes are if some aspects of the system are not exactly known.” In the context of our study, UQ is applied to determine the uncertainty in computed quantities (e.g. received power), given a parametric description of uncertainties in a mine's layout (e.g. roughness and electromagnetic constitutive parameters of walls) and operational state (e.g. presence of mining and communication equipment, and miners).

(More info: [https://en.wikipedia.org/wiki/Uncertainty\\_quantification](https://en.wikipedia.org/wiki/Uncertainty_quantification)).

**Monte Carlo (MC) method.** UQ can be achieved via many means; among the many options, the Monte Carlo (MC) method is the most popular. In a nutshell, MC repeatedly executes a deterministic/forward simulator for different realizations of the input parameters (selected according to the specified probability density functions (PDFs) for the uncertain parameters), thereby estimating uncertainty of the output/computed quantities, by computing its PDF or variance. MC methods are popular because they are “non-intrusive”: they simply ask the user to execute the deterministic/forward simulator again and again without requiring any modifications to the simulator itself. (UQ methods that call for modifications to the deterministic/forward simulator are called intrusive; while oftentimes more powerful than non-intrusive methods, they are seldom used due to the need for invasive changes to the deterministic/forward simulator). MC methods, while easy to implement, have one important drawback: they converge slowly. Specifically, uncertainty in the predicted quantity only decreases as  $1/\sqrt{n}$  where  $n$  is the number of executions of the deterministic/forward simulator. In this study, we therefore implemented non-intrusive UQ methods that converge much faster, i.e. require far fewer executions of the deterministic/forward simulator to yield trustworthy data.

(More info: [https://en.wikipedia.org/wiki/Monte\\_Carlo\\_method](https://en.wikipedia.org/wiki/Monte_Carlo_method)).

**Probability density function (PDF) or density** of a [continuous random variable](#), is a [function](#), whose value at any given sample (or point) in the [sample space](#) (the set of possible values taken by the random variable) can be interpreted as providing a *relative likelihood* that the value of the random variable would equal that sample. In our study, EM simulators are used to estimate

PDFs of received power given uncertainties in the mine layout and operational state. The PDF's maximum indicates the most likely received power; its width is a measure of the uncertainty in the received power.

(More info: [https://en.wikipedia.org/wiki/Probability\\_density\\_function](https://en.wikipedia.org/wiki/Probability_density_function)).

**Electric permittivity, permeability, and loss.** **Permittivity** usually is denoted by the Greek letter  $\epsilon$  (epsilon), is the measure of capacitance that is encountered when forming an [electric field](#) in a particular [medium](#). More specifically, permittivity describes the amount of charge needed to generate one unit of [electric flux](#) in a particular medium." The permittivity of a material is a complex number. The real part of the permittivity is closely related to a material's refractive index. The higher the real part of the permittivity, the more fields have a tendency to reflect from interfaces between air and the material (e.g. the wall of a mine tunnel). The imaginary part of the permittivity is indicative of losses in the material, and relates to "the loss", often denoted  $\sigma$  as  $\epsilon_{\text{imaginary}} = \sigma / (2\pi f)$  where  $f$  is the frequency. The higher the imaginary part of the permittivity, the faster a signal decays in a material. The permittivity of ore and soil is frequency dependent. Except for very low frequencies, the losses in ore and soil are such that waves cannot propagate more than a few meters into the material. The permeability of a material is the magnetic counterpart of the electrical permittivity.

(More info: <https://en.wikipedia.org/wiki/Permittivity>).

**Electrical size/dimension** of an object refers to the size of the object measured in wavelengths. In free space (or equivalently, inside a mine tunnel or gallery), the wavelength of an electromagnetic signal is given by  $\lambda = c / f$  where  $c = 3 \times 10^8$  m/s is the speed of light and  $f$  is the frequency. For example, at  $f = 300$  MHz,  $\lambda = 1$  m. Because wavelengths for most communication systems are smaller than a meter, mining tunnels and galleries are "electrically large," that is, their measure thousands if not millions wavelengths across. Full wave EM solvers analyze propagation phenomena by approximating wave quantities of interest in terms of "basis functions." They typically employ at least 10 such basis functions per wavelength; the total number of basis functions oftentimes tallies in the (tens of) millions. Keeping track of all these functions and solving for their amplitudes is a formidable task, even on today's powerful computers.

**Electromagnetic wavelength.** See note on "Electrical size / dimension"

## 9. References

- [1] "Underground coal mining disasters and fatalities-U.S. 1900-2006."
- [2] A. E. Forooshani, S. Bashir, D. G. Michelson, and S. Noghanian, "A survey of wireless communications and propagation modeling in underground mines," *IEEE Commun. Surveys Tuts.*, vol. 15, pp. 1524-1545, 2013.
- [3] A. Emslie, R. Lagace, and P. Strong, "Theory of the propagation of UHF radio waves in coal mine tunnels," *IEEE Trans. Antennas Propagat.*, vol. 23, pp. 192-205, 1975.
- [4] Z. Sun and I. F. Akyildiz, "Channel modeling and analysis for wireless networks in underground mines and road tunnels," *IEEE Trans. Commun.*, vol. 58, pp. 1758-1768, 2010.
- [5] D. Didascalou, T. Schafer, F. Weinmann, and W. Wiesbeck, "Ray-density normalization for ray-optical wave propagation modeling in arbitrarily shaped tunnels," *IEEE Trans. Antennas Propagat.*, vol. 48, pp. 1316-1325, 2000.
- [6] Y. Hwang, Y. P. Zhang, and R. G. Kouyoumjian, "Ray-optical prediction of radio-wave propagation characteristics in tunnel environments. 1. Theory," *IEEE Trans. Antennas Propagat.*, vol. 46, pp. 1328-1336, 1998.
- [7] S. F. Mahmoud and J. R. Wait, "Geometrical optical approach for electromagnetic wave propagation in rectangular mine tunnels," *Radio Sci.*, vol. 9, pp. 1147-1158, 1974.
- [8] M. F. Hadi and S. F. Mahmoud, "Modeling wireless propagation in a rectangular tunnel with the compact-FDTD method," in *Proc. IEEE RWS*, 2008, pp. 339-342.
- [9] L. Ramirez, F. Hasselmann, and Y. Zhang, "Channel characteristics in tunnels: FDTD simulations and measurement," *J. Microw. Opt. Electromag. Appl.*, vol. 10, pp. 121-130, 2011.
- [10] Y. Wu, M. Lin, and I. J. Wassell, "Modified 2D finite-difference time-domain based tunnel path loss prediction for wireless sensor network applications," *J. Commun.*, vol. 4, pp. 214-223, 2009.
- [11] G. S. Ching, K. Tsuda, and Y. Kishiki, "Analysis of path gain inside tunnels based on FDTD and ray tracing methods," in *Proc. Int. Symp. EM Theory*, 2013, pp. 644-647.
- [12] A. C. Yücel, Y. Liu, H. Bağcı, and E. Michielssen, "Statistical Characterization of Electromagnetic Wave Propagation in Mine Environments," *IEEE Antennas Wireless Propagat. Lett.*, vol. 12, pp. 1602-1605, 2013.
- [13] D. E. Bocker, P. E. Sieber, P. L. Werner, and D. H. Werner, "A hybrid approach for large-scale optimizations of medium frequency propagation in coal mines," in *Proc. IEEE Int. Symp. Antennas Propagat.*, 2011, pp. 2391-2394.
- [14] O. Bakir, A. C. Yucel, E. Michielssen, and H. Bağcı, "Statistical characterization of wave propagation in mine environments," in *Proc. IEEE Int. Symp. Antennas Propagat.*, 2012, pp. 1-2.
- [15] A. C. Yücel, Y. Liu, H. Bağcı, and E. Michielssen, "An FMM-FFT accelerated integral equation solver for characterizing electromagnetic wave propagation in mine tunnels and galleries loaded with conductors," in *Proc. CNC-USNC/URSI National Radio Sci. Meet.*, 2014, pp. 65-65.
- [16] D. Xiu and G. E. Karniadakis, "The Wiener-Askey polynomial chaos for stochastic differential equations," *SIAM J. Sci. Comput.*, vol. 24, pp. 619-644, 2002.
- [17] A. C. Yucel, H. Bağcı, and E. Michielssen, "An adaptive multi-element probabilistic collocation method for statistical EMC/EMI characterization," *IEEE Trans. Electromagn. Compat.*, vol. 55, pp. 1154-1168, 2013.
- [18] A. C. Yücel, H. Bağcı, and E. Michielssen, "An ME-PC enhanced HDMR method for efficient statistical analysis of multiconductor transmission line networks," *IEEE Trans. Compon. Packag. Manuf. Technol.*, vol. 5, pp. 685-696, 2015.
- [19] K. Deb, A. Pratap, S. Agarwal, and T. Meyarivan, "A fast and elitist multiobjective genetic algorithm: NSGA-II," *IEEE Trans. Evol. Comput.*, vol. 6, pp. 182-197, 2002.
- [20] J. Kennedy, "Particle swarm optimization," in *Encyclopedia of machine learning*, ed: Springer, 2011, pp. 760-766.



- [21] R. W. Wedderburn, "Quasi-likelihood functions, generalized linear models, and the Gauss—Newton method," *Biometrika*, vol. 61, pp. 439-447, 1974.
- [22] N. K. Georgieva, S. Glavic, M. H. Bakr, and J. W. Bandler, "Feasible adjoint sensitivity technique for EM design optimization," *IEEE Trans. Microwave Theory Tech.*, vol. 50, pp. 2751-2758, 2002.
- [23] J. A. Nelder and R. Mead, "A Simplex Method for Function Minimization," *The Computer Journal*, vol. 7, pp. 308-313, 1965.
- [24] R. Hooke and T. A. Jeeves, "`` Direct Search" Solution of Numerical and Statistical Problems," *J. ACM*, vol. 8, pp. 212-229, 1961.
- [25] D. E. Finkel, "DIRECT optimization algorithm user guide," Center for Research in Scientific Computation, North Carolina State University 2003.
- [26] J. M. Gablonsky, "Modifications of the DIRECT Algorithm," Ph.D. Thesis, Department of Mathematics, North Carolina State University, 2001.
- [27] D. R. Jones, C. D. Perttunen, and B. E. Stuckman, "Lipschitzian optimization without the Lipschitz constant," *J. Optim. Theory Appl.*, vol. 79, pp. 157-181, 1993.
- [28] H. Guo, Y. Liu, J. Hu, and E. Michielssen, "A Butterfly-Based Direct Integral-Equation Solver Using Hierarchical LU Factorization for Analyzing Scattering From Electrically Large Conducting Objects," *IEEE Trans. Antennas Propagat.*, vol. 65, pp. 4742-4750, Sep 2017.
- [29] A. C. Yücel, "Uncertainty Quantification for Electromagnetic Analysis via Efficient Collocation Methods," Ph.D. Thesis, EECS Department, University of Michigan, Ann Arbor, MI, 2013.
- [30] A. C. Yücel, L. J. Gomez, and E. Michielssen, "Compression of Translation Operator Tensors in FMM-FFT-Accelerated SIE Solvers via Tucker Decomposition," *IEEE Antennas Wireless Propagat. Lett.*, vol. 16, pp. 2667-2670, 2017.
- [31] R. L. Wagner, S. Jiming, and W. C. Chew, "Monte Carlo simulation of electromagnetic scattering from two-dimensional random rough surfaces," *IEEE Trans. Antennas Propagat.*, vol. 45, pp. 235-245, 1997.
- [32] C. Waltz, K. Sertel, M. A. Carr, B. C. Usner, and J. L. Volakis, "Massively parallel fast multipole method solutions of large electromagnetic scattering problems," *IEEE Trans. Antennas Propagat.*, vol. 55, pp. 1810-1816, 2007.
- [33] S. Rao, D. Wilton, and A. Glisson, "Electromagnetic scattering by surfaces of arbitrary shape," *IEEE Trans. Antennas Propagat.*, vol. 30, pp. 409-418, 1982.
- [34] W. C. Chew, E. Michielssen, J. Song, and J.-M. Jin, *Fast and efficient algorithms in computational electromagnetics*: Artech House, Inc., 2001.
- [35] E. Michielssen and A. Boag, "A multilevel matrix decomposition algorithm for analyzing scattering from large structures," *IEEE Trans. Antennas Propagat.*, vol. 44, pp. 1086-1093, 1996.
- [36] R. W. Freund, "A Transpose-Free Quasi-Minimal Residual Algorithm for Non-Hermitian Linear Systems," *SIAM J. Sci. Comput.*, vol. 14, pp. 470-482, 1993.
- [37] C. Zhou, J. Waynert, T. Plass, and R. Jacksha, "Attenuation constants of radio waves in lossy-walled rectangular waveguides," *Prog. Electromagn. Res.*, vol. 142, pp. 75-105, 2013.
- [38] Zhou, Chenming and J. Waynert, "The equivalence of the ray tracing and modal methods for modeling radio propagation in lossy rectangular tunnels," *IEEE Antennas Wireless Propag. Lett.*, vol. 13, pp. 615-618, 2014.
- [39] A. C. Yucel, L. J. Gomez, and E. Michielssen, "Compression of translation operator tensors in FMM-FFT accelerated SIE solvers via Tucker decomposition," *IEEE Antennas Wireless Propag. Lett.*, (in press), 2017.
- [40] C. Müller, *Foundations of the mathematical theory of electromagnetic waves* vol. 155: Springer Science & Business Media, 2013.
- [41] S. M. Rao, D. R. Wilton, and A. W. Glisson, "Electromagnetic scattering by surfaces of arbitrary shape," *IEEE Trans. Antennas Propagat.*, vol. 30, pp. 409-418, May 1982.

- [42] D. D. Donno, A. Esposito, L. Tarricone, and L. Catarinucci, "Introduction to GPU Computing and CUDA Programming: A Case Study on FDTD [EM Programmer's Notebook]," *IEEE Antennas Propagat. Mag.*, vol. 52, pp. 116-122, 2010.
- [43] W. C. Chew, E. Michielssen, J. M. Song, and J. M. Jin, *Fast and efficient algorithms in computational electromagnetics*. Norwood, MA, USA: Artech House, Inc., 2001.
- [44] J. M. Taboada, L. Landesa, F. Obelleiro, J. L. Rodriguez, J. M. Bertolo, M. G. Araujo, et al., "High scalability FMM-FFT electromagnetic solver for supercomputer systems," *IEEE Antennas Propagat. Mag.*, vol. 51, pp. 20-28, 2009.
- [45] L. D. Lathauwer, B. D. Moor, and J. Vandewalle, "A multilinear singular value decomposition," *SIAM J. Matrix Anal. Appl.*, vol. 21, pp. 1253-1278, 2000.
- [46] T. G. Kolda and B. W. Bader, "Tensor decompositions and applications," *SIAM Rev.*, vol. 51, pp. 455-500, 2009.
- [47] T. El-Moselhy and L. Daniel, "Stochastic integral equation solver for efficient variation-aware interconnect extraction," in *Proceedings of the 45th annual Design Automation Conference*, 2008, pp. 415-420.
- [48] T. El-Moselhy and L. Daniel, "Variation-aware interconnect extraction using statistical moment preserving model order reduction," in *Proceedings of the Conference on Design, Automation and Test in Europe*, 2010, pp. 453-458.
- [49] R. G. Ghanem and P. D. Spanos, "Stochastic Finite Element Method: Response Statistics," in *Stochastic finite elements: a spectral approach*, ed: Springer, 1991, pp. 101-119.
- [50] M. Loève, "Elementary Probability Theory," in *Probability Theory I*, ed: Springer, 1977, pp. 1-52.
- [51] G. B. Arfken and H. J. Weber, "Mathematical methods for physicists," ed: AAPT, 1999.
- [52] G. H. Golub and C. F. Van Loan, *Matrix computations* vol. 3: JHU Press, 2012.
- [53] N. Garcia and E. Stoll, "Monte Carlo calculation for electromagnetic-wave scattering from random rough surfaces," *Phys. Rev. Lett.*, vol. 52, p. 1798, 1984.
- [54] L. J. Gomez, A. C. Yücel, L. Hernandez-Garcia, S. F. Taylor, and E. Michielssen, "Uncertainty Quantification in Transcranial Magnetic Stimulation via High-Dimensional Model Representation," *IEEE Trans. Biomed. Eng.*, vol. 62, pp. 361-372, 2015.
- [55] Z. Gao and J. S. Hesthaven, "On ANOVA expansions and strategies for choosing the anchor point," *Appl. Math. Comput.*, vol. 217, pp. 3274-3285, 2010/12/01/ 2010.
- [56] I. M. Sobol, "Theorems and examples on high dimensional model representation," *Reliab. Eng. Syst. Saf.*, vol. 79, pp. 187-193, 2003/02/01/ 2003.
- [57] Z. Zhang, M. Choi, and G. E. Karniadakis, "Anchor Points Matter in ANOVA Decomposition," in *Spectral and High Order Methods for Partial Differential Equations: Selected papers from the ICOSAHOM '09 conference, June 22-26, Trondheim, Norway*, J. S. Hesthaven and E. M. Rønquist, Eds., ed Berlin, Heidelberg: Springer Berlin Heidelberg, 2011, pp. 347-355.
- [58] H. D. Sherali, C. M. Pendyala, and T. S. Rappaport, "Optimal location of transmitters for micro-cellular radio communication system design," *IEEE J. Sel. Areas Commun.*, vol. 14, pp. 662-673, 1996.
- [59] S. J. Fortune, D. M. Gay, B. W. Kernighan, O. Landron, R. A. Valenzuela, and M. H. Wright, "WISE design of indoor wireless systems: practical computation and optimization," *IEEE Comput. Sci. Eng.*, vol. 2, pp. 58-68, 1995.
- [60] M. H. Wright, "Optimization methods for base station placement in wireless applications," in *Vehicular Technology Conference, 1998. VTC 98. 48th IEEE*, 1998, pp. 387-391.
- [61] Z. Yun, S. Lim, and M. F. Iskander, "An integrated method of ray tracing and genetic algorithm for optimizing coverage in indoor wireless networks," *IEEE Antennas Wireless Propagat. Lett.*, vol. 7, pp. 145-148, 2008.
- [62] J. He, A. A. Verstak, L. T. Watson, C. A. Stinson, N. Ramakrishnan, C. A. Shaffer, et al., "Globally optimal transmitter placement for indoor wireless communication systems," *IEEE Trans. Wireless Commun.*, vol. 3, pp. 1906-1911, 2004.

- [63] J. M. Gablonsky and C. T. Kelley, "A locally-biased form of the DIRECT algorithm," *J. Global Optim.*, vol. 21, pp. 27-37, 2001.
- [64] B. Svensson, N. K. Nia, F. Danielsson, and B. Lennartson, "Sheet-metal press line parameter tuning using a combined DIRECT and Nelder-Mead algorithm," in *2011 IEEE 16th Conf. on ETFA*, 2011, pp. 1-8.
- [65] S. E. Cox, R. T. Haftka, C. A. Baker, B. Grossman, W. H. Mason, and L. T. Watson, "A comparison of global optimization methods for the design of a high-speed civil transport," *J. Global Optim.*, vol. 21, pp. 415-432, 2001.
- [66] "MATLAB R2014a," ed: The MathWorks, Natick, 2014.
- [67] F. Zhang, "Analysis of antenna radiation characteristics in mine tunnels," in *Proceedings of the 9th International Symposium on Antennas, Propagation and EM Theory*, 2010, pp. 327-330.
- [68] X. Yang, S. Feng, X. Zhang, X. Ren, and W. Li, "Research of Single Mode Radiation Leaky Coaxial Cable Used for Ultra Wide-band Communication," in *2006 International Conference on Communications, Circuits and Systems*, 2006, pp. 1261-1264.
- [69] J. H. Wang and K. K. Mei, "Theory and analysis of leaky coaxial cables with periodic slots," *IEEE Trans. Antennas Propagat.*, vol. 49, pp. 1723-1732, 2001.
- [70] S. P. Morgan, "Prediction of indoor wireless coverage by leaky coaxial cable using ray tracing," *IEEE Trans. Veh. Technol.*, vol. 48, pp. 2005-2014, 1999.
- [71] N. Ayuso, J. A. Cuchi, F. Lera, and J. L. Villarroel, "Through-the-earth magnetic field propagation: modelling and experimental validation," in *2006 IEEE Antennas and Propagation Society International Symposium*, 2006, pp. 680-683.
- [72] *Advanced Tutorial on Wireless Communication and Electronic Tracking*. Available: <https://www.cdc.gov/niosh/mining/content/emergencymanagementandresponse/cmmtracking/advcommtrackingtutorial1.html>
- [73] Plass, T., Jacksha, R., Waynert, J. and Zhou, C., 2013, July. Measurement of RF propagation in tunnels. In *Antennas and Propagation Society International Symposium (APSURSI), 2013 IEEE* (pp. 1604-1605). IEEE.
- [74] Zhou, C., Waynert, J., Plass, T. and Jacksha, R., 2013, July. Modeling RF propagation in tunnels. In *Antennas and Propagation Society International Symposium (APSURSI), 2013 IEEE* (pp. 1916-1917). IEEE.